# Welding simulation of steels welded with low transformation temperature (LTT) filler materials

by

Minaalsadat Mirhendi Esfahani

**Diploma work No. 181/2016**

At Department of Materials and Manufacturing Technology

CHALMERS UNIVERSITY OF TECHNOLOGY

Gothenburg, Sweden

Diploma work in the Master Program Materials Engineering

**Performed at:** ESAB / Chalmers University of Technology

Lindholmsallén 9, 417 55 Göteborg

**Supervisor(s):** Dr. Farshid Zamiri Akhlaghi
Post-doctoral researcher, Civil and Environmental Engineering, Structural Engineering

Dr. Johan Ahlström
Associate Professor at Materials Technology

Dr. Kamellia Dalaei
Team leader, Research Team

**Examiner:** Dr. Johan Ahlström
Associate Professor at Materials Technology

# Welding simulation of steels welded with low transformation temperature (LTT) filler materials
# MINAALSADAT MIRHENDI ESFAHANI

## MINAALSADAT MIRHENDI ESFAHANI, 2016

Diploma work no. 181/2016

Department of Materials and Manufacturing Technology

Chalmers University of Technology

SE-412 96 Gothenburg

Sweden

Telephone + 46 (0)31-772 10

Gothenburg, Sweden 2016

**Welding simulation of steels welded with low transformation temperature (LTT) filler materials**

**MINAALSADAT MIRHENDI ESFAHANI**
**Department of Materials and Manufacturing Technology**
**Chalmers University of Technology**

## Summary

Welding is a thermal process that creates residual stresses due to a combination of thermal expansion, plastic flow and phase transformation. By using filler material which has a composition that transforms to phase transformation to Martensite at low temperatures, the residual stress state can become more favorable. The purpose of this thesis is to develop a numerical tool to evaluate temperature evolution, phase transformations and residual stresses developing during multi-pass plate-to-plate welding using LTT filler. The commercially available finite element (FE) software Abaqus v6.13 (Simulia 2013) was used for the numerical simulations.
In the current thesis a transient 3D simulation of a moving heat source with a distributed heat flux is performed. First a repeated analysis of a single pass weld is performed to validate Abaqus as a good simulation software for welding simulation. Then a heat transfer analysis of a plate with 3 pass of weld is performed. Two different heat source models are used and compared. The Abaqus user subroutine DFLUX is used to define the welding torch heat input as a volumetric heat flux. The subroutine is developed in the FORTRAN language. The heat source travels along the weld line to simulate the torch movement. In the next phase of the work, Metallurgical analysis is performed to model the phase transformation during and after welding. User subroutine Hetval is used to model phase transformation. Finally, the data from the previous heat transfer analysis and metallurgical analysis are used as an input file for a mechanical analysis

Keywords: Welding simulation, Abaqus, Heat transfer analysis, phase transformation analysis, Mechanical analysis, JMatPro

## Acknowledgements

This diploma work has been done for completion of the Master's of Science degree at Chalmers University of Technology. The work has been done with the collaboration of ESAB.

I would like to express my sincere appreciation to my supervisors Dr. Johan Ahlström, Dr. Farshid Zamiri Akhlaghi and Dr. Kamellia Dallaei for their valuable guidance, encouragement and continuous support throughout this journey.

At the end I want to dedicate this thesis to my dear parents and my lovely husband for being great supporters of me.

Mina a. Mirhendi Esfahani
June 2016

# Table of Contents

## List of figures

## List of tables

# 1 Introduction

## 1.1 Motivation

Welding is an important joining process for metals and non-metals. It is used to accomplish a certain shape, from more basic geometries in which materials are delivered, like sheets, tubes etc. Welding is a thermal process that creates residual stresses in metals due to a combination of thermal expansion, plastic flow and phase transformation. Normally these stresses become tensile, which can be detrimental especially for fatigue properties. There is a distribution of residual stresses in a welded joint; presence of tensile residual stresses at or near the borderline between the fusion zone and the HAZ is considered most severe. By using filler materials which has a composition that causes phase transformation to martensite at low temperatures, the residual stress state can become more favourable. These filler materials are called Low Transformation Temperature (LTT) materials.

## 1.2 Objective

The purpose of the current thesis is to develop a numerical tool to evaluate temperature evolution, phase transformations and residual stresses developing during multi-pass plate-to-plate welding using a LTT filler material.

Generally, the thermal, mechanical and metallurgical processes are interconnected and comprised of different couplings as shown in Figure 1‑1. Material microstructure can be changed by deformation and temperature change. Moreover, mechanical properties mainly depend on the material microstructure and temperature. Further, thermal expansion can cause deformation, which in turn can produce small amount of heat. Heat capacity, specific heat and latent heat are dependent on microstructure of the material.

In this work, the dominant couplings only are considered. The thermal analysis includes a careful modelling of the heat introduced by the welding process. The phase transformations occurring due to the temperature variations have been modelled with simplified descriptions. Finally, the temperature fields, as well as the phase fields has been used as input for a mechanical model to estimate the residual stresses.

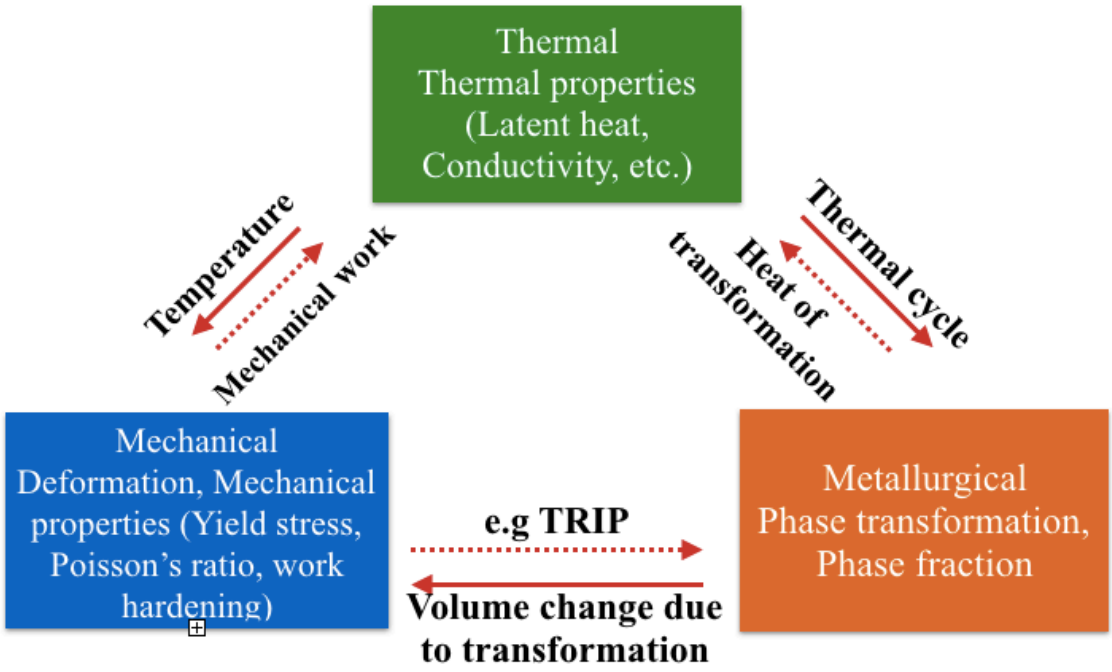


*Figure 1-1. Thermo-mechanical-metallurgical couplings*

## 1.3 Method

The focus of the work is on developing a method for numerical simulation. The commercially available finite element (FE) software Abaqus v6.13 (Simulia 2013) was used for the numerical simulations. It has the functionality to combine code written in user-defined subroutines with the main software.

The first part of the work was to repeat simulations from a previous Round Robin study reported in literature. Thereafter, a specific geometry including three-pass butt-weld was examined. The weld geometry had previously been experimentally characterized regarding microstructure and residual stresses. Results from the experimental characterization was used for verification of the simulation results.

Input for the Numerical simulation was taken from both literature and the commercial software JMatPro6.2.1 For the Round Robin simulation, input was given in the report.

## 1.4 Limitations

- Our research is limited to a specific steel/filler material combination and a a specific type of weld: multipass (3-pass) butt weld.
- In this work, we didn't consider all possible thermo-mechanical-metallurgical couplings.
- Previous residual stresses within the plates from previous procedures like rolling are neglected.
- Transformation plasticity was not considered.

# 2 Background

## 2.1 Welding residual stresses

### 2.1.1 Physical mechanism

Residual stress is a stress state in the material without external loading. The residual stress at a specific position is always in equilibrium with the surrounding material, i.e. if there are tensile residual stresses in one region of a component, there must exist compressive residual stresses elsewhere. Tensile residual stresses can be a major issue in welded components. Welding residual stresses are a result of inhomogeneous heating and cooling during and after welding, giving rise to local thermal expansion and contraction, changed microstructure, changed flow stress and phase transformations. While heating, the material in the weld region expands but the surrounding colder material restrains its expansion which causes compressive stress. Since the yield strength is decreased at elevated temperatures, plastic deformations occur. During cooling, the material contracts and as a result, tensile residual stresses are created at the welding region while the surrounding material balances this to maintain equilibrium. *Fig.1*, shows the effect of shrinkage and phase transformation on residual stress state. Austenite contracts when it cools down from 1200℃ to around 700℃. Austenite has FCC *(Face center Cubic)* structure in which atoms are more closely packed compared to BCC structure. Therefore, when a FCC-BCC phase transformation occurs, volumetric expansion of the transforming material is observed. For instance, when austenite transforms to bainite, it is expanded rather than being contracted. This trend continues until all austenite converts to bainite completely. Then it continues to shrink while the temperature decreases. For certain chemical compositions and cooling rates, austenite transforms to martensite, which has a larger expansion compared to bainite. Also, it takes place at lower temperatures. This gives the possibility to create compressive residual stresses in the welding region and can be beneficial for fatigue life of welded components. The lower the temperature when the martensite forms, the higher the compressive residual stress (Figure 2-1).

### 2.1.2 Residual stresses at different size scales

Based on their span of action, residual stresses are categorized in three categories (Radaj 2003): macroscopic level (type I) that expands over macroscopic regions over several crystallites; microscopic level (type II) which acts within crystallites like residual stress around a dislocation pile up and the atomic scale (type III) which acts between atomic regions for instance residual stress around a single dislocation ( Figure 2-2*)*. Type I residual stresses, are the most commonly considered in engineering applications. For a planar welded connection, the longitudinal and transversal residual stresses are usually studied. Longitudinal residual stress component is caused by weld longitudinal contraction and transverse residual stress is caused by transverse contraction (Figure 2-3*)*.

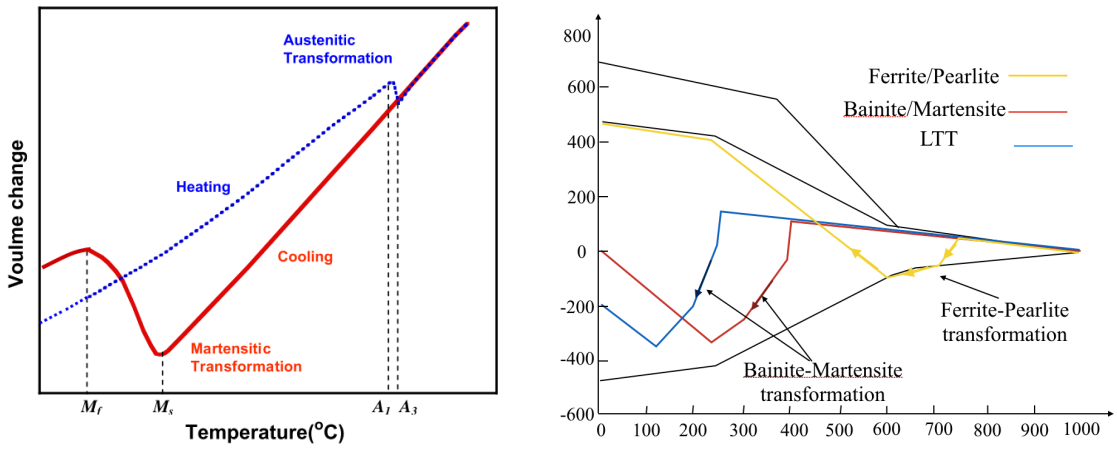


*Figure 2-1* Diagram of shrinkage vs Temperature *(Wohlfahrt et al. 2012)*

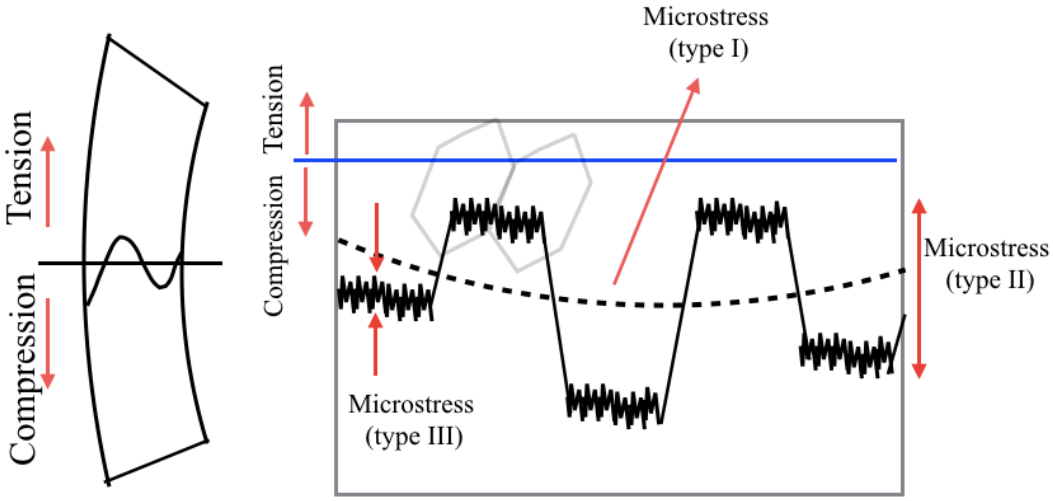


*Figure 2-2 Residual stresses type I, II, and III (Eckard Macherauch 2014)*

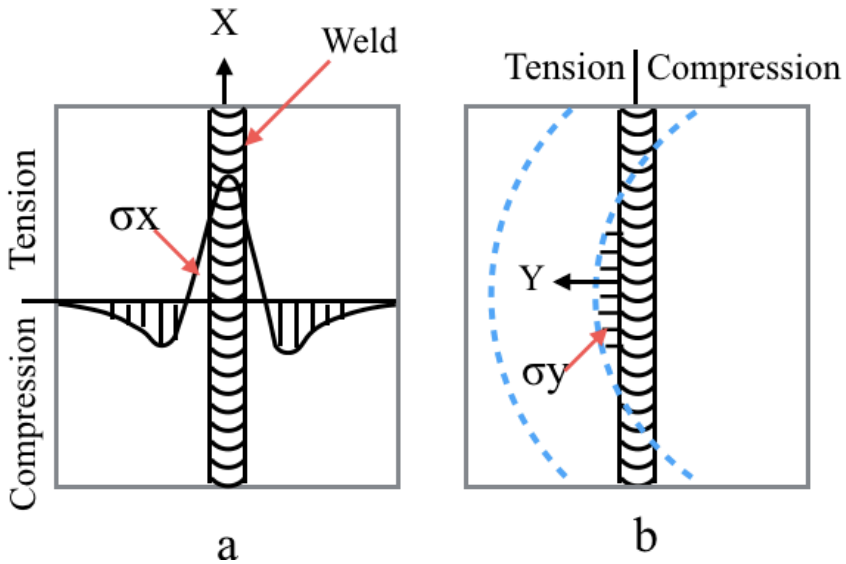


*Figure 2-3* Typical distributions of longitudinal ($\sigma_x$) and transverse ($\sigma_y$) residual

stresses in butt weld. Modified from (Welding Handbook Committee, n.d.)

### 2.1.3 Technical solutions for improvement of fatigue properties of welds

Tensile residual stresses can be one of the factors contributing to lower fatigue strength at the weld toe compared to the base material. Lower heat input or post weld treatments can be used to reduce residual stresses during or after welding. *Hammer* and *Needle Peening* are two methods to modify residual stress at the weld toe (Yildirim 2013). *High Frequency Mechanical Impact (HFMI)* treatment is an alternative technique which has slightly greater effect on fatigue strength than former traditional peening methods (Yildirim 2013). *International Institute of Welding (IIW)* describes the details of different techniques for increasing the fatigue life of the welded structures by locally modifying the residual stress state such as *Ultrasonic Impact Treatment (UIT), Ultrasonic Peening (UP), Ultrasonic Peening Treatment (UPT), High Frequency Impact Treatment (HiFIT), Pneumatic Impact Treatment (PIT)* and *Ultrasonic Needle Peening (UNP)* (G. B. Marquis and H. C. Yıldırım 2015).

A recent approach to eliminate tensile residual stresses at the weld toe is to use *Low Transformation Temperature (LTT)* filler material that leads to enhanced fatigue strength while omitting the need for subsequent thermal or mechanical treatment after welding. LTT materials are metal alloys that show zero or positive net volume change (i.e. expansion) during cooling down phase of the welding process. This is due to displacive austenite-to-martensite phase transformation that occurs at temperatures close to room temperature. If transformation occurs at the higher temperature, further thermal contraction will produce tensile stresses at the weld during cooling to the ambient temperature (Ramjaun, Stone, Karlsson, Kelleher, et al. 2014). The expansion of LTT material can compensate for shrinkage of the heated material during cooling down. It not only reduces the tensile residual stresses at the weld toe, but also produces compressive residual stresses in some cases (Ramjaun, Stone, Karlsson, Kelleher, et al. 2014)(Ramjaun et al. 2014b) (Ramjaun, Stone, Karlsson, Gharghouri, et al. 2014). Several researchers reported the improvement of fatigue strength by using LTT filler material (Shiga et al. 2014), (Ohta et al. 2003), (Barsoum and Gustafsson 2009), (Özdemir et al. 2010). *Fig.4* depicts the influence of phase transformation of LTT material in a temperature-elongation graph in comparison with a conventional filler material. The Martensite transformation start temperature (Ms) is lower than the ordinary filler materials.

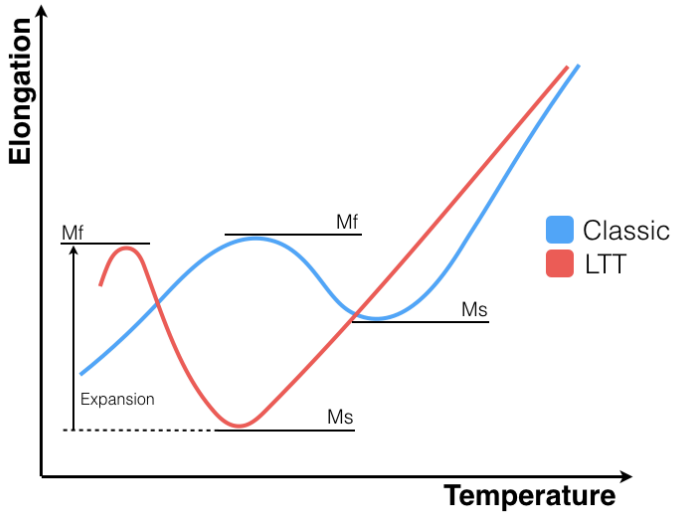


Figure 2-4 Temperature-elongation relationship of LTT welding material *(Günther 2005)*

### 2.1.4 Residual stress measurement

There are different methods to measure residual stresses, both destructive and non-destructive methods. In *Table.1,* some of the most commonly used methods are listed.

Table 2-1 Different methods of residual measurement. (Eckard Macherauch 2014)

| Methods | Measured quantities | Residual stresses determined | Character |
|---|---|---|---|
| **Mechanical** | Macroscopic surface strains | $1^{st}$ kind | Destructive |
| **X-Ray Diffraction** | Homogenous lattice strains | $1^{st}$+ $2^{nd}$ kind | Non-destructive |
| **Neutron Diffraction** | Homogenous lattice strains | $1^{st}$+ $2^{nd}$ kind | Non-destructive |
| **Ultrasonic** | e.g. time of flight differences of shear waves | $1^{st}$+ $2^{nd}$ +$3^{rd}$ kind | Non-destructive |
| **Magnetic** | e.g. Barkhousen-noise amplitude | $1^{st}$+ $2^{nd}$ +$3^{rd}$ kind | Non-destructive |

*X-Ray Diffraction (XRD)* is one of the most accurate methods to measure residual stresses. However, it is restricted to the surface residual stress determination, because of low penetration of x-ray wavelength in the materials. It is important to note that the measured residual stress is the combination of 1st and 2nd kind of residual stresses (E. Macherauch 1984).

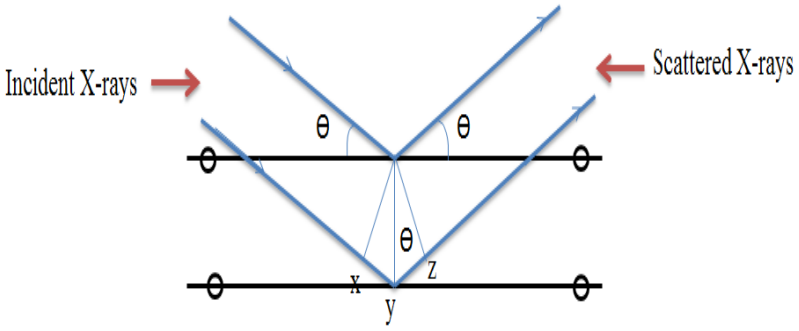


Figure 2-5 Bragg's angle

*XRD* works through an interaction between the incident beam and the crystals on the surface of polycrystalline material. Figure 2-6 shows the constructive interference of the incident X-rays on the material's surface, which occurs when Bragg's law ($n \lambda = 2d \sin \theta$) is satisfied. Angle $\theta$ is the angle of the incident X-ray beam and the lattice planes of the specimen and $2\theta$ is the angle of the incident and scattered X- ray beams which is called Bragg's angle. Differentiation of Bragg's law gives Equation 2-1. This equation relies on the relation of inter-planar spacing of crystal planes $d_{hkl}$ and Bragg´s angle as following equation suggests (Prevéy 2001) (Kirk 1971):

$$n\lambda = 2d\sin\theta \rightarrow \Delta\theta = -\frac{\Delta d}{d_{hkl}}\tan\theta$$ Equation 2-1

The equation shows that the strain $\frac{\Delta d}{d_{hkl}}$, is in relation with angle changes. The residual stress that produces the strain is the arithmetic average stress in a volume of irradiated surface material area of the material. Initially, a plane stress condition is assumed i.e. $\sigma_3=0$ ($\sigma_3$ is the stress component perpendicular to the surface) but $\varepsilon_3$ is not necessarily zero (Fig. 7).

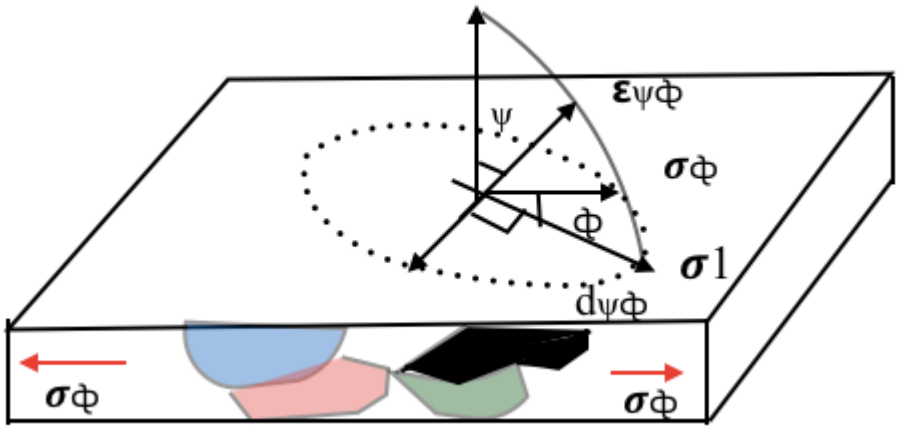


Figure 2-6 plane stress elastic model.*(Paul S Prevéy 1986)*

Strain $\varepsilon_{\varphi\psi}$ between the direction of angle φ and ψ is:

$$\varepsilon_{\varphi\psi} = \left[\frac{1+\upsilon}{E}(\sigma_1 cos^2\,\varphi + \sigma_2 sin^2\varphi)sin^2\psi\right] - \left[\frac{\upsilon}{E}(\sigma_1 + \sigma_2)\right]$$ *Equation 2-2*

υ is the Poisson ratio, E is Young's modulus, and $\sigma_1$ and $\sigma_2$ are the principal stresses in the irradiated surface.

The distance between lattice planes $d_{\varphi\psi}$ can also be measured as follow:

$$d_{\varphi\psi} = \frac{\Delta d}{d_0} = \frac{d_{\varphi\psi} - d_0}{d_0}$$ *Equation 2-3*

Where $d_0$ is the lattice spacing in the absence of stresses. By substituting Equation 2-3 in Equation 2-2, dφψ can be calculated for different ψ angles. If d is plotted for a certain crystal plane versussin $2\psi$, the stress can be calculated. To have a more precise result, a larger Bragg´s angle (usually greater than 120˚) is suggested (Paul S Prevéy 1986).

## 2.2 Welding Metallurgy

Material microstructure in a welded joint can broadly be subdivided into the *Fusion Zone (FZ), the Heat Affected Zone (HAZ)* and the *base material*. Since the material in the HAZ undergoes a complete thermal cycle, its time vs temperature curve is important for the microstructural development, and further sub-division of this zone is sometimes meaningful. The HAZ structure varies from coarse grain structure close to transition zone to finer grain structure. Figure 2-7 shows different sub-regions in HAZ with different microstructures and subsequently different mechanical properties (Easterling 1992). The microstructure of the HAZ also depends on the material thermal and mechanical history, e.g. it differs if the material was in a cold rolled or annealed condition because it affects recrystallization during welding.

The peak temperature ($T_p$) of a thermal cycle can be used as a measure to subdivide the weld joint into the FZ with the $T_p$ above the $T_{solidus}$, the transition zone with the $T_p$ around $T_{solidus}$ and HAZ with heating to above $A_3$ or $A_1$. As can be seen in Figure 2-7, the HAZ is subdivided into different zones: Tempered Base Material, Inter-critical zone (ICHAZ) with temperature between $A_1$ and $A_3$ with a partially austenitized microstructure, Fine grain zone (FGHAZ) with the peak temperature between $A_3$ and 1100 $^\circ$C which yields a recrystallized zone with fine austenite grains and Coarse grain zone (CGHAZ) with peak temperature between above 1100 $^\circ$C in which the austenite grain growth can occur. Grain growth is affected by the presence of precipitates and their solubility at high temperatures, as well as the width of the zone itself.

Weld-metal microstructure depends on the carbon content, alloy content, temperature, cooling rate and the time it was exposed to a high temperature. Higher heat input causes coarser grain size since the steel is at higher temperature of the coarsening temperature for longer time. However, by adding refining elements such as titanium, vanadium, niobium and aluminum, a finer grain size HAZ can be obtained. The structure of FZ and HAZ has a significant effect on the weld final properties. The coarser columnar structure is susceptible to hot cracking while a finer grain structure, a distorted columnar structure or an equi-axed structure are more resistant. The weld pool shape and welding speed also has a strong effect on the microstructure of the welded specimen Figure 2-7. The grain structure close to the fusion weld line is dominated either by epitaxial growth when the base metal and the weld metal have the same crystal structure or by nucleation of new grains when they have different crystal structures. In multiple welds, the weld bead undergoes subsequent heating and cooling cycles. Therefore the peak temperature at the first pass doesn't affect the final microstructure in HAZ if one the subsequent passes introduce a higher Tp at that point.

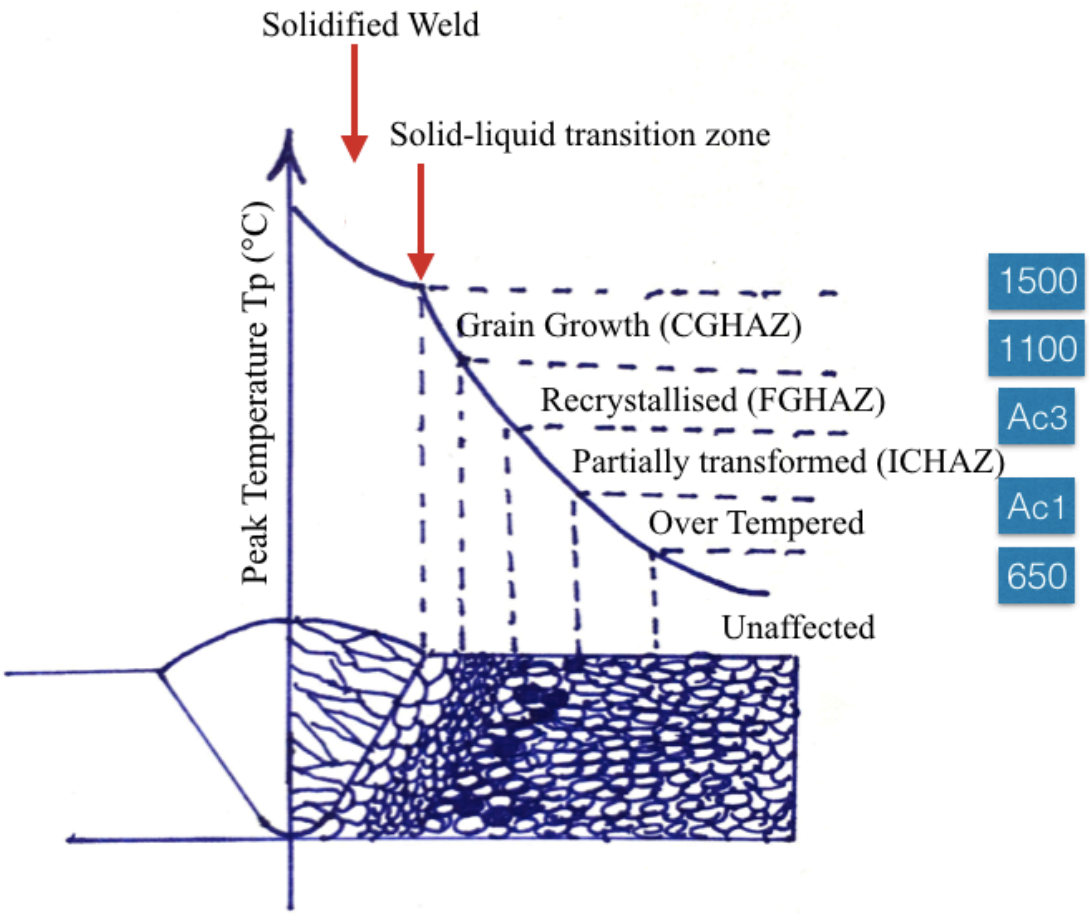


Figure 2-7 Schematic diagram of the various sub-zone of the heat-affected zone*(Easterling 1992) (Acevedo, Drezet, and Nussbaumer 2013)*

### 2.2.1 CCT Diagrams

During welding, depending on the cooling rate, different transformation products may appear. Therefore it is important to have an understanding of *Continuous Cooling Transformation* (*CCT*) diagrams (Easterling 1992). CCT diagram shows the extent of a transformation as a function of time for a continuously decreasing temperature Figure 2-8. CCT diagrams are used to predict the microstructure and consequently the properties of the products resulted from a specific cooling rate. They can also be used to prevent the formation of unwanted microstructure, e.g. too hard or too soft phases.

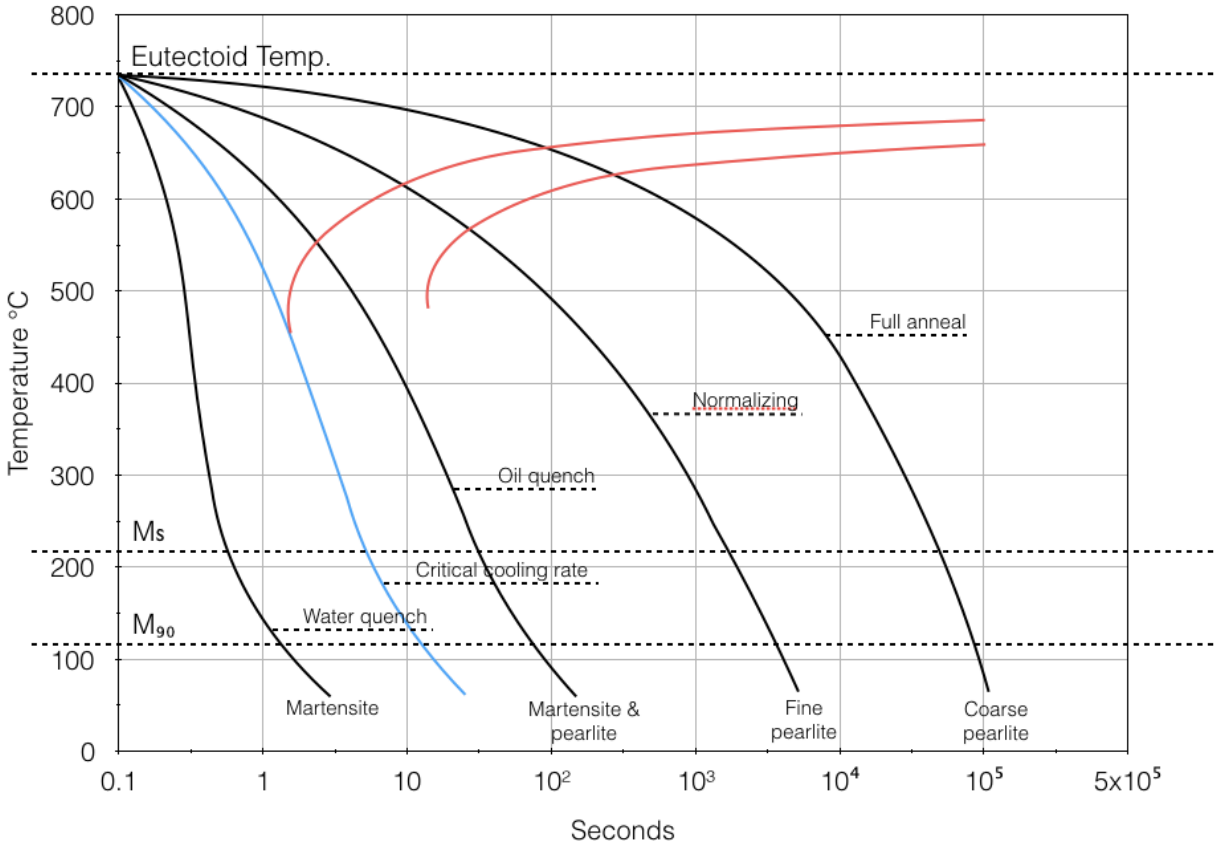


*Figure 2-8 continuous cooling transformation (CCT) diagrams.*

# 3 Computational weld modeling (CWM)

*Computational Welding Modeling (CWM)* has been increasingly used during the past two decades. CWM enables optimization of welding process through cost reduction, improved fatigue life, etc. It also gives the possibility of numerical estimation of welding parameters that are impossible to measure in an experiment such as evolution of microstructure, temperature distribution and stress development. Therefore, CWM can optimize the welding manufacturing factors and consequently improve the quality of the products. Although it is less expensive and more rapid than the experimental and trial and error methods, it introduces complexity due to the non-linear temperature-dependent properties and none linearity of the material's behavior at high temperatures. Figure *3-1*shows the increasing trend in welding simulation according to Lindgren (2001) review on finite element modeling of welding components. Hibbit and Marcal were the pioneers of CWM (according to Goldak 2005). Comprehensive reviews of the work done in this domain can be found in Lindgren (2007), Radaj (2003), and Grong (1997).

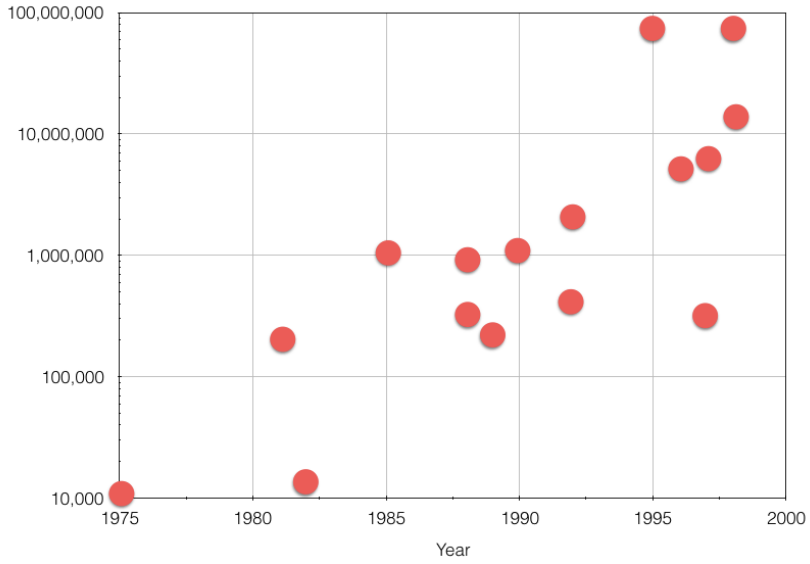


Figure 3-1 Size of computational models of welding measured by degrees of freedom multiplied by number of time steps versus year of publication of work.(until the beginning of 21$^{st}$ century) *(L.-E. Lindgren 2001).*

## 3.1 Thermal Analysis

The thermal analysis calculates the heat transfer resulting from the thermal load of the moving welding torch. The first step to simulate welding residual stress is the thermal analysis. DFLUX subroutine as defined for use with ABAQUS, is used to define the welding torch heat input as a concentrated flux. The subroutine is developed with the FORTRAN language. The heat source travels along the weld line to simulate the torch movement. In the current thesis a 3D simulation of moving heat source with a distributed heat flux is performed. Fourier developed the basic theory of heat flow which later was applied to moving heat sources by Rosenthal and Rykalin (John A. Goldak 2005) .The heat input generated from the weld is measured according to the Equation3-1 .

$$Q = UI\eta \qquad \text{Equation3-1}$$

Where $U$ is the voltage [V], $I$ is the current [A] and $\eta$ is the arc efficiency factor which shows how much of the energy is transferred to the material being welded Table 3-1Arc efficiency factor is used to take into account the energy loss during the conversion of electrical energy to thermal energy that is absorbed by metal. Efficiency factors for different welding procedures are also shown in the Table 3-1(Grong, O 1997) .

*Table 3-1*.welding efficiency factor

| Welding process | SAW Steel | SMAW Steel | GMAW CO2-steel | GMAW Ar-steel | GTAW Ar-steel | GTAW HE-Al | GTAW AR-Al |
|---|---|---|---|---|---|---|---|
| η | 0.91-0.99 | 0.66-0.85 | 0.75-0.93 | 0.66-0.7 | 0.25-0.75 | 0.55-0.80 | 0.22-0.46 |

### 3.1.1 Welding Heat Source

It is important to choose a proper welding heat source since the accuracy of the model largely depends on the chosen heat source. The most popular solution of welding heat input is developed by Rosenthal (1946) and later by Rykalin (1974) who used the basic theory of Fourier. Rosenthal's solutions made analysis of the welding process possible for the first time. Equation 3-2 presents Rosenthal thick plate solution:

$$T - T_0 = \frac{q_0}{2\pi\lambda}\left(\frac{1}{R}\right) exp\left[-\frac{v}{2a}(R + x)\right] \qquad \textit{Equation 3-2}$$

Due to its simplifying assumptions, Rosenthal model yields some errors for evaluated temperatures in or near FZ and HAZ, but nevertheless it is useful for a quick and rough estimation of welding temperature field. The research for analytical solutions has been followed by other researchers (Christensen, Davies, and Gjermundsen 1965; Eagar and Tsai 1983; Fachinotti, Anca, and Cardona 2011); see (Radaj 2003)and (Grong 1997) for a more complete bibliography.

Accuracy of the heat transfer model largely depends on the correct estimation of heat input energy, and also chosen heat source model. Pavelic et.al (1969) first suggested a Gaussian distribution of heat flux for welded components. The simplest heat source is a circular area distribution deduced by Rykalin with the Gauss normal (bell curve) distribution.

$$q_{area}(x, y) = \frac{3Q}{\pi r_{0.05}^2} exp\left(\frac{3(x^2 + y^2)}{r_{0.05}^2}\right) \qquad \textit{Equation 3-3}$$

In Equation 3-3:

$(x, y)$ : local coordinates with the origin of local coordinate system on the center of weld torch on the plate surface;
$q_{ar}(x, y)$ : location-dependent area-specific heat power density [W/m$^2$];
$Q$ : Total heat input power [W];
$r_{0.05}$ : Radius of circular surface heat source (from measurements), reduced by 5%.

Circular surface heat distribution lacks enough accuracy for weld methods with deep heat penetration such as arc and beam welding. It also doesn't show the fusion zone geometry thoroughly, as it assumes a constant heat source density. To overcome this limitation, heat sources in hemispherical and semi-ellipsoidal shapes with Gaussian power density distribution were presented (J. A Goldak and Akhlaghi 2005), as shown in equations Equation 3-4 and Equation 3-5, respectively:

$$q_{vol} = \frac{6\sqrt{3}Q}{\pi\sqrt{\pi}\, r_{0.05}^3} exp\left[-\frac{3(x^2+y^2+z^2)}{r_{0.05}^2}\right] \qquad \textit{Equation 3-4}$$

$$q_{vol} = \frac{6\sqrt{3}Q}{\pi\sqrt{\pi}\, x_{0.05} y_{0.05} z_{0.05}} exp\left[\left(\frac{x}{x_{0.05}}\right)^2 + \left(\frac{y}{y_{0.05}}\right)^2 + \left(\frac{z}{z_{0.05}}\right)^2\right] \qquad \textit{Equation 3-5}$$

In Equation 3-4 and Equation 3-5:

| | |
|---|---|
| $(x, y, z)$ | : local coordinates with the origin of local coordinate system on the center of weld torch on the plate surface; |
| $q_{vol}(x, y, z)$ | : location-dependent volume heat power density [W/m$^3$]; |
| $Q$ | : Total heat input power [W]; |
| $r_{0.05}$ | : radius of spherical heat source (from measurements), reduced by 5%; |
| $x_{0.05}$ , $y_{0.05}$ , $z_{0.05}$ | : Length, width, and depth of the measured heat source, reduced by 5%. |

A non-asymmetric three-dimensional model called double ellipsoidal Gaussian heat source, proposed by Goldak et al. (1984), is the most widely used model for fusion weld modelling. Two different ellipse shapes can be defined for front and rear sides of the weld pool. Power density distribution inside the front and rear parts of the heat source are given as:

$$\begin{cases} q_{vol,f} = f_f \dfrac{6\sqrt{3}\,Q}{\pi\sqrt{\pi}ABC_f} \exp\left\{-3\left[\left(\dfrac{x}{A}\right)^2 + \left(\dfrac{y}{B}\right)^2 + \left(\dfrac{z}{C_f}\right)^2\right]\right\} \\ q_{vol,r} = f_r \dfrac{6\sqrt{3}\,q}{\pi\sqrt{\pi}ABC_r} exp\left\{-3\left[\left(\dfrac{x}{A}\right)^2 + \left(\dfrac{y}{B}\right)^2 + \left(\dfrac{z}{C_r}\right)^2\right]\right\} \end{cases} \qquad \textit{Equation 3-6}$$

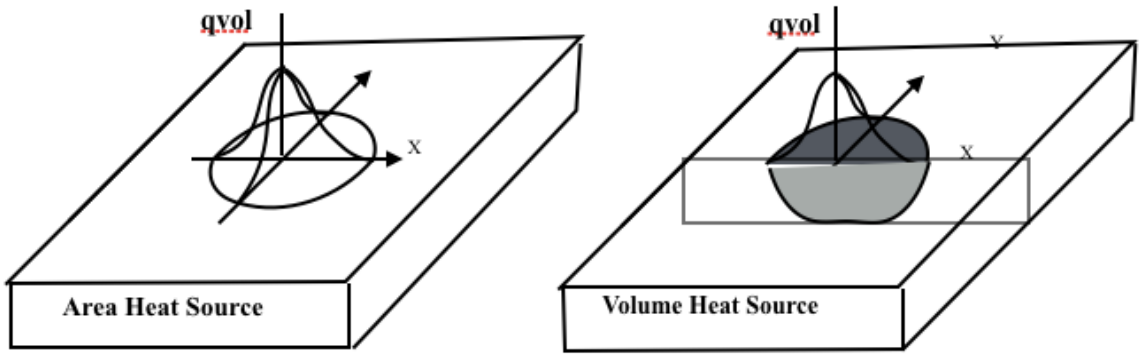


Figure 3-2 Distributed weld heat source, circular area heat source (a) and hemispherical volume source (b) with Gaussian (normal) distribution of area-specific energy density $q_{ar}$ [J/mm$^2$/s] and volume-specific source $q_{vol}$ [J/mm$^3$/s] *(Radaj 2003)*.

Where $Q$ is the total heat flux, $q_{vol,f}$ and $q_{vol,r}$ are power flux densities in the front and rear parts, respectively. A, B, $C_f$ , and $C_r$ are the geometrical parameters of the heat source, as shown in Figure 3-3. $f_r$ and $f_f$ are the heat portions which are deposited in the rear and the front of the heat source, respectively. It should be noted that the total heat energy is still un-changed ($f_f + f_r = 2$ but$f_f \neq f_r \neq 1$).

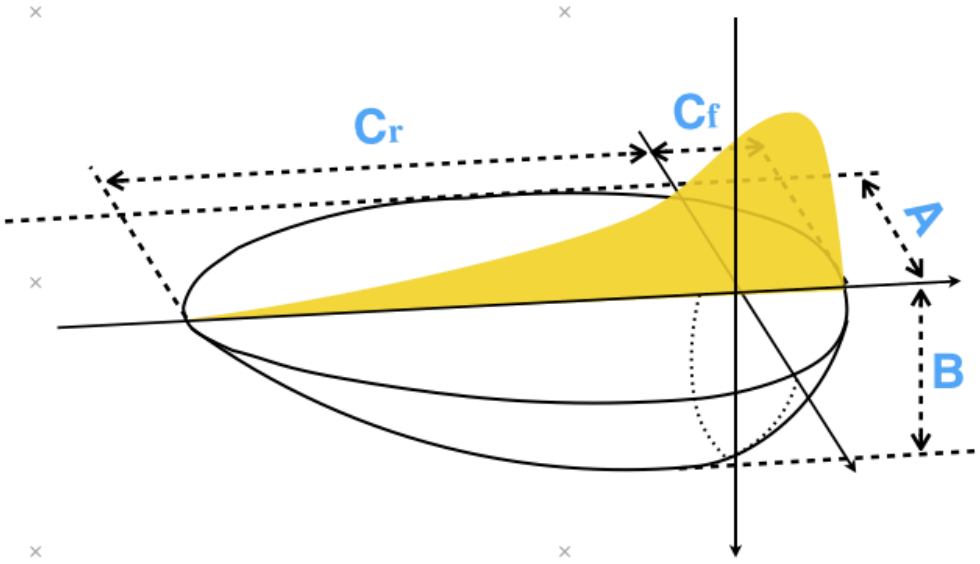


Figure 3-3. double ellipsoidal heat source

Soares (M. Hashemzadeh 2014) has compared Gaussian, semi ellipsoidal, and double ellipsoidal heat source models for fusion welds in stainless steel and has concluded that semi ellipsoidal and double ellipsoidal models give more accurate results for calculated residual stress field.

### 3.1.2 Heat loss during welding

The local temperatures during welding are considerably higher than the surrounding material; so heat loss will occur due to transfer of thermal energy by means of conduction, convection, and radiation.

#### *3.1.2.1 Conduction*

Heat can transfer through conduction in solids. When the material is heated, molecules will gain more kinetic energy and vibrate more. These molecules then bump into nearby particles and the increased energy is passed to other particles. This continues and passes the energy from the hot section to the colder sections of the substance. Thermal conductivity is a material property, which depends on the temperature and molecular bonding.

$$\vec{q} = -K\nabla T \qquad \text{(Equation 3-7)}$$

Where $\vec{q}$ is the heat flux through conductivity, K is the material's thermal conductivity in [W/m/K] (also sometimes denoted by $\lambda$), and $\nabla$T is the temperature gradient.

#### 3.1.2.2 Convection

In liquid and gaseous state, heat energy is transferred from hot places to cooler places by convection. Convection occurs when particles with higher heat energy in a liquid or gas move and replace particles with less heat energy.

$$q = h.A_s(T_s - T_b) \quad \text{(Equation 3-8)}$$

Where $A_s$ is the contact surface area of solid-fluid in heat transfer, $T_s$ is the surface temperature, $T_b$ is the temperature of the fluid and h is the heat transfer coefficient in [W/m$^2$/K].

#### 3.1.2.3 Radiation

Radiation is the transfer of heat that does not rely upon any medium. Heat can be transmitted through an empty space by thermal radiation and can be described as follow.

$$q = \varepsilon.\sigma(T^4 - T_\infty^4) \quad \text{(Equation 3-9)}$$

Where ε is the emissivity factor, σ is the Stefan-Boltzmann's constant, T is the source temperature and $T_\infty$ is the surrounding temperature

#### 3.1.2.4 Combined thermal boundary conditions

Convection and radiation can be considered as the thermal model boundary conditions separately, or they can be combined (ACEVEDO, 2011) as follow:

$$q_{rad} = \varepsilon_s\sigma_0(T^3 + T^2T_0 + TT_0^2 + T_0^3)(T\text{-}T_0) \quad \textit{Equation 3-10}$$

$$q_{total} = q_{convection} + q_{radiation} = h_{total}(T)(T\text{-}T_0) \quad \textit{Equation 3-11}$$

$$h_{total} = h_{convection} + h_{radiation} = h_c(T) + \varepsilon\sigma_0(T^3 + T^2T_0 + TT_0^2 + T_0^3) \quad \textit{Equation 3-12}$$

### 3.1.3 Specific heat capacity

Specific heat capacity is the energy required to increase the temperature of the unit mass of the material by 1 K. Specific heat capacity is also temperature dependent, and can be derived from the literature or software such as JMatPro.

### 3.1.4 Latent heat

Latent heat of a physical transformation is the amount of energy absorbed or released during the changes in physical state. This energy comes from the potential energy of the material's bonding. During the transformation (e.g. melting/solidification) the temperature remains constant and thermal energy is consumed/released for state-change. The latent heat associated with melting or freezing is called *heat of fusion* and the heat associated with vaporizing or condensing is called *heat of vaporization*.

During welding, at the front edge of the weld pool where the substance is melting, latent heat of fusion is supplied to melt the material. On the other hand, at the trailing edge of the pool, the heat must be released to solidify the melted material. In order to calculate the latent heat, an equivalent specific heat ($C_p$) can be defined as follows:

$$H = \int_{T_{solidus}}^{T_{liquidus}} \rho C_p T d(T) + h_1$$ *Equation 3-13*

Where H is enthalpy, $C_p$ is specific heat capacity, ρ is density and $h_l$ is latent heat of fusion. Using a constant equivalent specific heat capacity ($C_{eq}$) in the range of mushy zone and assuming $C_p$ as a linear function of temperature, equivalent heat capacity can be calculated.

$$C_{eq} = \frac{H}{\rho(T_{solidus} - T_{liquid})}$$ *Equation 3-14*

In *Equation 3-6*, $T_{solidus}$ and $T_{liquid}$ are solidus and liquidus temperatures, respectively and can be measured experimentally. For steel material with known composition, $T_{solidus}$ and $T_{Liquid}$ can be evaluated from the following empirical relations:

$T_{Solidus}$=1535−200 (%C) −12.3 (%Si) −6.8 (%Mn) −124.5 (%P) −189.3 (%S) −4.3 (%Ni) −1.4 (%Cr) −4.1 (%Al) *Equation 3-15*

$T_{Liquid}$=1537−88 (%C) −8 (%Si) −5 (%Mn) −30 (%P) −25 (%S) −4 (%Ni) −1.5 (%Cr) −5 (%Cu) −2 (%Mo) −2 (%V) −18 (%Ti) *Equation 3-16*

Finally, apparent specific heat capacity for the whole temperature range is given by:

$$C_p = \begin{cases} C_{p,solid} & T < T\_solid \\ \dfrac{C_{p,solid} + C_{p,liquid}}{2} + \dfrac{h_1}{\rho(T_{liquid} - T_{solid})} & T_{solid} \le T \le T_{liquid} \\ C_{p.liquid} & T > T_{liquid} \end{cases}$$ *Equation 3-17*

Figure 3-4 shows the temperature-dependent specific heat values according to Withers (Withers and Bouchard 2006) for steel (S355) and the European Standard for the structural fire design of steel structures Eurocode 3(EC3). The Peak at 750°C corresponds to solid-state α to γ phase transformation.

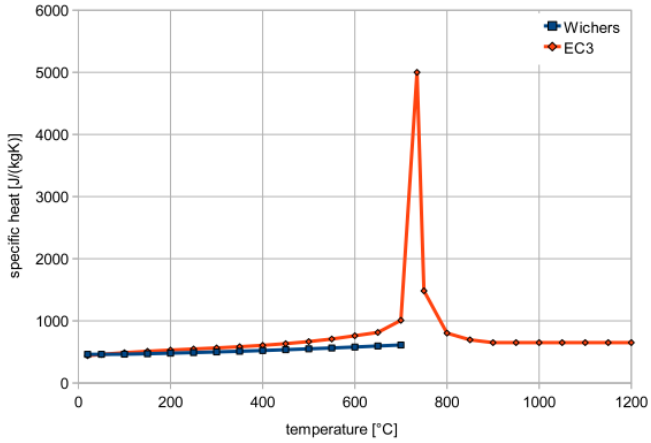


Figure 3-4 Temperature-dependent apparent specific heat capacity values, The peak at around 750°C corresponds to solid-state α to γ phase transformation*(Krummenacker 2011)*.

## 3.2 Mechanical and Metallurgical Analysis

During welding using LTT materials, additional volume change strain is induced due to solid-state phase transformation along with thermal strains. Accordingly, the total strain can be written as follow:

$$\Delta\varepsilon = \Delta\varepsilon^{E} + \Delta\varepsilon^{p} + \Delta\varepsilon^{T} + \Delta\varepsilon^{\Delta v} \qquad \textit{Equation 3-18}$$

Which represents changes in strain due to elastic ( $\Delta\,\varepsilon^{E}$) and plastic ($\Delta\varepsilon^{P}$) deformations as well as thermal expansion/contraction ($\Delta\varepsilon^{T}$). $\Delta\varepsilon^{\Delta v}$ takes into account the volume change during phase transformation. According to Koistinen–Marburger (Koistinen and Marburger 1959) relationship (KM), $\Delta\varepsilon^{\Delta v}$can be computed for austenite to Martensite phase transformation as follows:

$$\Delta\varepsilon^{\Delta v} = \Delta f_M . \Delta\varepsilon^{v*} = \{-k.exp[-k(M_s - T)]\}\Delta T . \Delta\varepsilon^{v*} \qquad \textit{Equation 3-19}$$

Where $\Delta f_M$, is the increment of martensite fraction, T is the current temperature, $\Delta\varepsilon^{v*}$ is the strain due to volume change corresponding to fully martensitic transformation and k is the transformation constant (Deng 2009). $\Delta\varepsilon^{v*}$ can be calculated from the diagram of strain due to volumetric change versus temperature for the base metal and the weld metal (Figure 3-5).

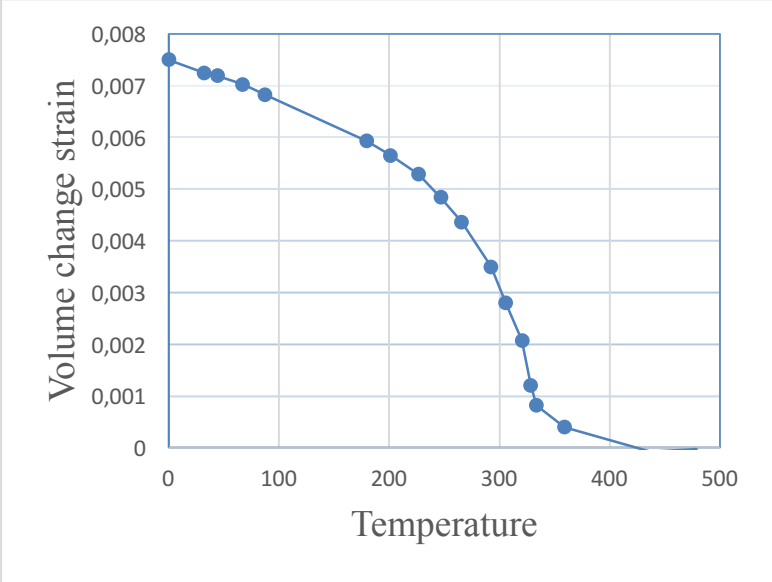


*Figure 3-5. Volumetric change of 9Cr–1Mo-weld metal during cooling.(Deng 2009)*

### 3.2.1 Hardening Models

Hardening rules can define changes in the yield surface while plastic deformations occur in a cyclic loading. Three hardening models are more common in the welding simulation; *isotropic, kinematic and combined hardening model* (Houlsby and Puzrin 2006).

- In the isotropic model, the yield surface expands while it keeps its shape and its center i.e. the yield surface grows in tension and compression analogously. As shown in Figure 3-6 when the material yields at point A, it starts its plastic deformation. The stress increases due to work hardening, which leads to increased material strength. When compression cycle starts at point B, the yield will occur in point C, with the same ordinate of point B but with a negative sign. During CD path, the material continues to harden. When the loading changes sign for another time, the material will yield at a higher stress (point E,$\sigma_E = -\sigma_D$).
- On the other hand, in kinematic hardening, the yield surface keeps its size but gets translated in the stress space Figure 3-7. It has a loading cycle identical to that of isotropic hardening (OAB). While unloading, material yields at a lower stress than the isotropic one. In the reverse loading, the material yields at a higher stress level but still on the AB line.
- In the combined model both the size of yield surface is increased while its center-point position changes Figure 3-7. The change in the yield surface is a linear combination of the expansion (isotropic model) and translation (kinetic model).

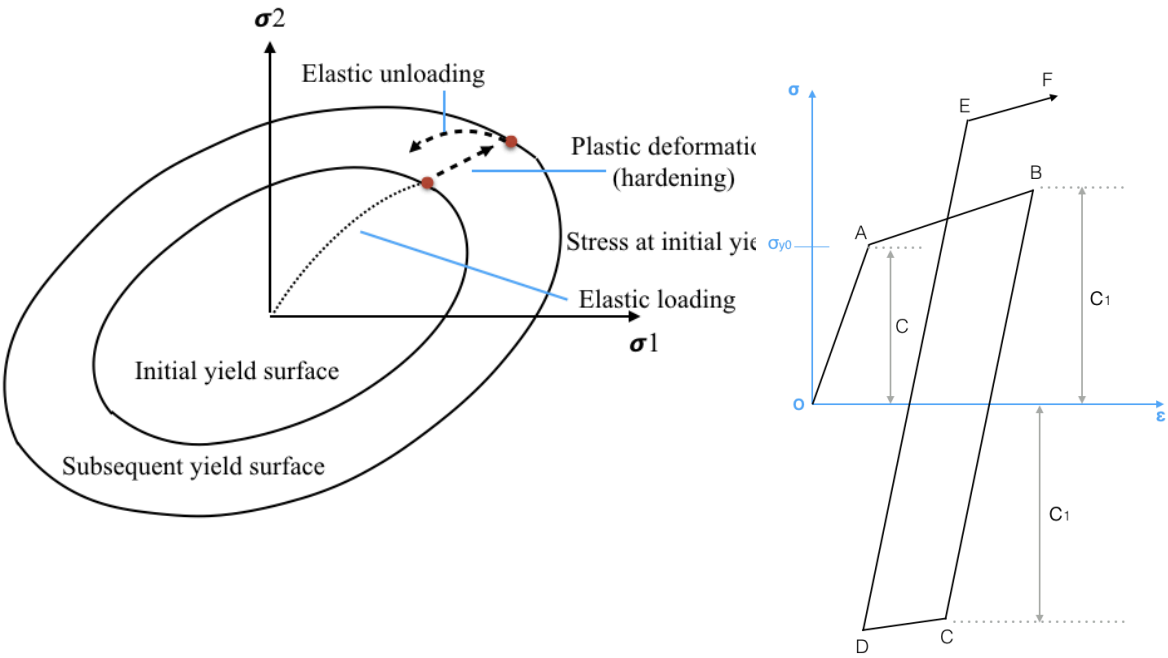


(a) (b)

*Figure 3-6*. Isotropic hardening *(Houlsby and Puzrin 2006)*.

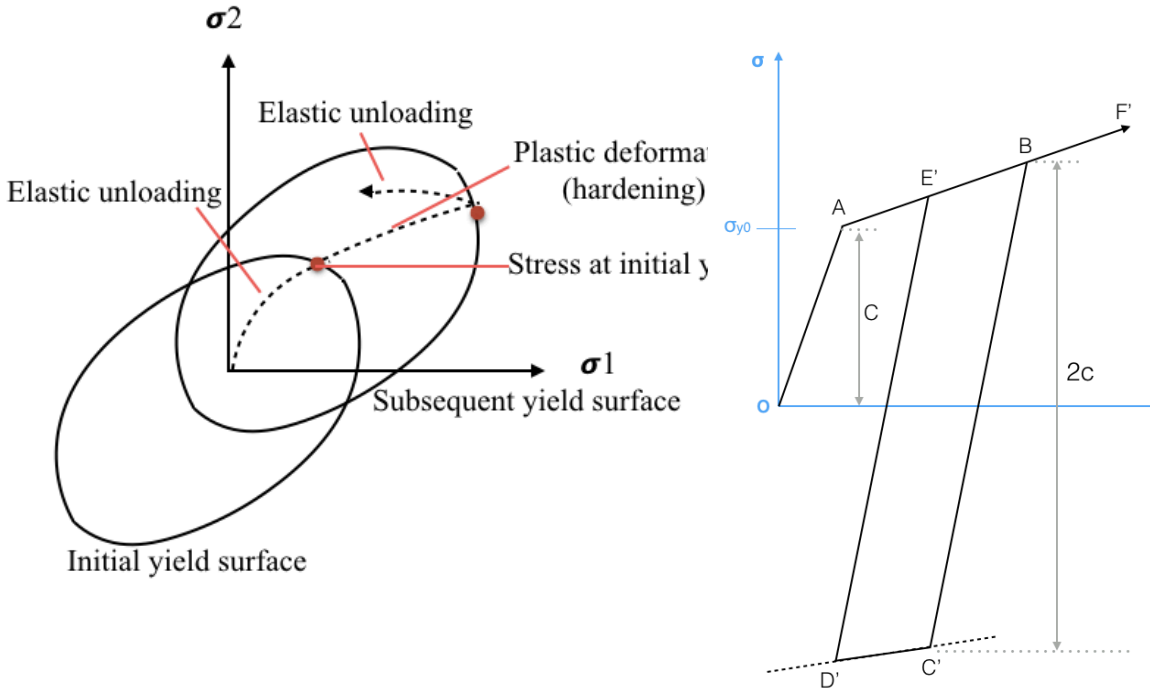


(a) (b)

*Figure 3-7*.Kinematic hardening *(Houlsby and Puzrin 2006)*.

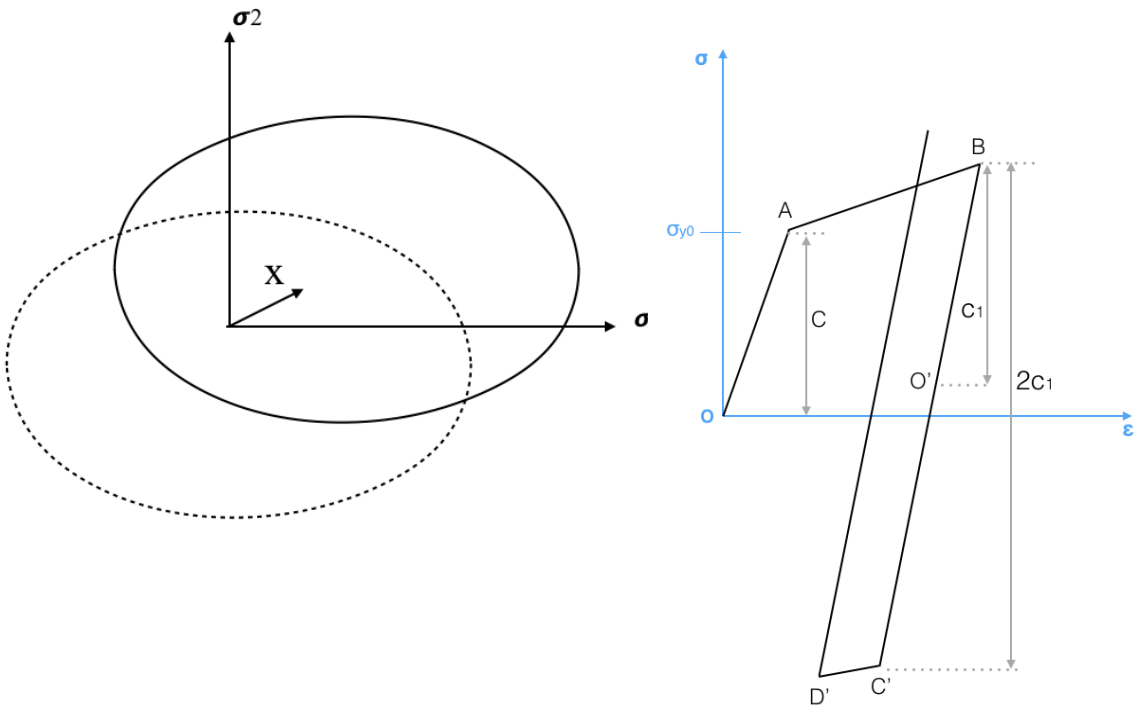


*Figure 3-8. Combined hardening model (Houlsby and Puzrin 2006).*

### 3.2.2 Thermal Expansion

Heating and cooling cycles during welding can cause expansion and contraction. The expansion coefficient varies with different phases and temperatures. Therefore, non-uniform expansion and contraction lead to plastic deformation and residual stress in the welded pieces. Different types of dimensional changes in the welded pieces include *Transverse shrinkage, Longitudinal Shrinkage, Angular Distortion and* Buckling Figure 3-9.

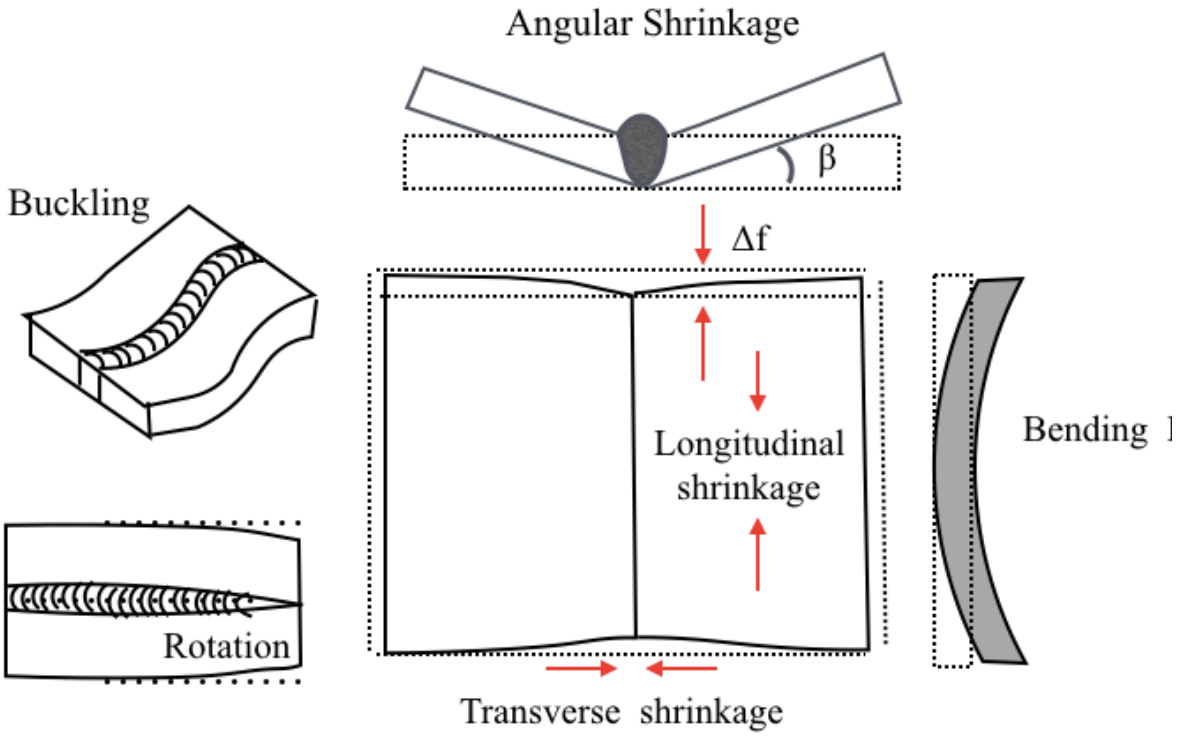


Figure 3-9 different types of welding distortion *(John A. Goldak 2005)*

### 3.2.3 Phase transformation

Deng (2009) studied the effects of solid-state phase transformation on welding residual stresses and distortions in steels. For the two studied materials (low carbon steel S15C and medium carbon steel S45C), his results showed that martensitic transformation considerably affects residual stress and distortion.

According to KM model for displacive transformation (Koistinen and Marburger 1959), Martensite volume fraction can be calculated as follow:

$$p_i = p_a\left(1 - e^{-\alpha(M_s - T)}\right) \qquad \textit{Equation 3-20}$$

Where $p_i$ is the volume fraction of Martensite, $p_a$ is retained austenite volume fraction. $M_s$ is the Martensite start temperature and α is a constant, which depends on the material. Leblond equation (Leblond et al. 1985) can be used in case of phases being in the equilibrium. It can be applied to both diffusion- and diffusion less-controlled transformations[1]. For the basic case of phase transformation in isothermal conditions, Leblond equation is presented in the form:

$$\dot{z}_i(t) = \frac{dz_i}{dt} = \frac{z_{i,eq}(T) - z(t)}{\tau} \qquad \textit{Equation 3-21}$$

[1] For diffusionless transformations, KM model is preferable over Leblond model, from computational point of view, since it is independent of time and time-derivatives.

Where $z_i$ is the time-dependent volume fraction of phase i, $z_{eq}$ is the equilibrium volume fraction of phase i as a function of temperature T, and $\tau$ is a parameter representing characteristic time of transformation (the shorter the $\tau$, the faster the transformation occurs). This equation can be extended to non-isothermal conditions with several coexisting phases and different transformations.

There is an interaction between metallurgical phenomena and mechanical behavior of material during welding (Figure 1-1). On the one hand, phase transformations occurring during heating and cooling cycles of welding, causes mechanical strains; on the other hand when phase transformation takes place in a material which is under mechanical stresses, permanent (plastic) strains occur, known as *Transformation-Induced Plasticity (TRIP)*. This is an irreversible length change that is produced during phase transformation under small external stress (lower than yield stress of the weaker material phase) (Taleb, Cavallo, and Waeckel 2001)(Fischer et al. 2000). Greenwood and Johnson first explained the TRIP without distinguishing a diffusive or displacive transformation in their model (Fischer et al. 2000). Using LTT material, transformation induced plasticity can be utilized to control residual stresses produced during welding (Ramjaun, Stone, Karlsson, Kelleher, et al. 2014).

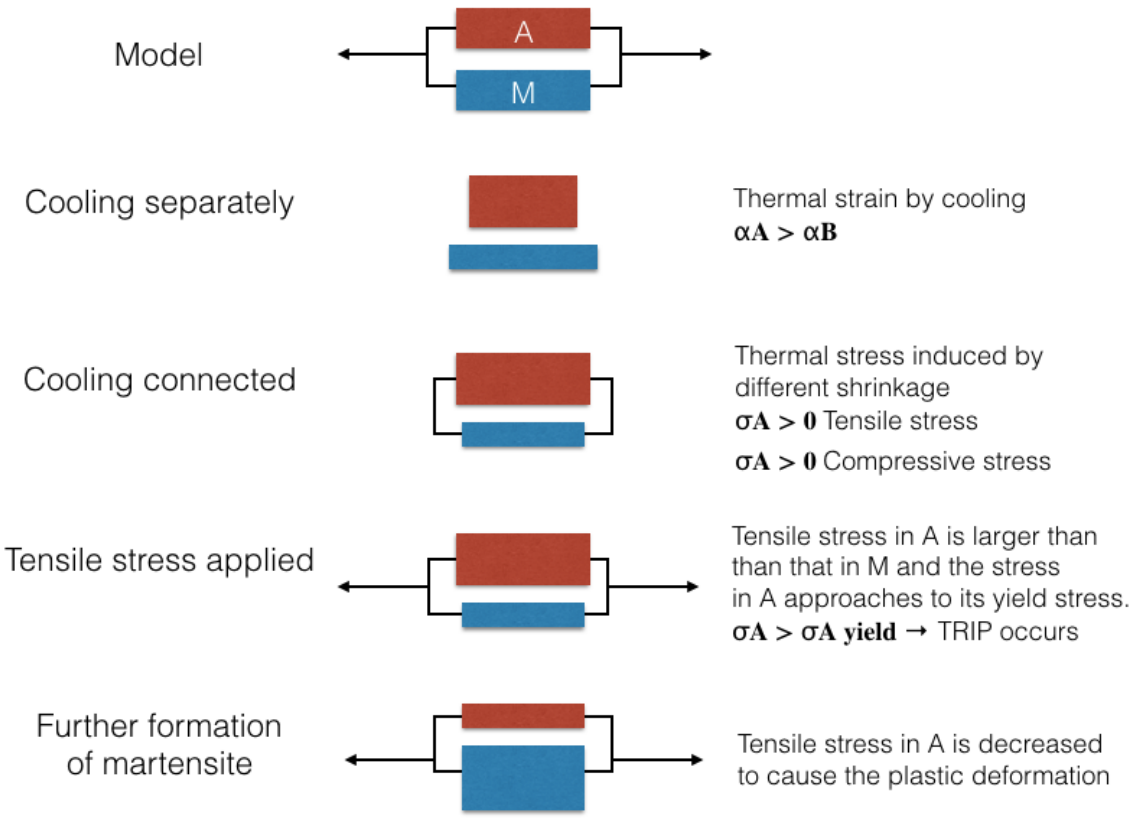


Figure 3-10 . A model of transformation induced plasticity*(Deng and Murakawa 2013a)*

## 3.3 Implementation in current study

In the current thesis a transient 3D simulation of moving heat source with a distributed heat flux is performed. First a repeated analysis of a single pass weld is performed to validate Abaqus as good simulation software for welding simulation. Then a heat transfer analysis of a plate with 3 pass of weld is performed. Two different heat source model is used and compared. Abaqus user subroutine DFLUX is used to define the welding torch heat input as a volumetric heat flux. The subroutine is developed with the FORTRAN language. The heat source travels along the weld line to simulate the torch movement. In the next phase of the work, Metallurgical analysis is performed to model the phase transformation during and after welding. User subroutine Hetval is used to model phase transformation. Finally the data from the previous heat transfer analysis and metallurgical analysis are used as an input file for mechanical analysis. Figure 3-11shows the schematic of simulation procedure.

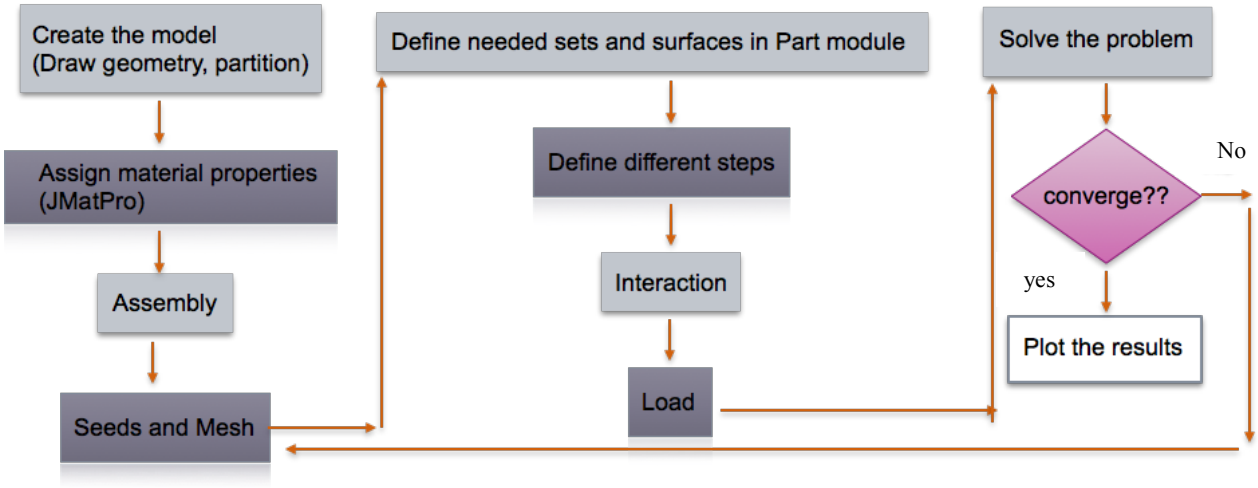


*Figure 3-11 the simulation steps*

# 4 Welding simulation of NeT round robin specimen

## 4.1 Introduction

A round robin study is an analysis or measurement that is performed several times with the same details in different laboratories using different equipment. The parameters to be measured are the same for all participants in the study, but the methods of measurement/analysis can vary. A Round robin procedure can help in determining the precision of a considered test or analysis method. In this section, a round robin project, which was performed to study residual stresses and distortion in welded pieces both numerically and experimentally, is described (El-Ahmar 2007)(Smith and Smith 2009)(Dong and Hong 2002)(Ficquet et al. 2009)(Smith and Smith 2009)(Truman and Smith 2009). In the original study, four identical specimens made of AISI Type 316L austenitic stainless steel plate were manufactured with the dimensions of 180mm*120mm*17mm and a single Tungsten Inert Gas (TIG) weld bead with the length of 60mm was deposited in the centerline of the plates depicted in Figure 4-1. To clear thermal history and residual stresses induced during manufacturing, all four samples were solution heat treated for 45 minutes at 1050℃, then cooled down in the furnace. No phase transformation occurred during the annealing process. Results from numerical simulation indicate that an isotropic hardening model leads to over-conservative results of stress especially in longitudinal stresses while non-linear kinematic hardening model gives the most accurate prediction of residual stresses ((Truman and Smith 2009)). But recently Wohlfahrt (Wohlfahrt et al. 2012) concluded that isotropic hardening model gives better results in austenitic steels.

To repeat the above simulation using Abaqus, thermal and mechanical data were derived from the literature as mentioned in tables Table 4-1, Table 4-4 and

| Element | Carbon | Manganese | Silicon | Chromium | Nickel | Molybdenum | Phosphorous | Sulfur | Iron |
|---|---|---|---|---|---|---|---|---|---|
| Percentage by weight | 0.03 | 2.00 | 0.75 | 16-18 | 10-14 | 2-3 | 0.04 | 0.03 | Bal |

In this work, the round robin procedure was solved by Abaqus to validate it as a simulation method for welding residual stresses.

Table 4-1 NeT task group 1 simulation round robin participants.*(Ficquet et al. 2009)*.

| Organization | abbreviation | Reference |
|---|---|---|
| British Energy and Frazer–Nash Consultancy, UK | BE-FNC | Ficquet et al. |
| INSA-Framatome, France | FANP | El-Ahmar et al. |
| Imperial College, London, UK | Imperial | O' Dowd et al. |
| Institute for Nuclear Research, Romania | | |
| JRC, Institute for Energy, Petten, The Netherlands | JRC_UP | Ohms et al. |
| Korea Power Engineering Company, Korea | KOPEC | |
| SERCO Assurance, UK | SERCO Bate et al | |
| University of the West of England, UK | UWE | |

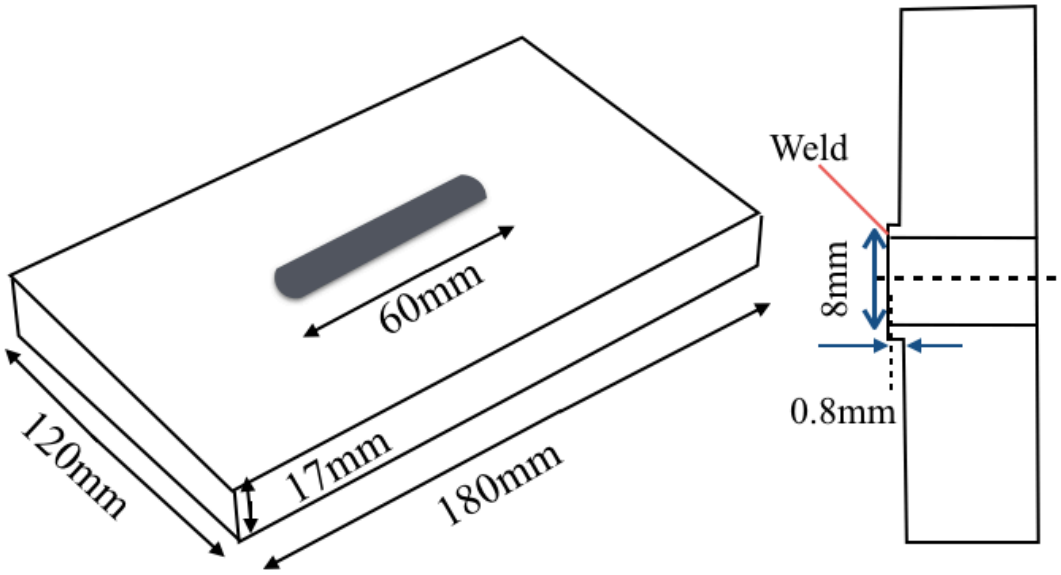


Figure 4-1 dimensions of the NET specimens

*Table 4-2 welding parameters*

| Parameter | Value | Unit |
|---|---|---|
| Welding type | TIG | - |
| Weld speed | 2.27 | mm/s |
| Heat input model | Cylindrical | — |
| Weld efficiency | 0.75 | — |
| Arc time | 26.4 | s |
| Torch travel length | 60 | mm |
| Heat input | 633 | J/mm |
| Heat source radius | 2.4 | mm |
| Heat source depth | 0.7 | mm |

*Table 4-3 material properties*

| Parameter | Value | Unit |
|---|---|---|
| Tliquid | 1483.91 | ˚C |
| Tsolidus | 1471.72 | ˚C |
| Density | 7.97E-06 | kg/mm3 |
| Latent heat of fusion | 220 | µJ/kg |

## 4.2 Thermal Analysis

Convection and radiation are considered as thermal boundary conditions in this model. Temperature-dependent convective heat transfer coefficients of 4.2 W/m$^2$K at 20℃ to 14.8 W/m$^2$ K at 2500℃ are applied to the top face of the model and the constant values of 7 and 3.5 W/m$^2$ K were applied to the sides and bottom faces of the model, respectively. The radiative

heat transfer with an emissivity of 0.4 is also assumed. It is important to have a consistent system of units. Table 4-4 depicts the chosen units that are used in the calculations.

Table 4-4 consistent table of units.

| Physical quantity | Symbol | **Dimension** |
|---|---|---|
| Mass | M | M |
| Length | L | L |
| Time | t | T |
| Temperature | T | - |
| Density | ρ | $ML^3$ |
| Force | F | $MLT^{-2}$ |
| Stress | σ | $ML^{-1}T^{-2}$ |
| Thermal conductivity | λ | $MLT^{-3}$ |
| Mass specific heat | $C_p$ | $L^2T^{-2}$ |
| Heat energy | E | $ML^2T^{-2}$ |
| Heat power | Q | $ML^2T^{-3}$ |
| Volumetric heat flux | q | $ML^{-1}T^{-3}$ |
| Film coefficient | h | $MT^{-3}$ |
| Thermal expansion | $T^{-1}$ | - |

## 4.3 Material properties

Table 4-5 shows the chemical composition of steel 316L. Figure *4-3* depicts the temperature-dependent material thermal properties. Heat conductivity at the temperature above the solidus is assumed to be three times the conductivity of solidus temperatures as can be seen in Figure 4-2Figure 4-2. This is done in order to take into account the convective stirring at the high velocities in weld pool.

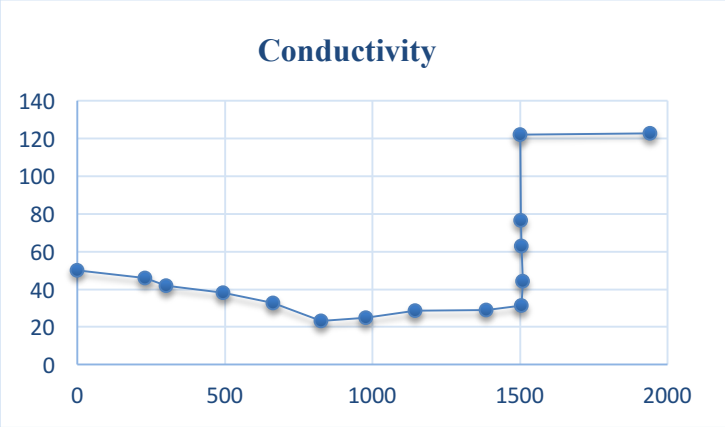


*Figure 4-2 Temperature-dependant conductivity for low alloy steel used for Finite Element Modeling (J. A Goldak and Akhlaghi 2005)*

## 4.4 Thermal load

In Abaqus, distributed thermal load and flux types can be applied with the user-defined DFLUX subroutine. It allows the user to define an arbitrary time-dependent distribution for surface or volumetric heat power density all over the computational domain. For this part of the study and for the sake of simplicity, a cylindrical heat source with uniform power density inside cylinder is chosen and the DFLUX subroutine is written in FORTRAN programming language. The

heat source is modelled as a cylinder with the height and radius of 0.7 mm and 2.4 mm, respectively. These values for cylindrical heat source size are obtained through trial and error to yield sufficiently accurate weld pool size in the analysis. From welding parameters Table 4-2, the volumetric heat flux used as the thermal load, is calculated as follows:

$$Heat\ flux = \frac{633(\mathrm{J/mm})\times 0.75\times 10^{9}\times 2}{26.4(\mathrm{s})\times 12.67(mm^{2})} = 8.52\times 10^{7}\,\frac{\mu W}{mm^{3}} \qquad \textit{Equation 4-1}$$

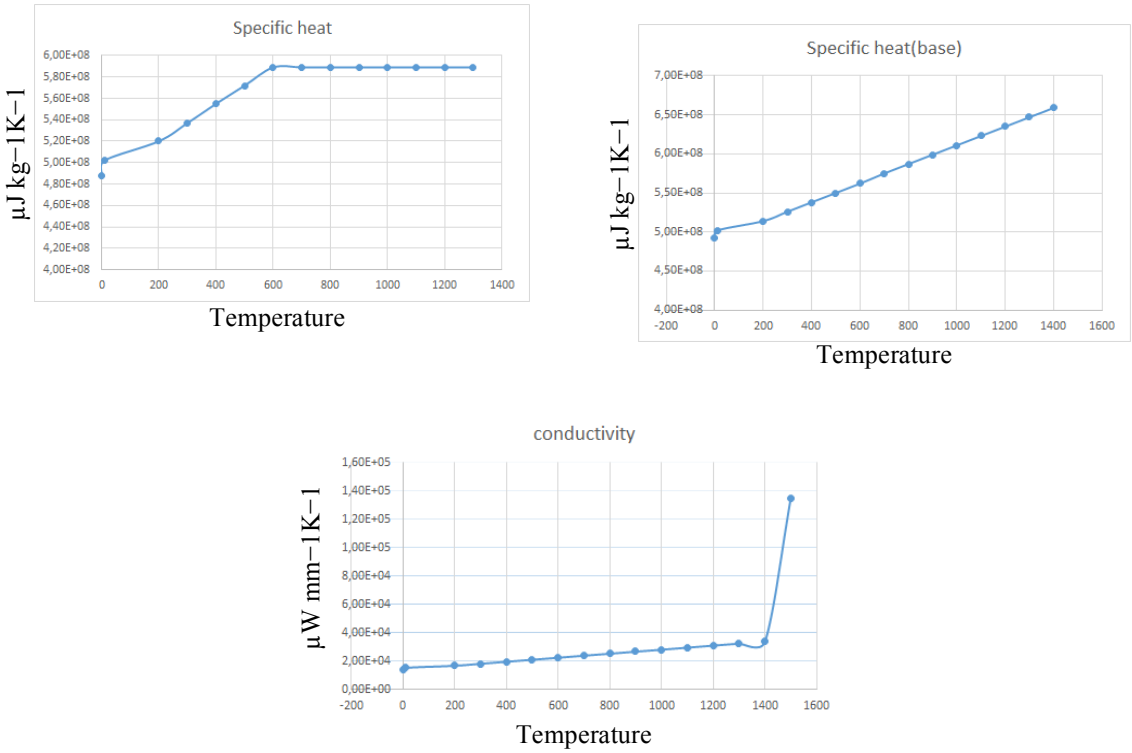


Figure 4-3. Thermal material properties Specific heat ($C_p$) for base material and weld metal, and thermal conductivity ($\lambda$) (assumed the same for all material).

## 4.5 Finite element mesh and element type

The plate is drawn in the part section in Abaqus and the bead is added by partitioning the plate. Different techniques like chamfering, volume edit and etc. is used to create the geometry. The model is constructed using 8-node linear heat transfer brick elements, called DC3D8 in Abaqus. The model contains 46067 elements and 50925 nodes.
*Figure 4-4* shows the meshed piece.

*Table 4-5* Chemical composition of steel 316L

| Element | Carbon | Manganese | Silicon | Chromium | Nickel | Molybdenum | Phosphorous | Sulfur | Iron |
|---|---|---|---|---|---|---|---|---|---|
| Percentage by weight | 0.03 | 2.00 | 0.75 | 16-18 | 10-14 | 2-3 | 0.04 | 0.03 | Bal |

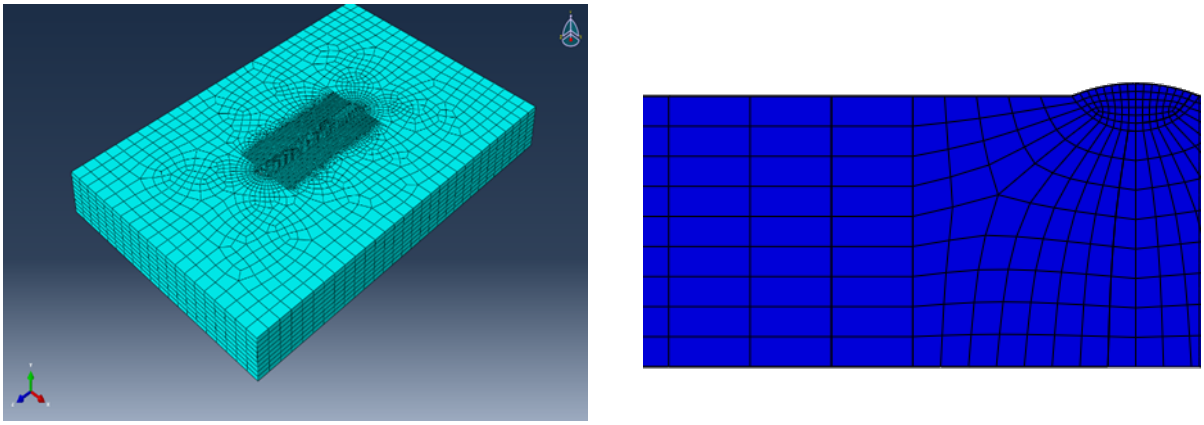

(a) (b)

Figure 4-4. Meshing *overall view (a)* and close-up of the fine mesh at weld region (b)

## 4.6 Model validation

### 4.6.1 Temperature histories

One way of validating the model is to study the temperature history derived from the model at a certain distance from the weld and compare it with the experimental data. The thermal cycle including $T_{max}$, and the time of cooling, specially cooling time from 800 °C to 500°C ($t_{8/5}$), can be considered for model validation. Fig. 24 depicts the temperature-time graph at the top surface and on the centerline of the weld.

Figure *4-6* is the results of this study calculated at a point located 8 mm away from the weld line. These plots depict the temperature at a specific point as a function of time. Considering the temperature starts from the ambient temperature and increases to the max temperature close to melting temperature $T_m$. When the torch moves away, the temperature decreases and reaches the ambient temperature again. The different positions of the HAZ are heated to different peak temperatures and decreases with increasing distance from the melting zone.

For a rough estimation of cooling times, different semi-empirical formulas (based on Rosenthal's solution) have been suggested to estimate $t_{8/5}$. For relatively thick plates, the heat dissipation takes place in three dimensions; i.e. the heat can flow in both the workpiece plane and its thickness. In this case $t_{8/5}$ can be calculated as follows ("Erklärungen Zur Abkühlzeit t8/5" 2016):

$$\Delta t_{8/5} = (6700 - 5\,T_0) \cdot Q \cdot \left(\frac{1}{500 - T_0} - \frac{1}{800 - T_0}\right) \cdot F_3 \qquad \text{Equation 4-2}$$

Where Q is the heat power (Watt), $T_0$ is preheating temperature, and $F_3$ is the seam factor in three-dimensional heat dissipation.

In the case of thin plates where the heat flow occurs only in the work piece plane (two dimensional), cooling time can be calculated as follows:

$$\Delta t_{8/5} = (4300 - 4.3T_0) \cdot 10^5 \cdot \frac{Q^2}{d^2} \cdot \left[ \left( \frac{1}{500 - T_0} \right)^2 - \left( \frac{1}{800 - T_0} \right)^2 \right] \cdot F_2 \qquad \text{Equation 4-3}$$

In Equation 4-3, Q is heat input, T0 is the preheating temperature, d is the sheet thickness and $F_2$ is the seam factor in two-dimensional heat dissipation.

Table 4-6. The values of seam factors.(Ulrich Dilthey 2006)

| Type of weld | Seam factors | |
|---|---|---|
| | $F_3$ | $F_2$ |
| Run on plate bead | 1.0 | 1.0 |
| 1st and 2nd fillet weld pass on T or cross joint | 0.67 | 0.45 to 0.67 |
| 3rd and 4th fillet weld on T or cross joint | 0.67 | 0.3 to 0.67 |
| Fillet weld on corner | 0.67 | 0.9 |
| Fillet weld on lap | 0.67 | 0.7 |
| Root layer of V-seams (opening angle 60 °, web spacing 3 mm) | 1.0 to 1.2 | rd. 1.0 |
| Root layer of double-V-welds (opening angle 50 °, web spacing 3 mm) | 0.7 | rd. 1.0 |
| Middle layers of V and double-V-welds | 0.8 to 1.0 | rd. 1.0 |
| Top layers of V and double-V-welds | 0.9 to 1.0 | 1.0 |
| I-seam 'location-counter-location-weld' | - | 1.0 |

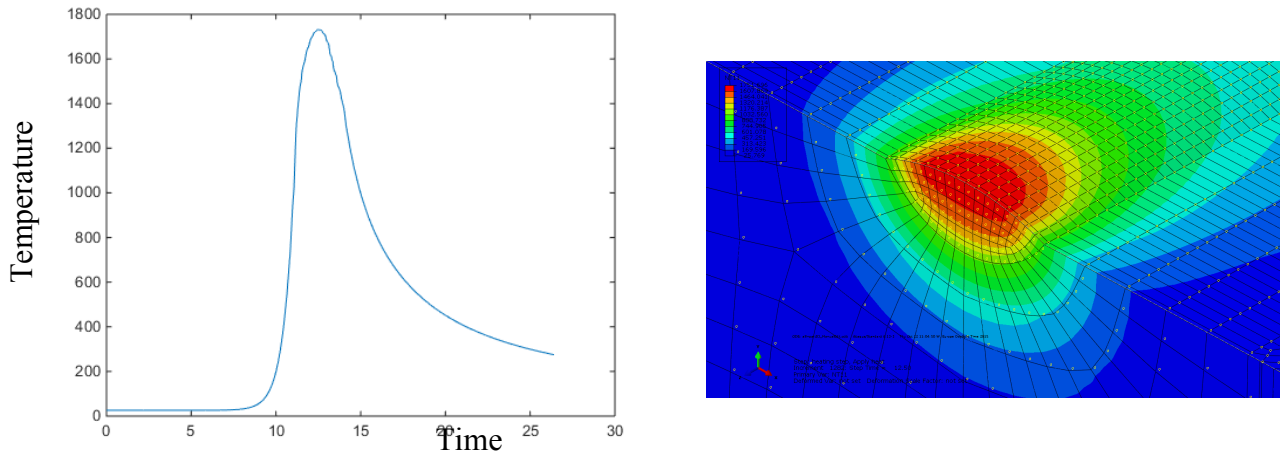


(a) (b)

Figure 4-5. Temperature-time graph at the center of surface of the FZ (a), and temperature field at the weld torch location (section view)(b).

The cooling time ($\Delta t_{8/5}$) measured from Figure *4-5* is 3.12 seconds and the $\Delta t_{8/5}$ derived from Equation 4-3 is 2.96 second. This shows that the results are in a good agreement with the empirical estimate. $\Delta t_{8/5}$ can also measure from experimental thermocouple measurements, but these results were not available.

Table 4-7 Calculating t $_{8/5}$

| | |
|---|---|
| Arc voltage | 25,40 |
| Welding current | 85,00 |
| Welding speed | 13,62 |
| Sheet thickness | 17,00 |
| Preheating | 20:00 |
| Welding processes | Tungsten Inert Gas (TIG) |
| Type of weld | Root layer of V-seams |
| Calculated cooling time | $\Delta t_{8/5}$ = 2.96 s |

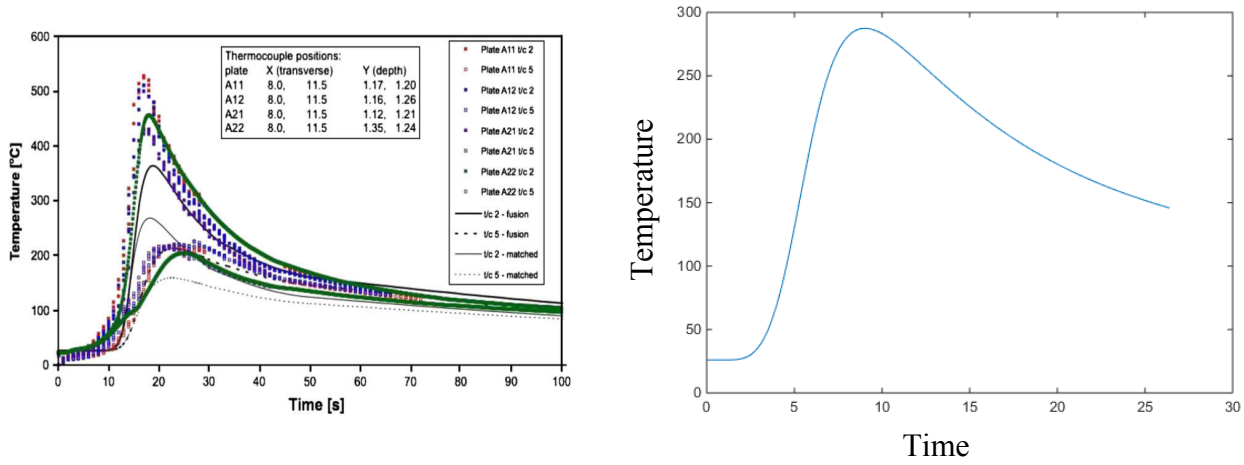


Figure 4-6 Predicted and measured transient temperatures at mid-length, top surfaces (HAZ)

### 4.6.2 Comparison of Fusion Zone and HAZ to experimental results

The second way to validate the model is to compare the cross section of the model and the weld macrograph. Figure *4-8* shows fusion boundaries derived from Round Robin studies. It depicts the temperature on a contour plot at a section perpendicular to the weld bead at the bead mid-length. It shows that in higher heat input the fusion boundary is matched with the result of cross section metallography image while in low heat input it doesn't match. Figure *4-8* shows the cross section of our model. The results are quite similar to the results derived from the round robin study. The temperature in the HAZ and FZ varies from 250 to 3000 ℃. The higher temperature seems a little high which needs more calibration.

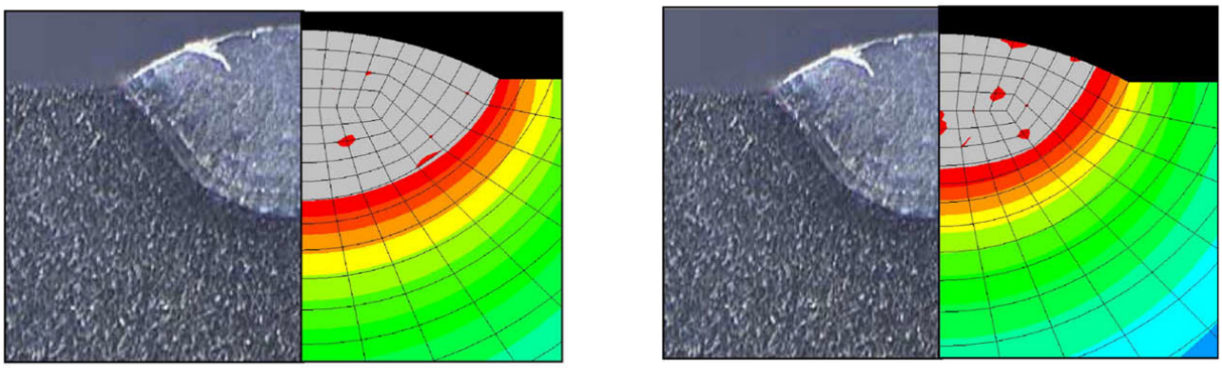

Figure 4-7 Predictions of extent of fusion boundary a. matched fusion boundary b. low heat input

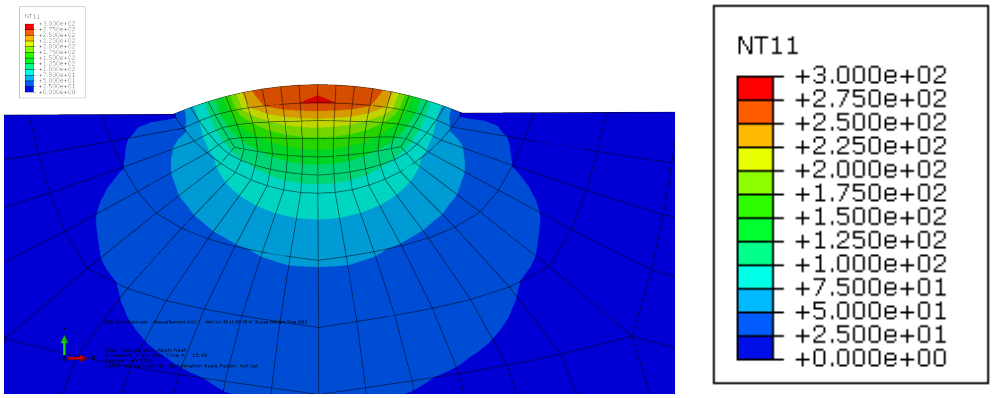


Figure 4-8 Fusion boundary of the model at the mid-length

## 4.7 Summary

In this section a thermal analysis was done according to a previously done round robin study to make sure that Abaqus is a validated simulation software for the thesis purpose. It provided good and acceptable results so the project is continued with the next phase which is the thermal analysis of the model provided by ESAB.

# 5 Thermal analysis of model provided by ESAB

## 5.1 Introduction

The base specimen is prepared form a plate of 500*150*15 mm dimensions, machined with a V-shape groove of 60˚C and 8 mm deep, welded with three passes. The dimensions and part of the experimental setup are presented in Figure 5-1 and Figure 5-2 . Chemical compositions of the base material and weld metal are listed in the appendix 3.

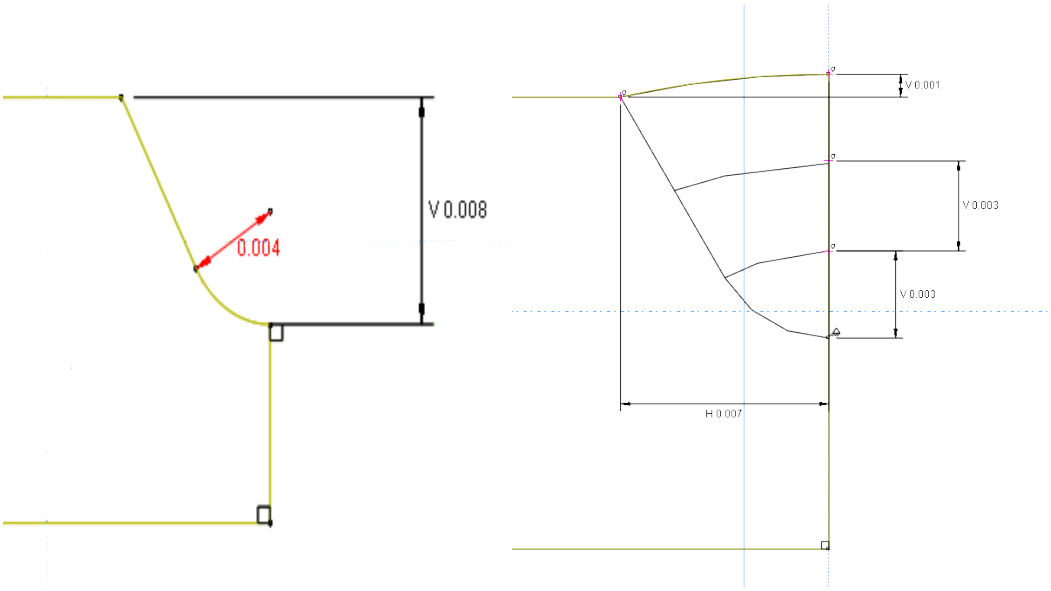


*Figure 5-1Cross-section of V-shape groove and multi passes*

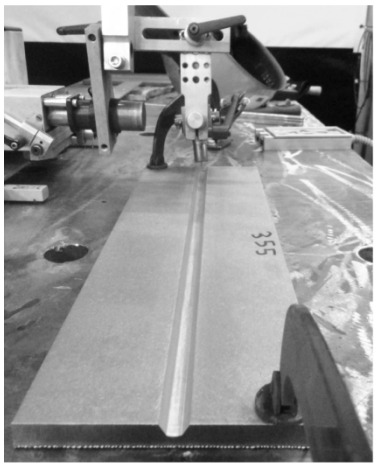


*Figure 5-2Ready set up for welding*

For the multi pass welding FE models, the geometry including all passes is usually defined initially. Therefore the 'not laid' weld is also included in the model at the beginning of analysis, which could decrease the accuracy of the model, if not properly treated. To imitate the gradual addition of filler metal during welding, one can do one of the following methods (L. E. Lindgren 2007)

- Add the whole weld material at the beginning, but define zero material properties for weld passes before they are laid. This method is called *Quiet Elements*.
- Add the weld beads corresponding to each pass in different steps by deactivating them at the beginning of the simulation and activating each part at the time of addition of the corresponding weld metal.

The second method is used within this analysis.

## 5.2 Simplifications and assumptions

Welding process comprises of several complex phenomena that occur at the same time, as discussed in Chapter 3. Therefore several simplifications are necessary to achieve a finite element model that is both "accurate enough" and "computationally fast enough". Most important assumptions and simplifications include:

- The analysis is done between three couplings of thermal, mechanical and metallurgical domains, but the weak couplings are neglected (Figure 1-1).
- In each weld pass, it is assumed that the whole weld bead is laid down at the same time (i.e. at the beginning of the welding step).
- Welding speed is assumed constant during each pass.
- The heat source is considered either cylindrical or double-ellipsoid with Gaussian power density distribution.
- Welding efficiency is one of the uncertainties because we had no data on this.

## 5.3 Weld pool

In this study, double ellipsoidal heat source is chosen due to the fact that it represents the shape and energy distribution in the molten pool in a way that is closer to the reality, compared to other available models. In double ellipsoid model, the heat gradient is different in the front and the rear side of the weld torch (steeper at the front and smoother at the rear).

The modelling was started with a simpler heat source, namely the cylindrical heat source model with uniform power density distribution within the cylinder. Later, the heat source is replaced by a double ellipsoidal one. There are some guidelines regarding the choice of heat source dimensions. Goldak and Akhlaghi (2005) recommend that the heat source sizes should be taken as 90% of the sizes of the molten pool. So from cross-sectional metallographic of the weld, the volume of the heat source is calculated and 90% of that amount is considered as the weld pool dimension.

## 5.4 Abaqus user subroutine DFLUX

The DFLUX subroutine provides the possibility to define a non-linear flux distribution as a function of time, temperature, coordinates, etc. in a heat transfer or mass diffusion analysis. DFLUX is used in this work to simulate a moving heat source with a non-uniform distributed flux. It is developed in FORTRAN language to describe a cylindrical and a double ellipsoid moving heat source for a three pass weld. In this subroutine, different variables should be defined as output, namely FLUX(1) and FLUX(2) which will be passed to the main program. FLUX(1) is a body heat power flux flowing into the model and FLUX(2) is (dq/dT), which is

the rate of change of the flux with respect to the temperature. Important input values that are passed from main Abaqus program to the subroutine, are TIME (2), that indicates the current value of total time, and COORDS which is an array containing the coordinates of the points of interest.

## 5.5 Material Properties

Material properties such as (temperature-dependent thermal conductivity, specific heat, latent heat, young's modulus, density, etc.) were collected from either from measurements at ESAB, or from numerical analysis by JMatPro. JMatPro is a material simulation software, which can calculate a wide range of alloy's properties including

- Mechanical properties,
- Physical and Thermo-physical properties
- Chemical properties
- Phase transformations and etc.

In order to use JMatPro and in addition to chemical composition of the alloy, austenite grain size, cooling rate and austenitization temperature are needed as input. Several studies have been conducted to evaluate the effect of grain size on residual stresses. Heinze et. al (2013) studied the effect of prior austenite's grain size on the welding-induced residual stress state in the heat affected zone for the structural steel S355J2+N. They concluded that the prior austenite's grain size has no significant influence on the residual stress state. The range of material properties for different alloys are shown in Figure *5-3*according to Goldak (J. A Goldak and Akhlaghi 2005). As it is clear in the Figure *5-3*, by increasing temperature, conductivity increases as well. It also shows that thermal conductivity of steels at room temperature depends on the alloy composition. By increasing the amount of alloy elements, thermal conductivity is reduced. Figure *5-3* Presents thermal conductivity graphs and specific heat capacity for the Weldox 700 steel (parent material) and LTT1 (weld metal) studied here. As mentioned before, heat conductivity at the temperature above the solidus is assumed to be three times the conductivity of solidus temperatures.

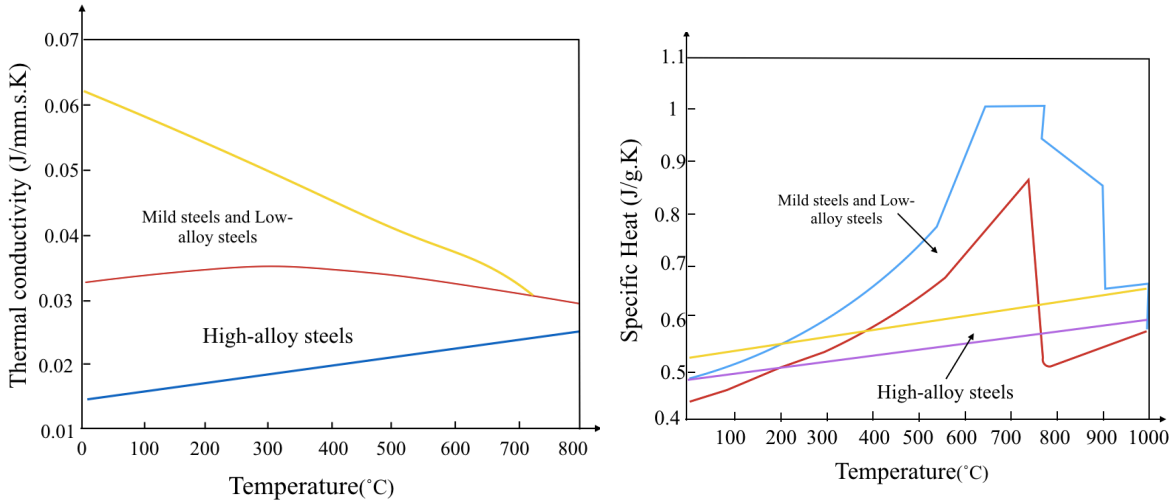


Figure 5-3 (a)Thermal conductivity of steels as function of temperature, (b) Specific heat of steels as function of temperature*(J. A Goldak and Akhlaghi 2005)(J. A Goldak and Akhlaghi 2005)*

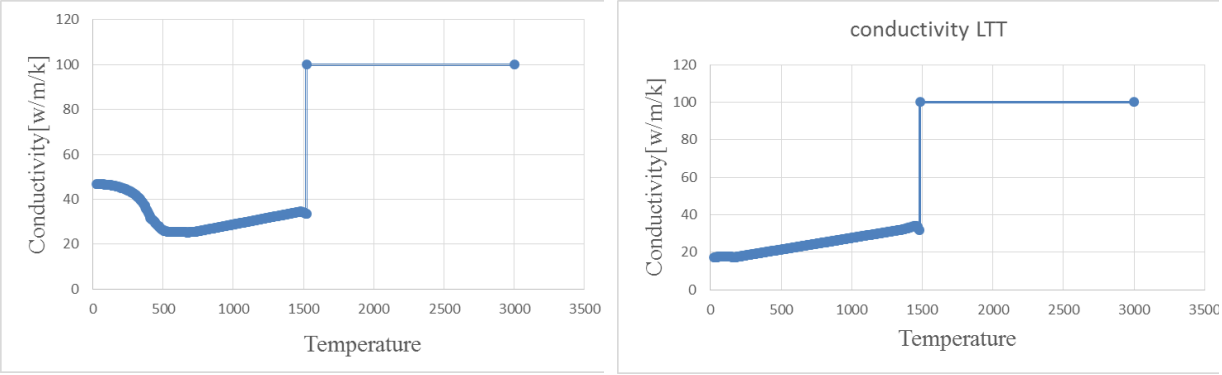


Figure 5-4 Thermal conductivity of (a) Weldox700 and (b) LTT1, derived from JMatPro

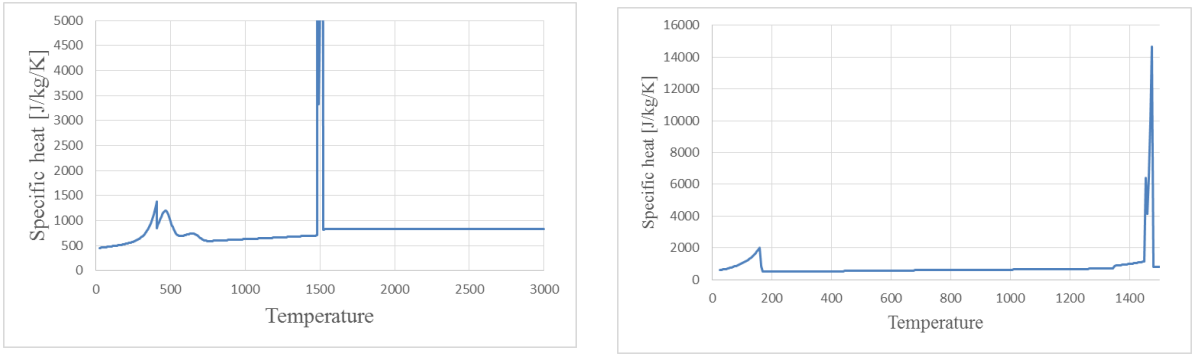


*Figure 5-5* Specific Heat of (a) Weldox700 and (b) LTT1, derived from JMatPro

Figure 5-5 shows that there is a peak over the range of temperatures from a lower (solidus) temperature to an upper (liquidus) temperature. This peak is related to the released latent heat. In order to avoid taking to account the latent heat twice, this peak is removed in the data of specific, instead the area under the peaks are calculated and added to the material properties in input file as the latent heat for both Weldox and LTT1.

## 5.6 Welding procedure

As can be seen in the appendix 1, the weld length is 500 mm. In order to simulate the three-pass welding, 8 analysis steps are defined. Initial step in which the whole weld passes are removed through model change, first pass (W1), cooling first pass of the weld (C1), second pass of the weld (W2), cooling the second pass (C2), third pass of the weld (W3), cooling the third pass (C3) and the final cooling to let the whole weld reach the ambient temperature. The welding and cooling times are calculated from the data from actual welding of the specimen: The measured welding speed for first, second, and third pass are 3, 4, and 5 mm/s, respectively. The inter-pass cooling times (C1, C2, and C3) are taken as 60 seconds Table *5-1*.

As discussed earlier, at the beginning of each pass, the whole corresponding weldment material is laid down by activating it through model change. The welding parameters including welding velocity in each weld's pass, start and end time in each step and duration of each step are listed in the Table *5-1*.

Table 5-1. Welding velocity, start time and end time for each step of welding simulation.

| Step | Velocity(mm/sec) | Duration(sec) | Start time | End time |
|---|---|---|---|---|
| initial | | 1 | 0 | 1 |
| W1 | 6 | 83.3 | 1 | 84.3 |
| C1 | | 60 | 84.3 | 144.3 |
| W2 | 5 | 100 | 144.3 | 244.3 |
| C2 | | 60 | 244.3 | 304.3 |
| W3 | 4 | 125 | 304.3 | 429.3 |
| C3 | | 60 | 429.3 | 489.3 |
| C final | | 900 | 489.3 | 1389.3 |

## 5.7 Generating geometry and mesh

The geometry is created in part section. In the first try the plate was drawn and different passes were added to the plate. In this way the geometry had several short edges which later led to ill-shape mesh. Therefore, in the next try the whole plate was drawn and multi passes were created by partitioning the plate. Another cell partition added in order to have a finer mesh in HAZ and its surrounded elements and larger mesh in the further elements. Then different sets and surfaces is defined in Part section, listed in Table 5-3. In order to reduce the analysis time the model is divided in to two symmetry halves. A symmetry plane is defined and zero film properties is assigned to it.

Linear hexahedral elements of type DC3D8 (8-node brick elements) with one temperature degree of freedom in each node, is used. In order to save the analysis time the mesh, further away from the heat source, is coarser than the FZ and HAZ-mesh. The global seed size of 8 mm is assigned first. Then according to Figure 5-7 seed sizes of 2, 1 and 2 mm is assigned respectively. In the next step the model is meshed part by part from the finer seed area to the

area with the coarser seeds. The total number of nodes is 15744 and total number of elements is 12789.

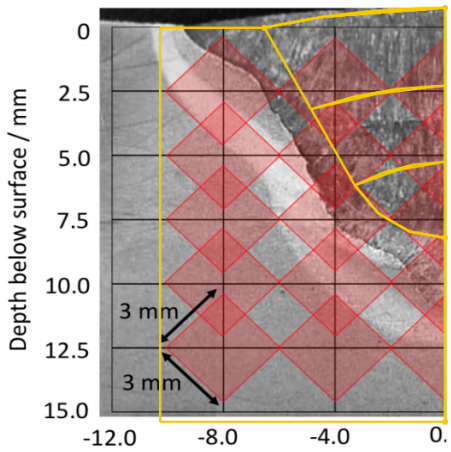


*Figure 5-6 Comparison of weld cross section in (a)Moded and (b) real*

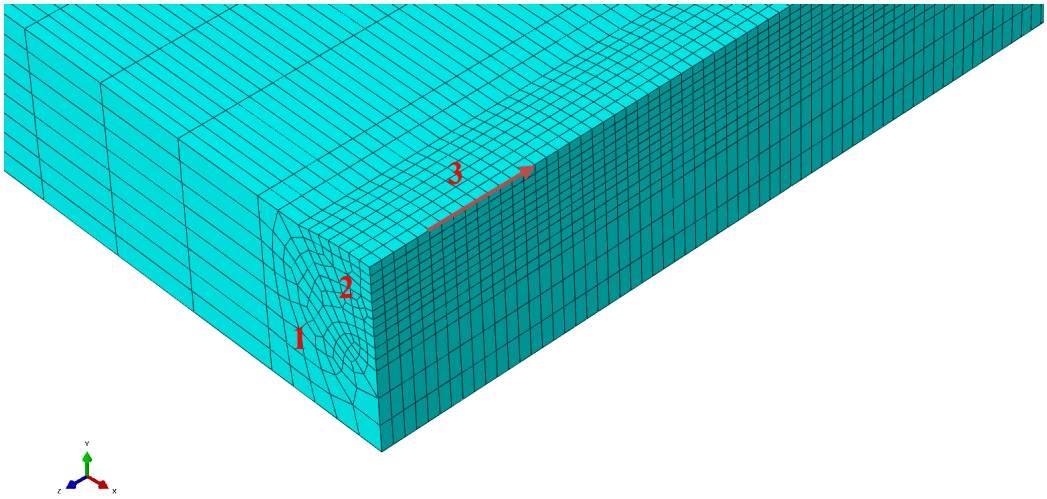


*Figure 5-7 Seeds and mesh*

*Table 5-2 Welding parameters*

| Parameter | Value | Unit |
|---|---|---|
| Welding type | GMAW | - |
| Weld speed | 3,4&5 | mm/s |
| Heat input model | Cylindrical /Double ellipsoid | — |
| Weld efficiency | 0.9 | — |
| Torch travel length | 0.5 | mm |
| Current | 26.2 | A |
| Voltage | 250 | V |
| Power | 250*26.2*ɳ | W |

*Table 5-3 Different sets and surfaces in the model*

| Name | Surface/Set | Application |
|---|---|---|
| AllWeld | Set | Model change/remove weld |
| Fieldoutput | Set | To limit the analysis |
| Halfplate | Set | Film properties |
| Pass1 | Set | Film properties |
| Pass2 | Set | Film properties |
| Pass3 | Set | Film properties |
| Pass1Surface | Surface | Film properties |
| Pass2surface | Surface | Film properties |
| Pass3surface | Surface | Film properties |
| Platesurface | Surface | Film properties |
| SymmetryPlane | Surface | Film properties |

## 5.8 Convergence

In order to put the analysis to converge, a proper time increment and element length are needed. Selecting the time increment can be automatic or optionally can be chosen manually by defining a fixed increment in the Step module. In the automatic time-stepping, minimum, maximum step size, and number of increments should be defined. Deltmx parameter is set to limit the maximum change of temperature allowed in each time step. For example in the step related to the first pass the initial time increment is set to 0.01, the max time increment is 0.015 and the minimum time increment is set to 0.0001. The total time which is the welding time for the first pass is 83.3 second and deltmx is set to 100. As can be seen in Figure *5-8*, two criteria can affect the time increment value (Acevedo, Drezet, and Nussbaumer 2013):

The convergence criterion: In this case the time increment is reduced until the convergence is reached. If the time increment reaches the minimum time increment without convergence the analysis will be stopped.
Deltmx: the time increment is reduced until there is convergence for a $\Delta T < \Delta T_{max.}$ (Figure *5-8*)

In order to reduce the analysis time and output file size, in the FIELD OUTPUT module, one can choose only the area of the interest e.g. in the current case, FZ and HAZ area are chosen by a frequency for reporting the results in the output file (e.g. each 10 step) instead of reporting analysis results for the whole model. An example of the command line of input file is as follows:

OUTPUT, HISTORY, FREQ=10

*NODE OUTPUT, NSET=HAZ+WELD

If the analysis does not converge even with the smallest prescribed time step, following actions can be considered:

- Revising the analysis tolerances (residual heat flux in each step),
- Reconsidering the element sizes in the mesh.

Regarding mesh revision, it is important to use fine mesh in the FZ and HAZ to have an accurate prediction of temperature and stress distribution. In order to find the optimum mesh size, it is divided or multiplied by a constant value and the model is resubmitted with the new mesh sizes. If the element dimensions are too large then the temperature doesn't move smoothly between elements in the weld direction, which is physically incorrect. These oscillations may lead in an uneven temperature distribution if temperature-dependent material properties are defined in the model. There is also a guideline on the relation of minimum usable time increment and the element size (Abaqus documentation). The time increment is defined as follow:

$$\Delta t > \frac{\rho C_p}{6K} \Delta l^2$$

Where Δt is the time increment, ρ is density, K is thermal conductivity and Δl is element length. The element length should be 75% of torch diameter.

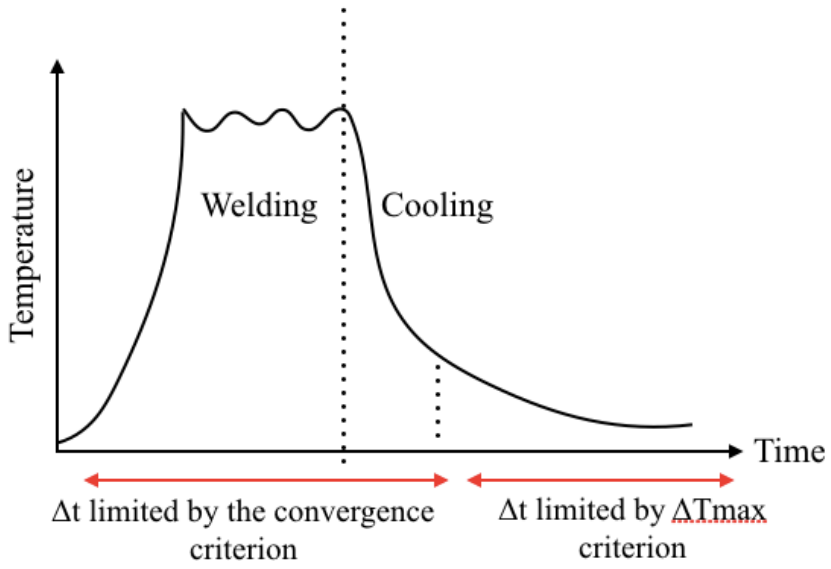


Figure 5-8 Time increments driven by the convergence criterion or by the ΔT max criterion.(Acevedo, Drezet, and Nussbaumer 2013)

## 5.9 Interaction

As discussed before, 8 steps are defined. In the beginning of each pass the geometry of the weld pass is activated through model change module which is done as an interaction in the model. Therefore, different sets are defined in the part section according to Table 5-3.

## 5.10 Boundary condition

Combined convection and radiation are applied by defining several surface sets for the surfaces in contact with air for each weld pass. Ambient temperature of 50˚C is also assumed in the predefined load manager.

## 5.11 Results (cylindrical heat source)

The complexity of the geometry and size of the model led to large modeling and analysis time. The analysis was completed after 120 hours running at Glenn cluster at Chalmers University. The next step will be validating its results.

### Model validation

#### 5.11.1 Temperature History

The temperature history of the model is plotted in the FZ at a node in the first pass of the weld *(*Figure 5-10*)*. The temperature increases as the torch bypasses the point of observation. In the left diagram, it is clear that the temperature increases up to 1900˚C, 1700˚C and 450˚C in the first, second and third passes respectively. The temperature declines as the torch moves on but it does not get to the room temperature until final cooling. In the right diagram, the location of the node under consideration is shown.

*Table 5-4. Calculation of T8/5 for the model with the properties provided by ESAB.*

| | |
|---|---|
| Arc voltage | 26.20 |
| Welding current | 250.00 |
| Welding speed (1st, 2nd and 3rd pass) | 36.00, 30.00, 24.00 (cm/min) |
| Sheet thickness | 15.00 |
| Preheating | 50.00 |
| Welding processes | Tungsten Inert Gas (TIG) |
| Type of weld | Root layer of V-seams |
| Calculated cooling time | $t_{8/5}$ = 3.61 s , 3.57s and 5.00 |

*Table 5-4*shows the theoretical $t_{8/5}$ for each pass of the weld. Calculated $t_{8/5}$ from the Figure 5-10for the first and second pass is 1.08 and 2.32 second respectively. The calculated results have a difference of almost 60 % from theory, however it should be considered that the theoretical formula are also has some assumptions which made the less accurate. Moreover, the cooling rate is still quite high which means the final microstructure could be martensite. Figure 5-11 *and* Figure 5-12 depicts Temp-time diagrams at different nodes with different distance from the torch location. *Figure 5-13* shows the cross section of the weld for each pass of the weld.

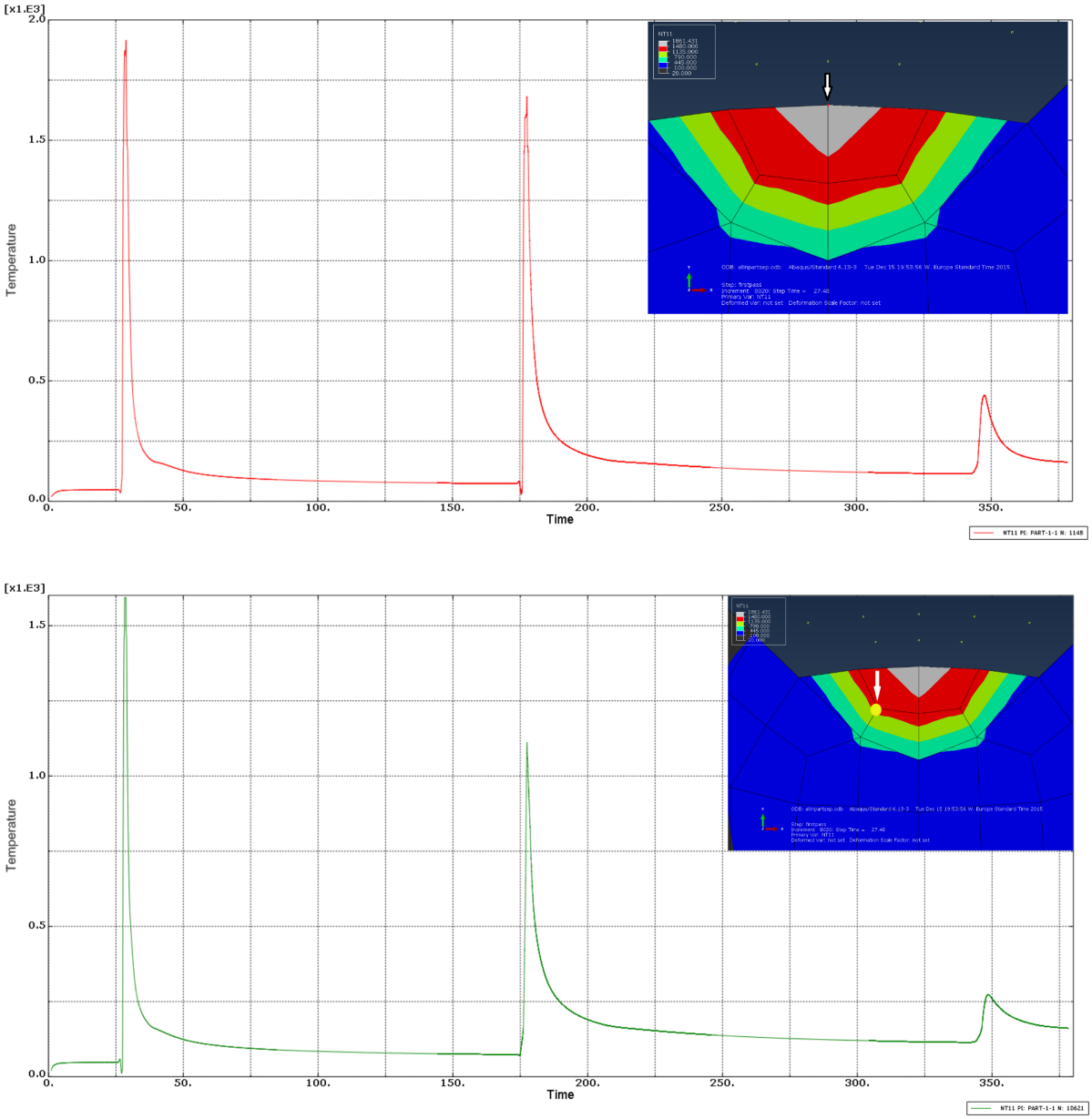


*Figure 5-9 Temperature-Time graphs for all three passes in two different nodes at the first pass, shown in the image*

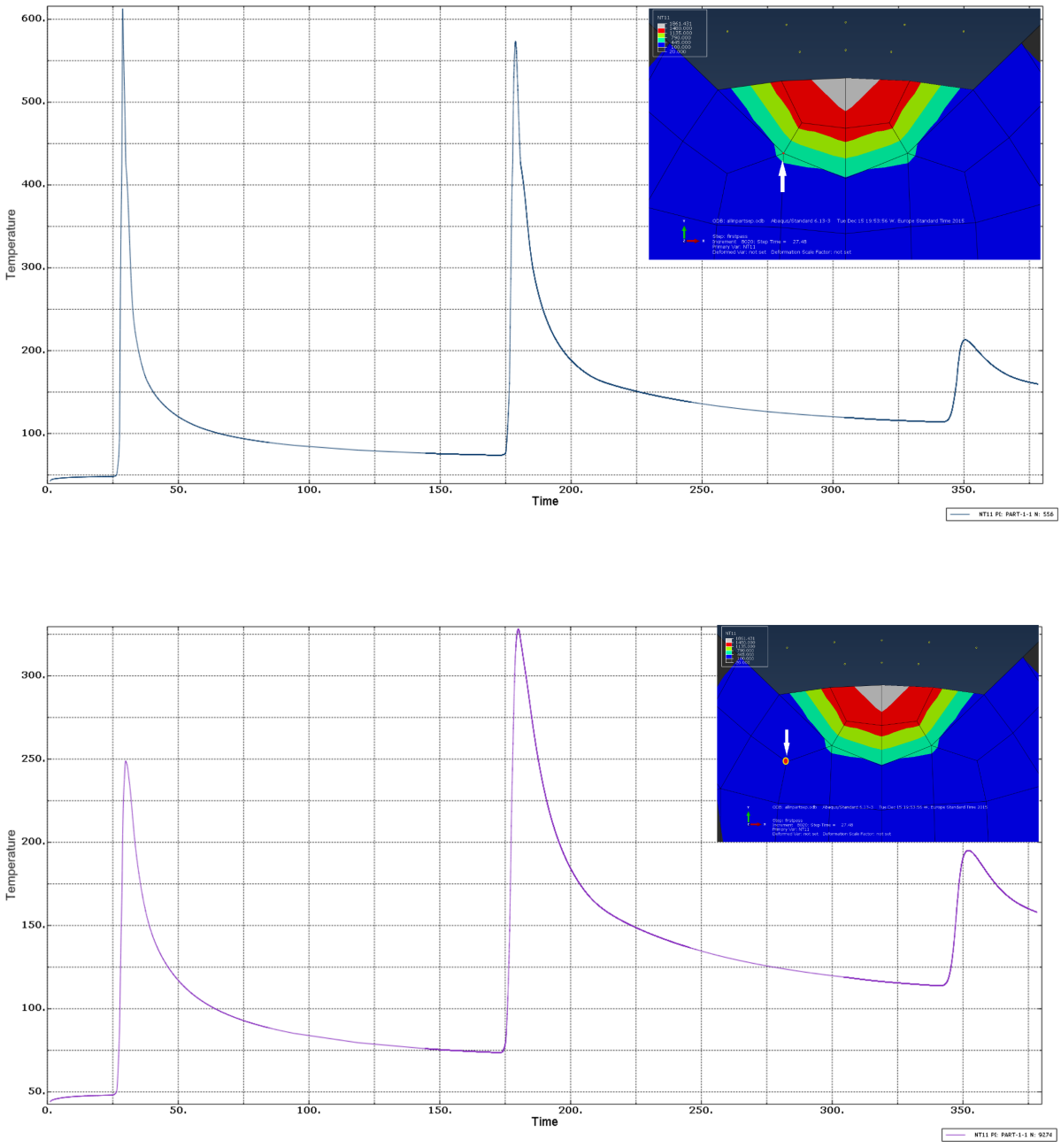


*Figure 5-10 Temperature-Time graphs for all three passes in two different nodes in the base material, shown in the image*

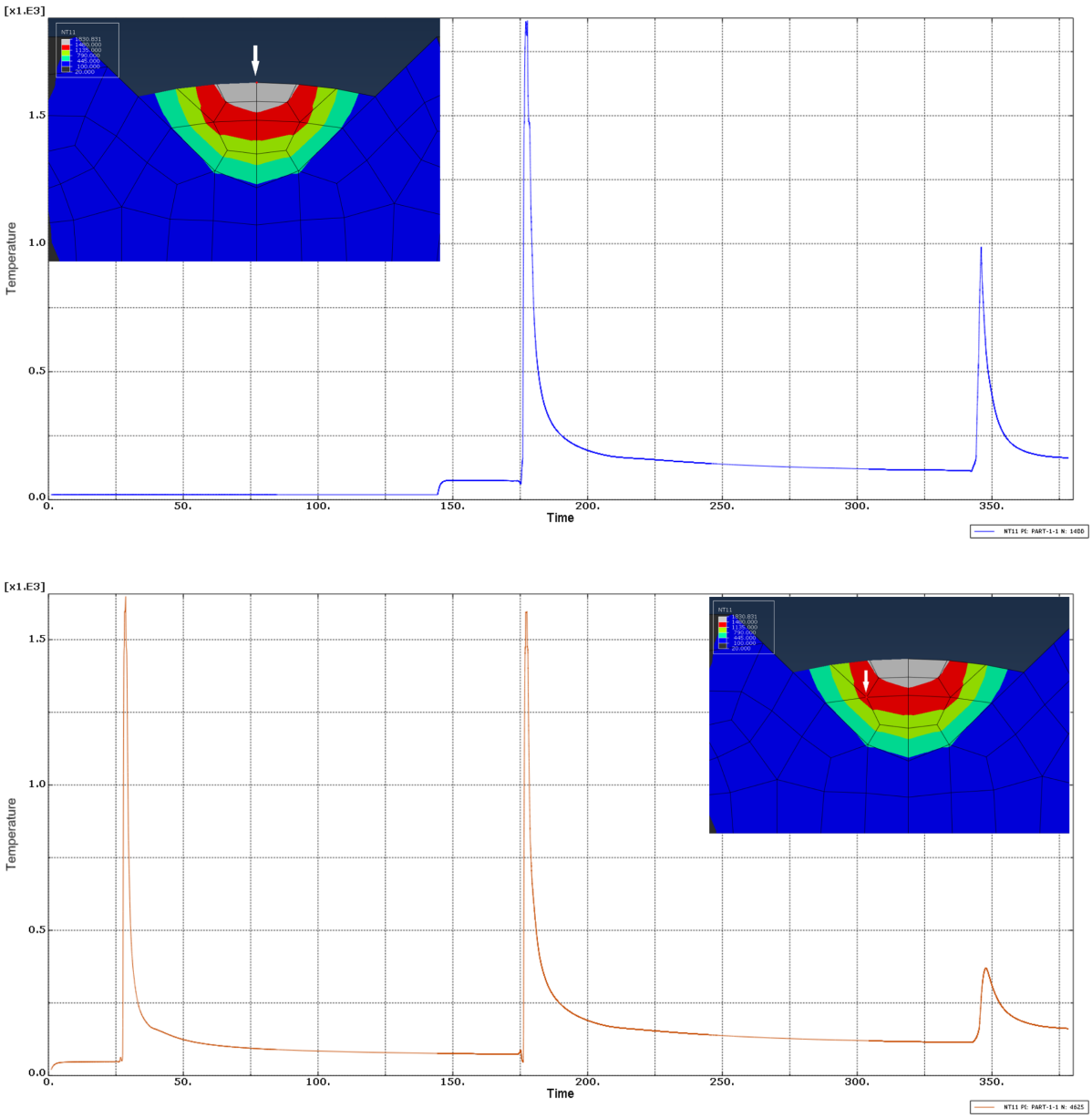


*Figure 5-11 Temperature-Time for all three passes in two different nodes at the second pass, shown in the image*

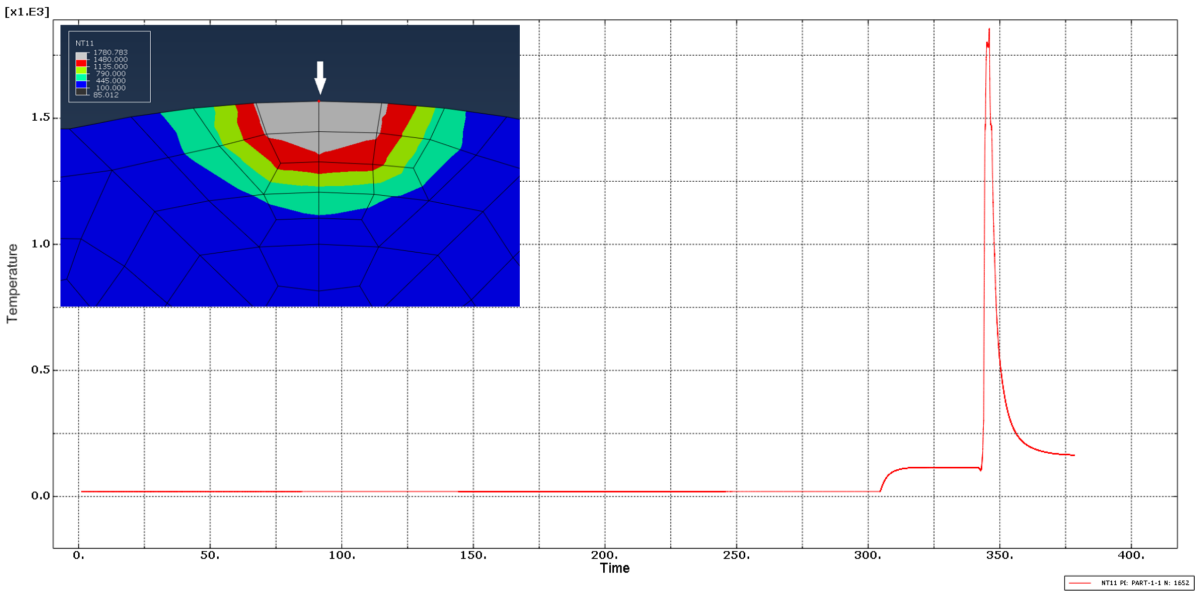


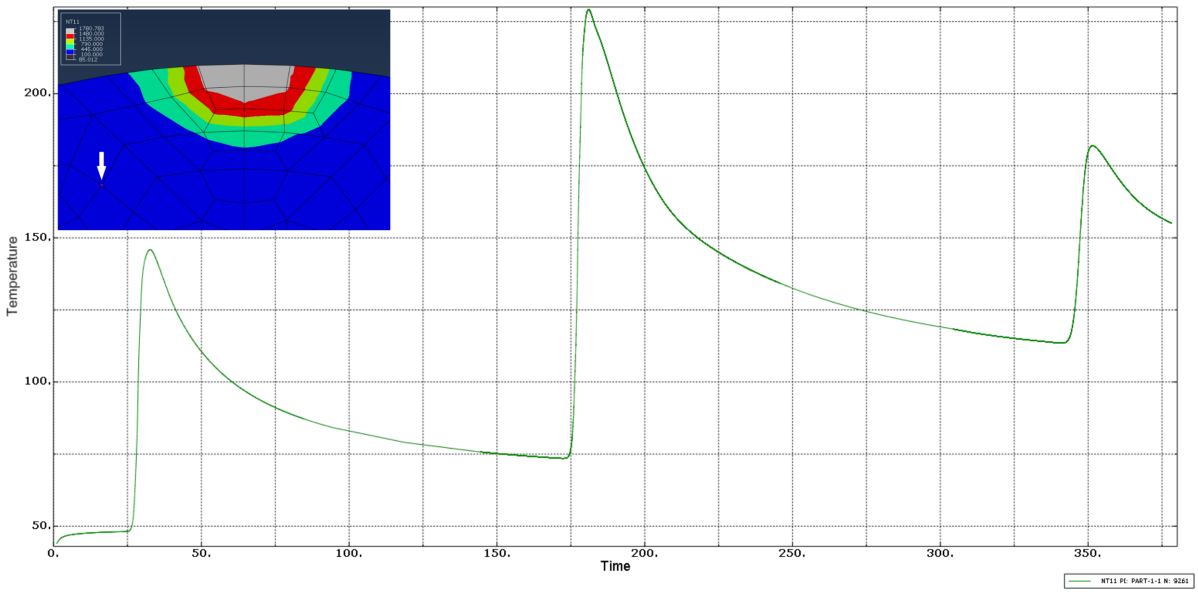


*Figure 5-12 Temperature-Time graphs for for all three passes in two different nodes at the second pass, shown in the image*

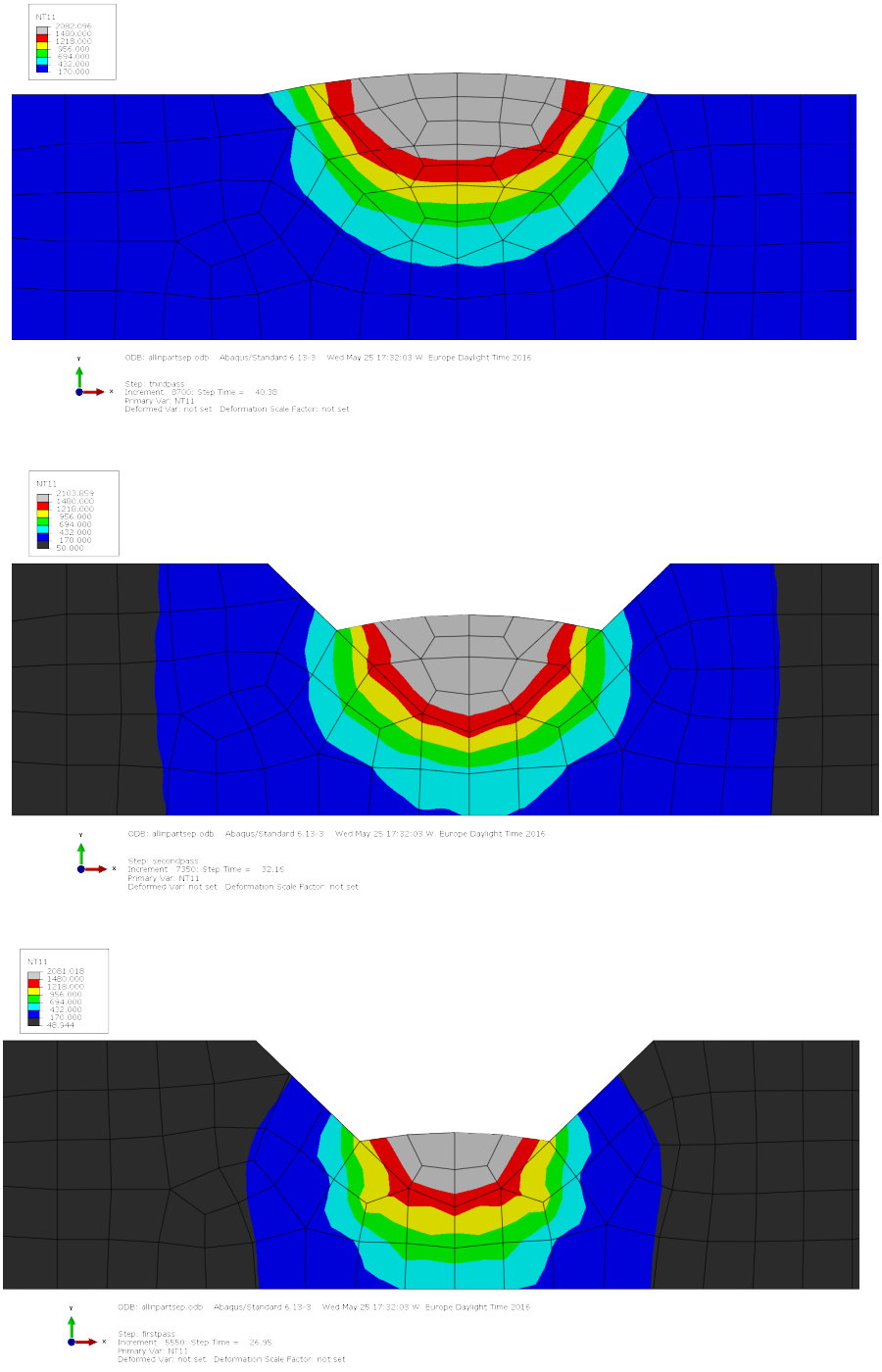


Figure 5-13 the cross section of ESAB model a. first pass, b. second pass and c. third pass

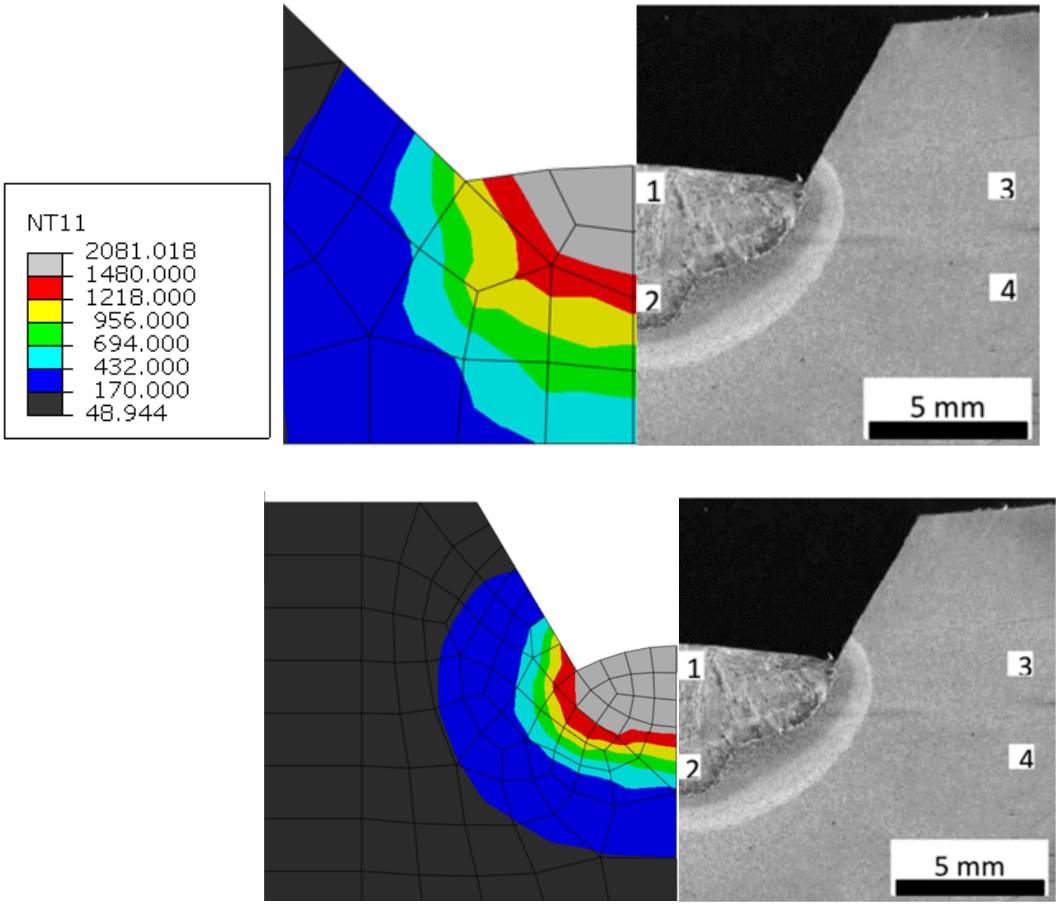


Figure 5-14 HAZ geometry, experimental and simulated for two different model with different mesh size

## 5.12 Results (Double-ellipsoid heat source)

After validating the model with the cylindrical heat source the next step is repeating the analysis using a double-ellipsoid heat source. The DFLUX subroutine is reformulated in FORTRAN language for the three pass weld. In this case the problem is how to estimate the double-ellipsoid parameters. There are some theoretical formulas to calculate these parameters.

### 5.12.1 Goldak Double Ellipsoid Heat Source Model parameters

It is important to estimate the parameters of Goldak heat source model since it will affect the temperature field and consequently the residual stresses. Christen has described different solution to calculate the double ellipsoid heat source dimensions based on Rosenthal equation (Christensen, Davies, and Gjermundsen 1965). The Rosenthal model has some limitations due to the fact that he assumed a point source in an infinite slab. The temperature distribution according to Rosenthal is as follow:

$$dT_{t'} = \frac{\exp\left(-\frac{R^2}{4\pi a(t-t')}\right)}{\rho c(4\pi a(t-t'))^{3/2}}\delta Q dt'$$

Where (a) is diffusivity, δQ is the heat source, (x', y', z') is the heat source coordinate at the t'=0. $R^2$ is the distance from the heat source $((x-x')^2-(y-y')^2-(z-z')^2)$.

In order to eliminate the Rosenthal equation limitations Christen defined his solutions in a dimensionless form. New dimensionless coordinates are as follow:

$\xi = \frac{\upsilon x}{2a}$ Dimensionless x-coordinate

$\Psi = \frac{\upsilon y}{2a}$ Dimensionless y-coordinate

$\zeta = \frac{\upsilon z}{2a}$ Dimensionless z-coordinate

Dimensionless time and temperature are defined as follow

$$\theta = \frac{(T - T_0)}{(T_c - T_0)}$$

$$\tau_i = \frac{t}{t_i}$$

Where $T_c$ is a chosen temperature e.g. melting temperature and $t_i$ is the arc ignition time.

Dimensionless operating parameter is defined as follow:

$$n_3 = \frac{q_0 \upsilon}{4\pi a^2 (H_c - H_0)}$$

$$a = \frac{\lambda}{\rho c}$$

Where a is diffusivity, λ is conductivity, ρ is the material density, c is specific heat capacity, $(H_c - H_0)$ is heat content per unit volume at the reference temperature and $q_0$ is the net arc power.

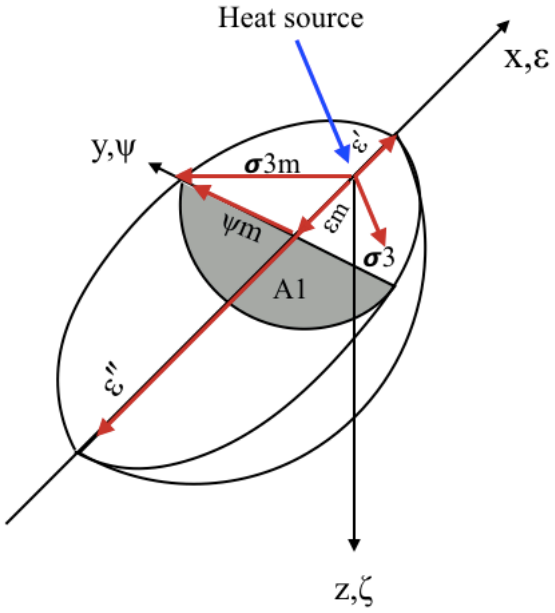


Figure 5-15 Dimensionless *parameters of Rosenthal solution (Grong 1997).*

In order to calculate the double-ellipsoid parameters, the isothermal contour can be calculated for the fusion zone. The isothermal length and width are calculated as follows according to Grong.

$$\Psi = \zeta_m = \sqrt{(\sigma_{3m})^2 - (\xi_m)^2} = \frac{\sigma_{3m}}{(\sigma_{3m}+1)}\sqrt{1+2\sigma_{3m}}$$ Isothermal width

Where $\sigma_3$ is dimensionless vector

$$\sigma_3 = \frac{vR}{2a}$$ Dimensionless vector

$$\xi' = \frac{1}{2}\ln\left(\frac{n_3/\theta}{\xi'}\right)$$ Distance from front of the ellipsoid

$$\xi'' = -n_3/\theta$$ Distance from rear of the ellipsoid

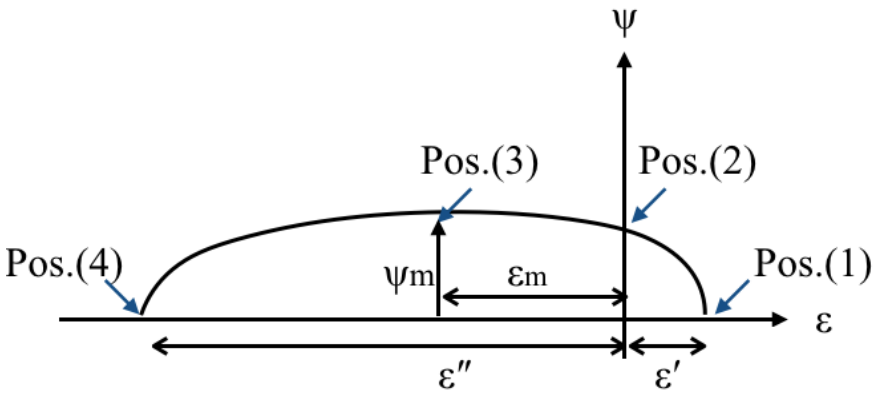


Figure 5-16 Double-ellipsoid parameters (Grong1977)

A more accurate solution for double-ellipsoid heat source is proposed recently by Fachinotti et al(Fachinotti, Anca, and Cardona 2011). According to Fachinotty the temperature field is defined as follows:

$$T(x,y,z,t) = T_0 + \frac{3\sqrt{3}Q}{\rho c \pi\sqrt{\pi}}\int_0^1 \frac{\exp\left(-\frac{3y^2}{12k(t-t')+b^2}-\frac{3z^2}{12k(t-t')+c^2}\right)}{\sqrt{12k(t-t')+b^2}\sqrt{12k(t-t')+c^2}} \times [f_f A_f(1-B_f) + f_r A_r(1-B_r)]\,dt'$$

Where

$$A_i = \frac{\exp\left(-\frac{3(x-vt')}{12k(t-t')+a_i^2}\right)}{\sqrt{12k(t-t')+a_i^2}}$$

$$B_i = \operatorname{erf}\left(\frac{a_i}{2}\frac{x-vt'}{\sqrt{k(t-t')}\sqrt{12k(t-t')+a_i^2}}\right)$$

Where T is the temperature at the position (x, y, z) and t is the time, k is the thermal conductivity and $T_0$ is the initial temperature.

In the present report the double ellipsoid parameters were calculated according to Christen formulas. A Matlab code were written (Appendix 4) and Material properties were used to estimate the double ellipsoid dimensions.

Table 5-5. Double ellipsoid parameters

| $C_f$ (m) | $C_r$ (m) | **Width** (m) | **Depth** (m) |
|---|---|---|---|
| 0.0109 | 0.0160 | 0.0046 | 0.0046 |

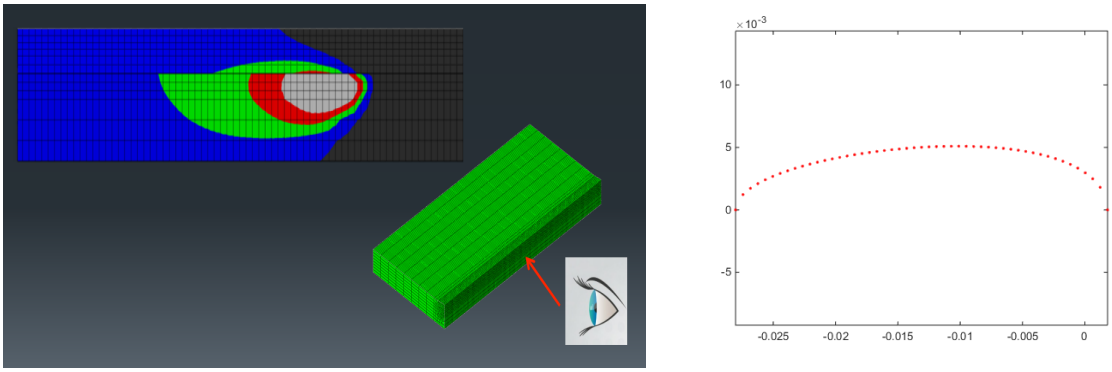


Figure 5-17. Calculated double-ellipsoid with Matlab

The analysis is run in the cluster but did not converge so it was decided to do a convergence study and a sensitivity study.

### 5.12.2 Sensitivity study

There are some factors such as material properties, heat source dimensions and film properties that can affect the thermal analysis. To study these parameters several analysis were done to compare the effect of these parameters on the final results. In order to follow the effect of specific heat and latent heat, several analysis were done with and without latent heat / specific heat to optimize theses parameters. Finally the peak of specific heat (Figure 5-5) in the range of solidus and liquidus was removed and the area under those peak were calculated and assumed as the latent heat (Figure 5-18)

Figure 5-19 shows the temperature history of the model with double ellipsoid heat source for the first pass. Only half of the first pass was calculated due the problem in converging the model with Goldak heat source. Therefore, very small time-increments are used. As a result, the analysis time became too long and the results file (odb, file) became too big. Since both time and memory exceeded the limitation I had

it was decided to use the cylindrical heat source instead and accept the lower accuracy to achieve a cheaper analysis.

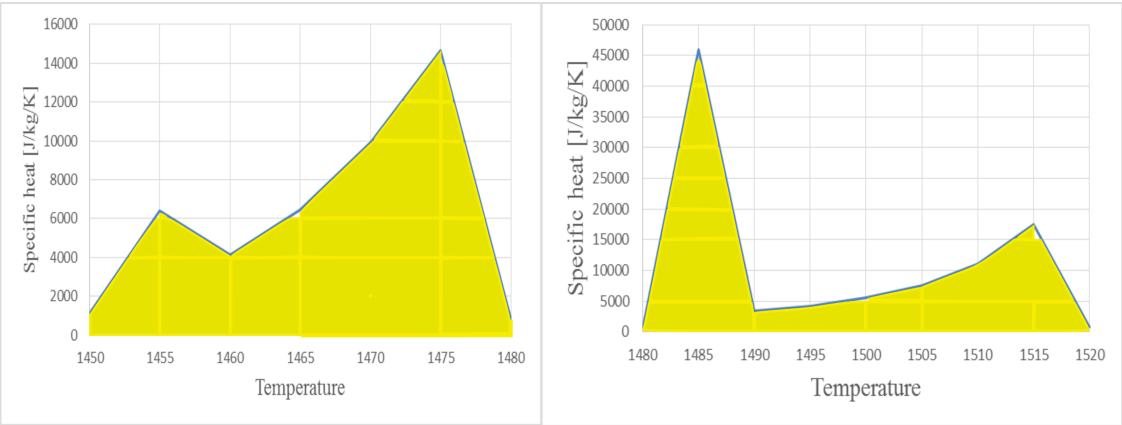


*Figure 5-18calculating latent heat by calculating the area under the specific heat-temperature graphs for LTT1 (a) and Weldox700 (b)*

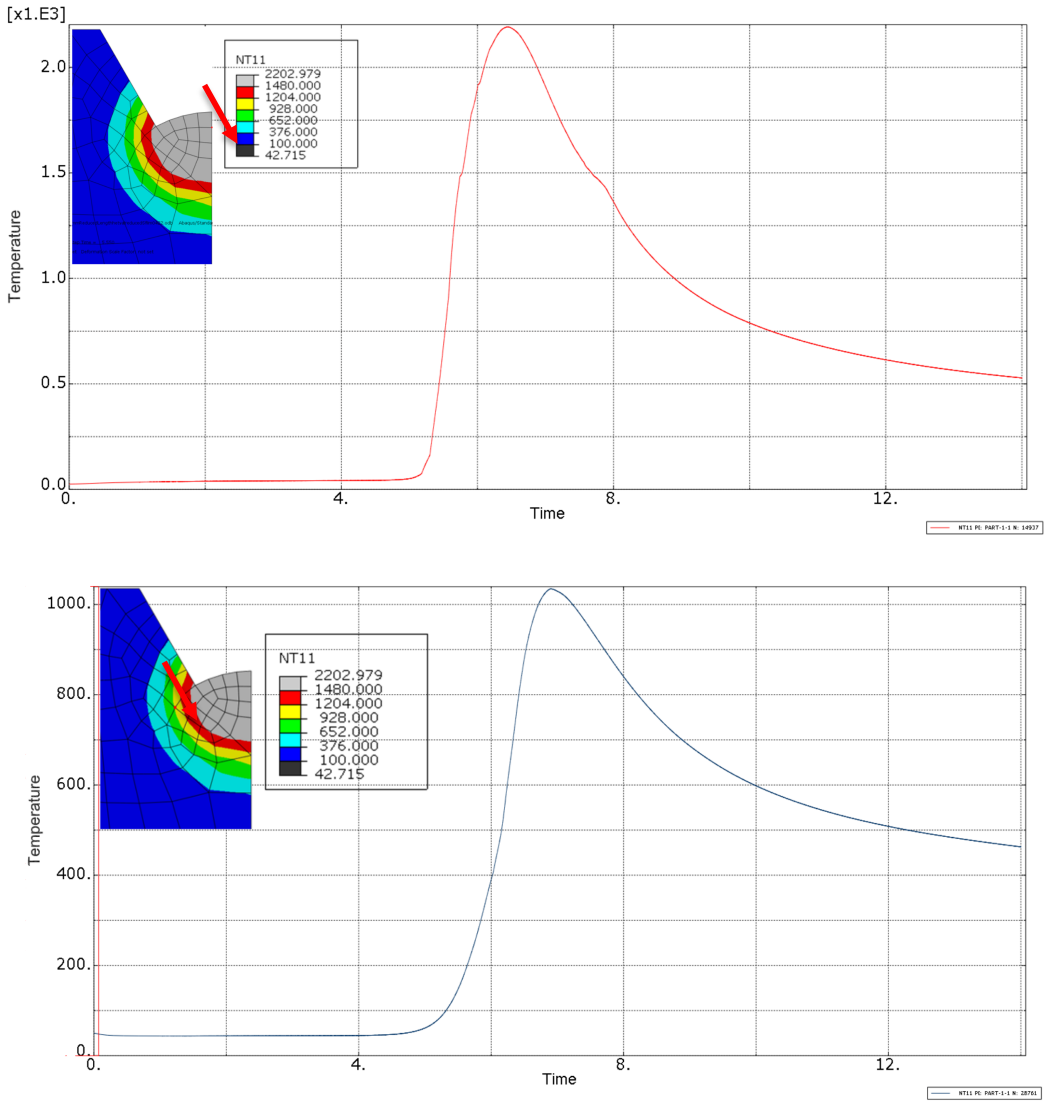


*Figure 5-19 Time-Temperature results for the analysis with Double ellipsoid heat source at FZ and HAZ*

In order to follow the effect of film properties two analysis were done one with film properties (combined convection and radiation) and the other one by assigning zero film properties.

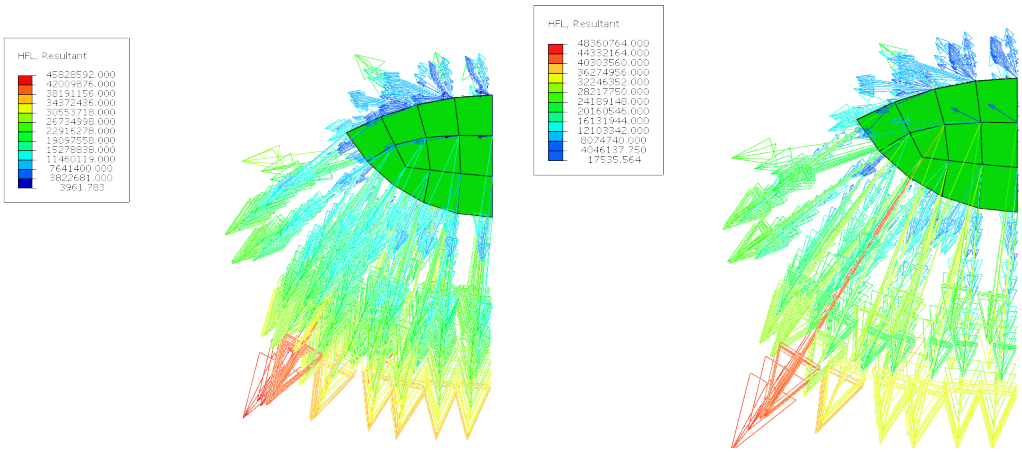


*Figure 5-20 Heat flux in a model with film properties (a) a model without film properties (b)*

### 5.12.3 Convergence study

In order to do a convergence study to different mesh is analyzed to see the effect of the mesh size. The model with finer mesh comprises of 188620 nodes and 175077 linear hexahedral elements of type DC3D8 and the model with larger mesh consists of 36252 nodes and 31450 linear hexahedral elements of type DC3D8 (Figure 5-21). Figure 5-22 compared the results for both model with the finer mesh and larger mesh size. The results are similar but the higher temperature for the model with finer mesh is less than the other model. Furthermore, by decreasing the mesh size the analysis time increased. In fact the analysis with the finer mesh worked without any convergence problems but the time consuming computation and large output files are a big concern.

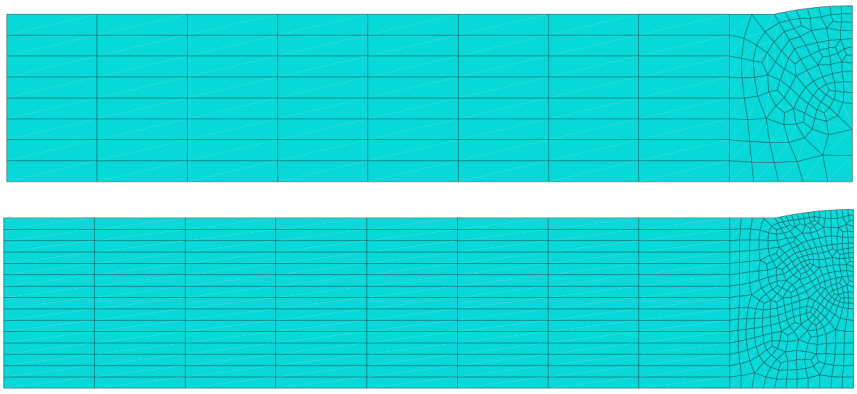

*Figure 5-21 Different mesh size*

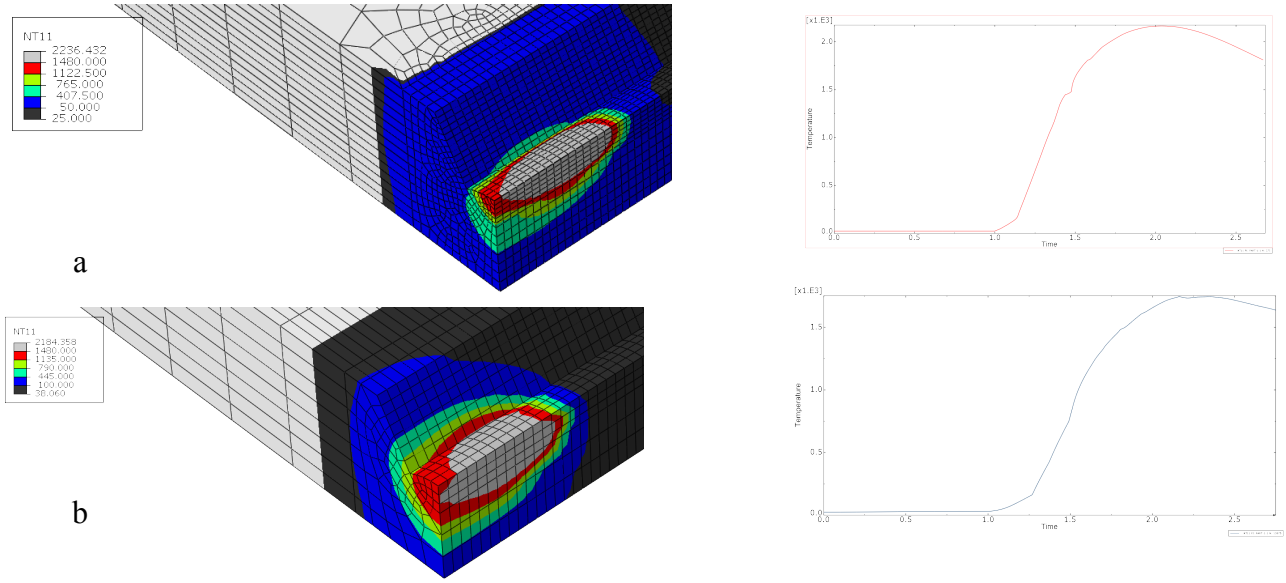


*Figure 5-22 Temperature-Time diagram for the model with finer mesh (a) and coarser mesh (b)*

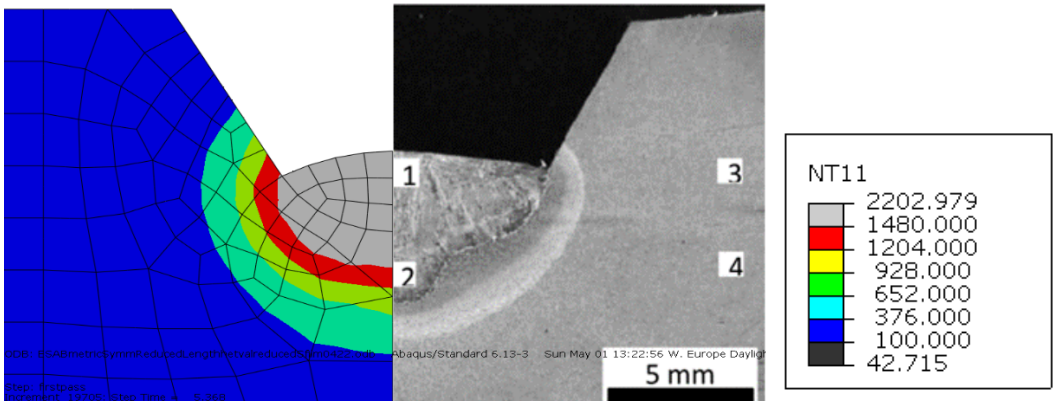


*Figure 5-23 HAZ geometry, experimental and simulated*

Figure 5-23 shows the comparison of HAZ and FZ for the experimental and simulated results. It shows that the geometries are more accurate compared to the results from the other analysis with the cylindrical heat source. The shape of the HAZ and FZ are more similar to the experimental results. The grey part in the left image shows the melted zone which is similar to the right image as in the both images some parts of the base material was melted. The red and green zones are related to HAZ, which are comparable to the light grey zone in the right image. In addition, the temperature range seems more accurate than the previous analysis.

# 6 Phase transformation analysis

In this work a metallurgical analysis is performed on the model provided by ESAB to simulate the phase transformations during welding. The user subroutine Hetval is used to model phase transformation. It is written as a FORTRAN code. Hetval shows the effect of internal heat generation on state variables (such as the fraction of material transformed) that themselves evolve with the solution and are stored as Solution-Dependent state Variables (SDV). To do so first different SDVs were defined in the input file as initial conditions separately for the base material (WELDOX700) and the filler material (LTT1). SDVs 1 to 6 are defined for Phase volume fractions of Austenite, Ferrite-Pearlite, Logic Active, Liquid, Bainite, Martensite and temperature for the base material and weld's passes as follow:

*HEAT GENERATION
*DEPVAR
7
*INITIAL CONDITIONS, TYPE=FIELD, VARIABLE=1
Pass1Geometry, "Initial volume fraction of Austenite"

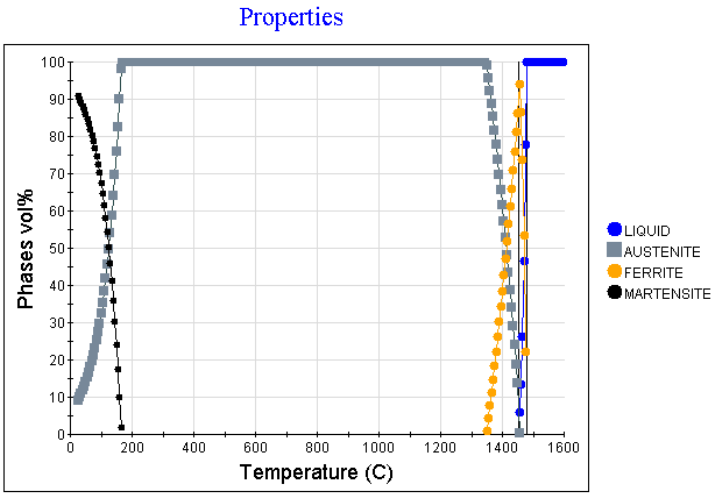


*Figure 6-1 Phase-Temperature diagram of LTT1 derived from JMatPro*

Then the Hetval code is written in the follow scope:

SUBROUTINE HETVAL (CMNAME, TEMP, TIME, DTIME, STATEV, FLUX, PREDEF, DPRED)
INCLUDE 'ABA_PARAM.INC'
CHARACTER*80 CMNAME
DIMENSION TEMP(2),STATEV(*),PREDEF(*),TIME(2),FLUX(2), DPRED(*)
user coding to define FLUX and update STATEV
RETURN
END

It is defined in Hetval which phases exist at different temperatures during heating and cooling by using the data from phase transformation diagrams derived from JMatPro (Figure 6-1) . Logic Active used is considered as zero for the temperature less than $A_1$ and one for the higher temperatures. When the base material is heated above $A_1$, Ferrite/Pearlite ($SDV_2$) partially transforms to Austenite ($SDV_1$). For the filler in a same way Martensite transforms partially to Austenite between $A_1$ and $A_3$. For temperatures above $A_3$ until the melting temperature $SDV_1$ (Austenite) is equal to one and other phases are equal to zero. $A_1$ and $A_3$ temperatures can be calculated according to the following equations (Deng and Murakawa 2013):

$$A_1 = 723 - 10.7Mn - 16.9Ni + 29Si + 16.9Cr + 290As + 6.4W$$

$$A_3 = 912 - 203\sqrt{C} - 15.2Ni + 44.7Si + 104V + 31.5Mo + 13.1W - 30Mn - 11Cr - 20Cu + 700P + 400Al + 120As + 400Ti$$

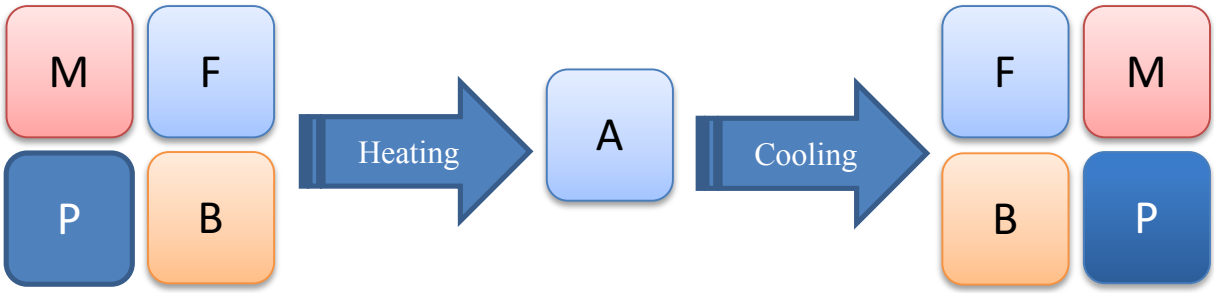


*Figure 6-2 Transformation of phases*

Figure 6-3 shows a schematic of the phase transformation analysis. phase transformation results a, b and c for phase fraction of Austenite, Liquid and other phases respectively gives as a result the range of SDV in the interval from zero to one. Fig 6-3 shows an example. The first image is related to austenite, the second one is for liquid and the third one is for other phases. Figure 6-4a shows the assumed initial conditions for the plate, martensitic filler material and ferritic-pearlitic base material, and image b shows that at the weld pool there is only liquid phase and apart of the base material transformed to other phases.

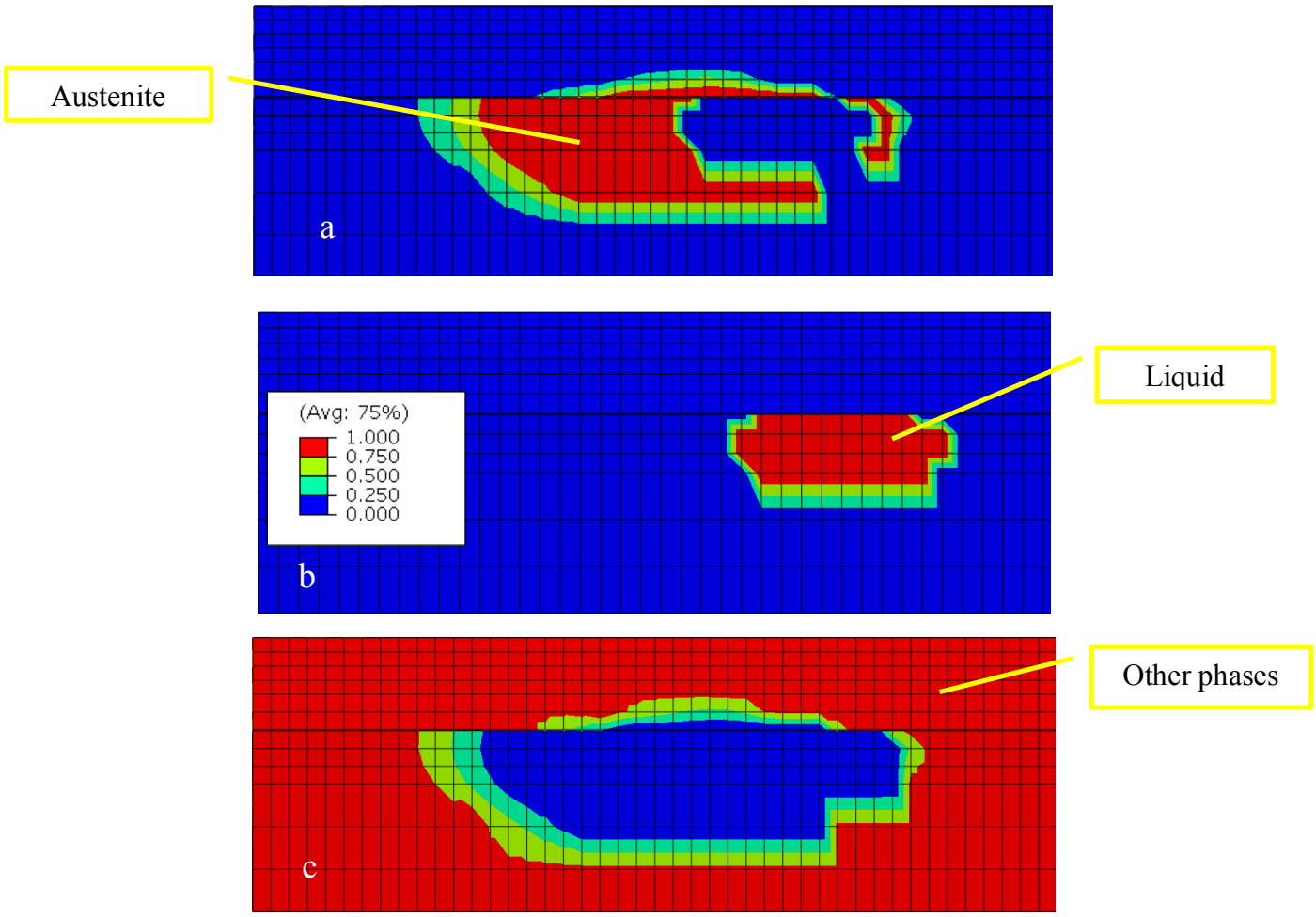


*Figure 6-3 phase transformation results a, b and c for phase fraction of Austenite, Liquid and other phases respectively*

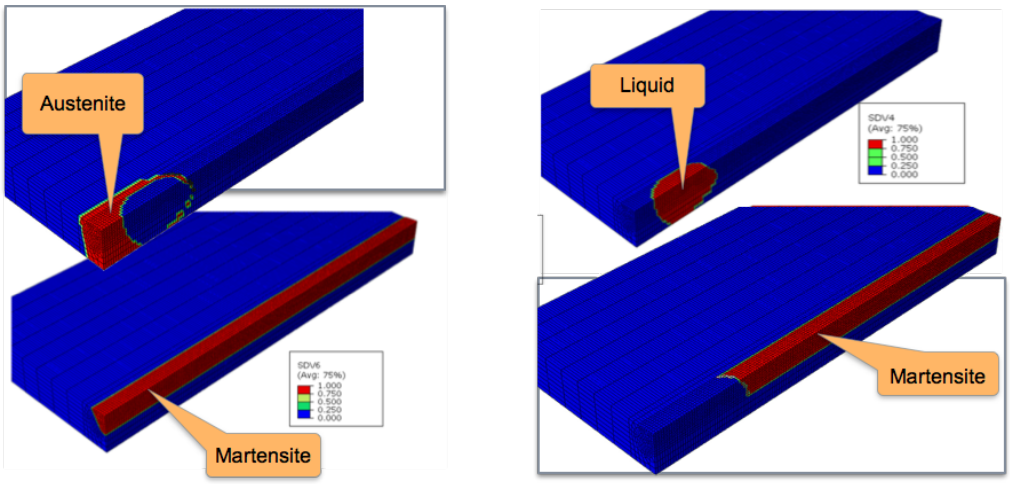


*Figure 6-4 Phase fraction. during welding*

# 7 Mechanical Analysis

A sequentially coupled thermal-mechanical analysis approach is used in this work. A sequentially coupled heat transfer analysis is used when the stress/deformation field in a component depends on the temperature field in that structure, but the temperature field can be found without knowledge of the stress/deformation response. This is usually done by first conducting a thermal analysis and saving the nodal temperatures as a function of time in a ".fil" file by requesting it in the input file as an output file as follows:

*NODE FILE, NSET=AllNodes, FREQUENCY=1
NT

*EL FILE, ELSET=weld3pass, FREQUENCY=1
SDV

Then the heat transfer analysis results transferred to stress analysis as a predefined field. *Temperature, file=Location of .fil-file/ Name of .fil-file without ".fil". The element type in the mechanical analysis should be changed to Stress/displacement elements, for example C3D8 (8-node linear brick).Then static steps should be defined in the input file instead of heat transfer step in the thermal analysis with the same increments.

## 7.1 Appropriate boundary conditions

The following boundary condition is used in the mechanical part of the simulation.

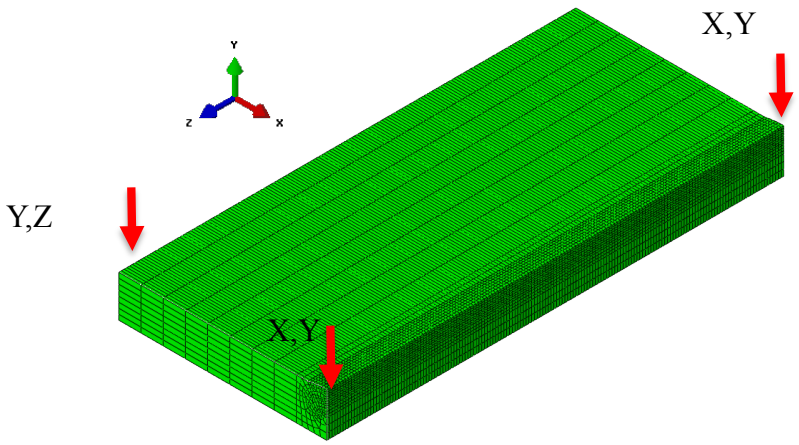


*Figure 7-1 mechanical boundary conditions*

## 7.2 Material properties needed for mechanical analysis:

### 7.2.1 Elastic

To specify elastic material properties, temperature dependent data for Young's modulus and Poisson's ratio are used. Dependencies parameter is set equal to the number of field variable dependencies included in the definition of the properties. If this parameter is omitted, it is assumed that the moduli are constant or depends only on temperature.

### 7.2.2 Thermal Expansion

Thermal Expansion is defined by temperature dependent data of thermal expansion coefficients and it can be isotropic, orthotropic, or fully anisotropic. Abaqus uses thermal expansion coefficient to compute thermal strain. The total thermal expansion is calculated from a reference temperature, $\theta^0$ (Figure 7-2).

Thermal strains are generated according to the formula:
$\xi^{th} = \alpha(\theta, f_\beta)(\theta - \theta^0) - \alpha(\theta^I, f_\beta^I)(\theta^I - \theta^0)$

$\alpha(\theta, f_\beta)$: Thermal expansion coefficient
θ: Current temperature
$\theta^I$: Initial temperature
$f_\beta$: Current values of the predefined field variables
$f_\beta^I$: Initial values of the field variables
$\theta^0$: Reference temperature for the thermal expansion coefficient.
If the coefficient of thermal expansion, α, is not a function of temperature or field variables, the value of the reference temperature,$\theta^0$ is not needed otherwise

So in the input file zero is set equal to 25 as follow:

*Expansion, zero=25.0, Dependencies=3

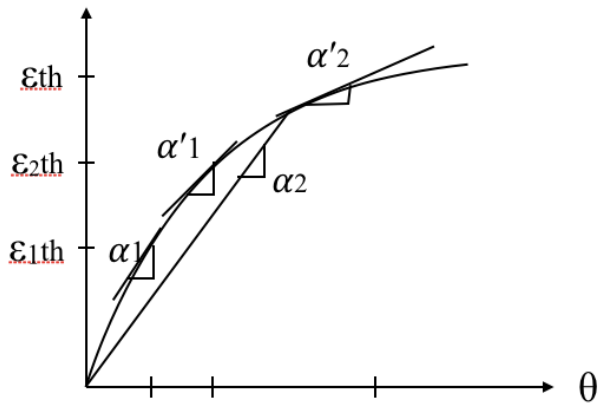


*Figure 7-2 Definition of the thermal expansion coefficient.*

### 7.2.3 Plastic

This option is used to specify the plastic part of the material model for elastic-plastic materials that use the Mises or Hill yield surface (Abaqus documentation). Dependencies parameter is set equal to the number of field variable dependencies included in the definition of hardening behavior, in addition to temperature and possibly strain range. JMatpro was used to derive the plastic material properties. In order to calculate high temperature strength, the hardness of the LTT1 material was set to 349 ±6 according to table 4.1(Timothy Issak Ramjaun 2014).

*Plastic, Dependencies=3

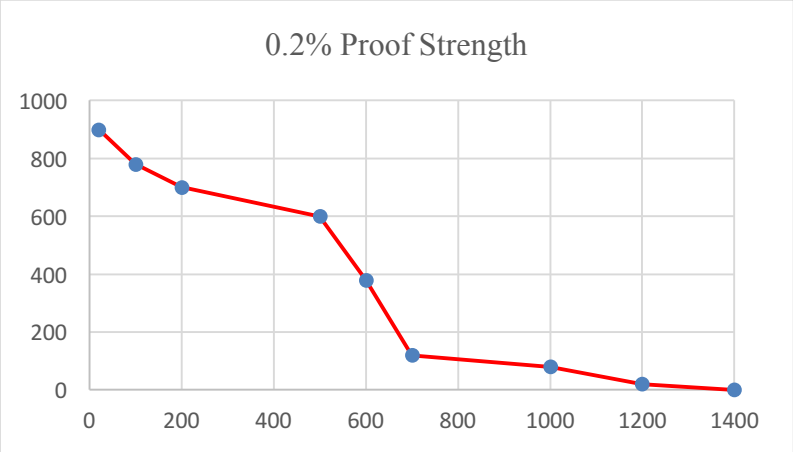


*Figure 7-3 High temperature strength diagram for LTT1 material derived from JMatPro*

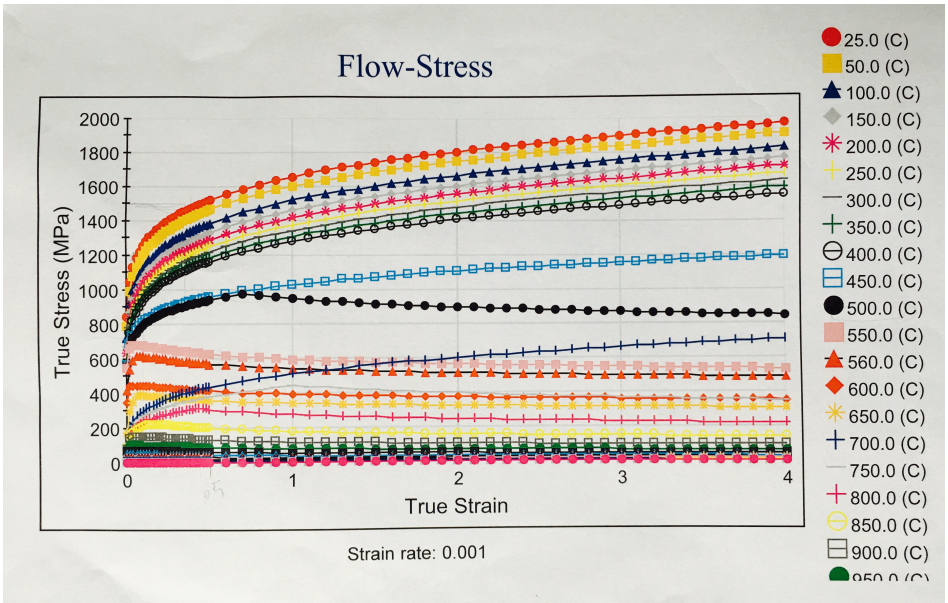


*Figure 7-4 Stress-strain graph for LTT1 derived from JMatPro*

## 7.3 Results

Figure 7-5 and Figure 7-5 show the mechanical results, both the stress component in x direction (perpendicular to the weld) and the displacement. It is obvious that the stress in the melted zone is zero but in the HAZ there is compressive stress because that region is heated and wants to expand while the cold surrounded region prevents its expansion. There are tensile residual stresses in other regions to balance the total stress in the component.

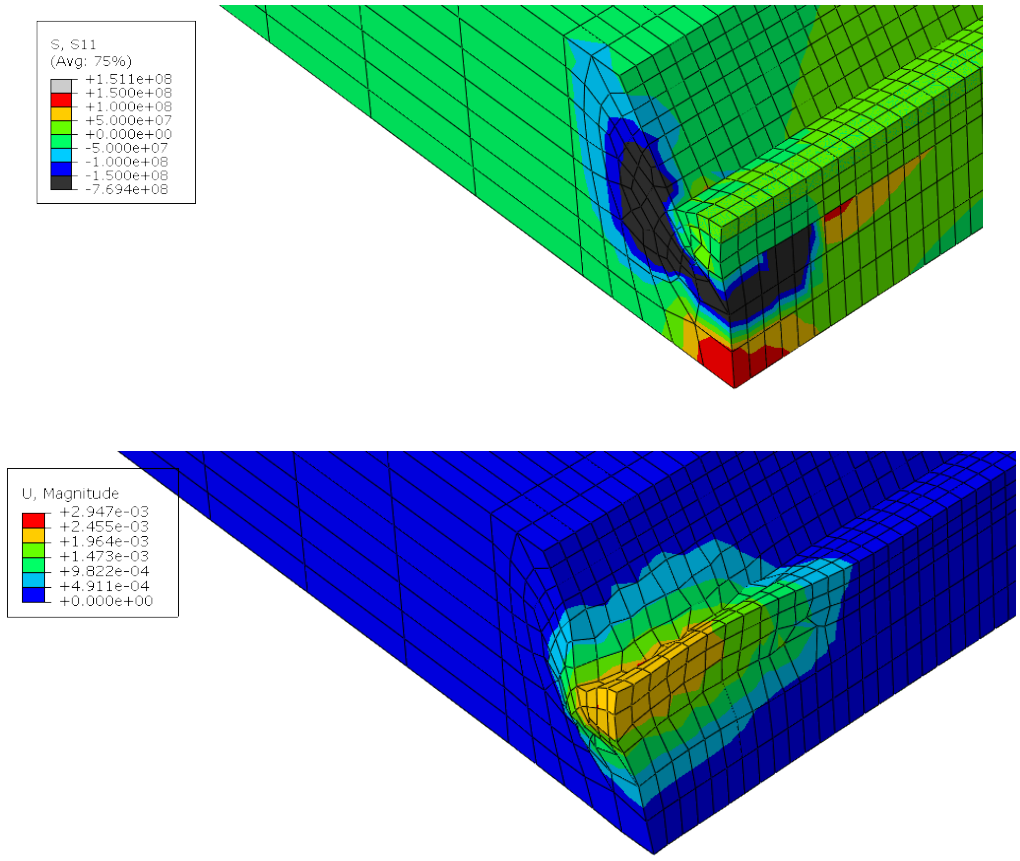


*Figure 7-5 mechanical results a.S11 (stress component) and b. U (displacement)*

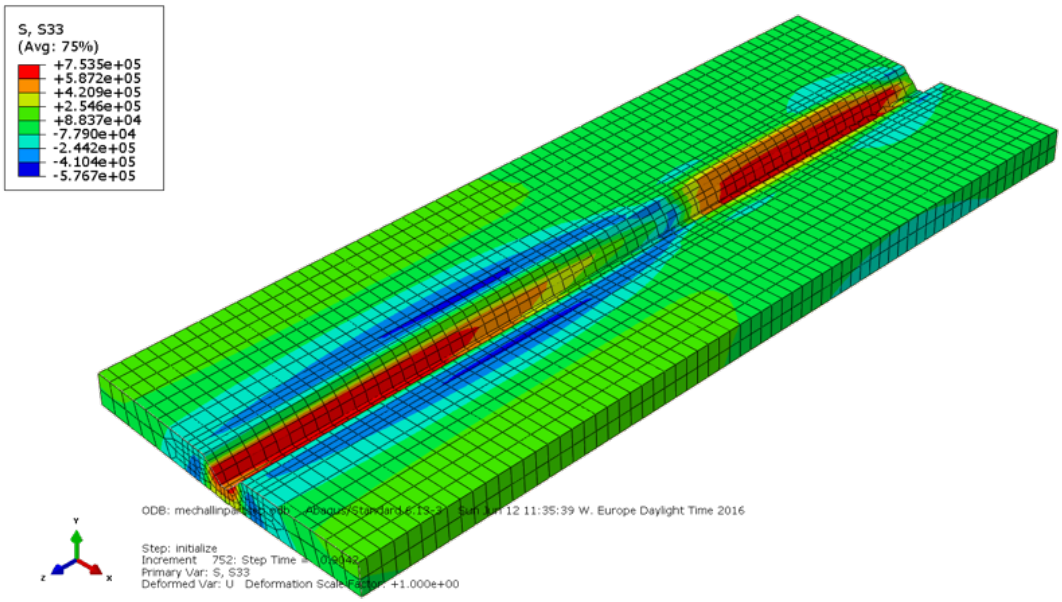


*Figure 7-6 mechanical results S11 (stress component)*

# 8 Conclusion

This research aimed at developing a method for numerical simulation including thermal, metallurgical and mechanical analysis of a welded component.

- As a first step a published round robin analysis was implemented to validate Abaqus as a good simulation tool for thermal welding simulation. This yielded good results.
- As a second step the thermal analysis of the ESAB case was done with two different heat source models, cylindrical and double ellipsoid. The results from the thermal analyses shows good predictions of the temperature history for both FZ and HAZ. Although the Double Ellipsoid heat source provides more accurate results compared to cylindrical heat source, it was decided to go forward with the Cylindrical heat source because it is more cost saving.
- In the third step the metallurgical phase transformation during welding was modeled for both LTT filler material and the base material.
- The final step was mechanical modeling. It was performed by sequentially coupled thermal-stress analysis using the data which were saved during an preceding thermal analysis.

# 9 Recommendation for future studies

The thermal analysis part of the simulation tool with double ellipsoid heat source needs to be further verified and adjusted to find some way to increase the time increments to reduce the computation time.

The metallurgical and mechanical analyses can be further developed.

In this work the data from thermal analysis and phase transformation analysis was saved in a .fil file and used later as the input file for the mechanical analysis. A fully coupled analysis could be done, but were not feasible in this study.

A more sophisticated model for thermal expansion can be done by writing a user/subroutine Uexpan.

# 10 References


"Abkühlzeit t8/5: Erl GmbH SCHWEISSEN+SCHNEIDEN." 2016. Accessed January 26. http://www.erl-gmbh.de/home/fachwissen/berechnungen/abkuehlzeit-t85.html.

Acevedo, C., J. M. Drezet, and A. Nussbaumer. 2013. "Numerical Modelling and Experimental Investigation on Welding Residual Stresses in Large-Scale Tubular K-Joints." *Fatigue & Fracture of Engineering Materials & Structures* 36 (2): 177–85. doi:10.1111/j.1460-2695.2012.01712.x.

Barsoum, Z., and M. Gustafsson. 2009. "Fatigue of High Strength Steel Joints Welded with Low Temperature Transformation Consumables." *Engineering Failure Analysis* 16 (7): 2186–94. doi:10.1016/j.engfailanal.2009.02.013.

Christensen, N, Davies, and K Gjermundsen. 1965. "Distribution of Temperatures in Arc Welding." *British Welding Journal* 12 (2): 54–75.

Deng, Dean. 2009. "FEM Prediction of Welding Residual Stress and Distortion in Carbon Steel Considering Phase Transformation Effects." *Materials & Design* 30 (2): 359–66. doi:10.1016/j.matdes.2008.04.052.

Deng, Dean, and Hidekazu Murakawa. 2013. "Influence of Transformation Induced Plasticity on Simulated Results of Welding Residual Stress in Low Temperature Transformation Steel." *Computational Materials Science* 78 (October): 55–62. doi:10.1016/j.commatsci.2013.05.023.

Dong, P., and J. K. Hong. 2002. "Analysis of IIW X/XV RSDP Phase I Round-Robin Residual Stress Results." *Welding in the World* 46 (5-6): 24–31.

Eagar, T. W., and N. S. Tsai. 1983. "Temperature Fields Produced by Traveling Distributed Heat Sources." *Welding Journal* 62 (12): 346–55.

Easterling, K. E. 1992. *Introduction to the Physical Metallurgy of Welding*. 2nd ed. Butterworth-Heinemann.

El-Ahmar, Walid. 2007. "Robustesse de la simulation numérique du soudage TIG de structures 3D en acier 316L (Robustness of numerical simulation of TIG welding of 3D structures in steel 316L)." INSA-Lyon. http://theses.insa-lyon.fr/publication/2007ISAL0023/these.pdf.

"Erklärungen Zur Abkühlzeit t8/5." 2016. Accessed January 26. http://www.erl-gmbh.de/home/fachwissen/berechnungen/abkuehlzeit-t85/erklaerungen.html.

Fachinotti, Víctor D., Andrés Amílcar Anca, and Alberto Cardona. 2011. "Analytical Solutions of the Thermal Field Induced by Moving Double-Ellipsoidal and Double-Elliptical Heat Sources in a Semi-Infinite Body." *International Journal for Numerical Methods in Biomedical Engineering* 27 (4): 595–607. doi:10.1002/cnm.1324.

Ficquet, X., D.J. Smith, C.E. Truman, E.J. Kingston, and R.J. Dennis. 2009. "Measurement and Prediction of Residual Stress in a Bead-on-Plate Weld Benchmark Specimen." *International Journal of Pressure Vessels and Piping* 86 (1): 20–30. doi:10.1016/j.ijpvp.2008.11.008.

Fischer, F. D., G. Reisner, E. Werner, K. Tanaka, G. Cailletaud, and T. Antretter. 2000. "A New View on Transformation Induced Plasticity (TRIP)." *International Journal of Plasticity* 16 (7–8): 723–48. doi:10.1016/S0749-6419(99)00078-9.

Francis, J. A., H. K. D. H. Bhadeshia, and P. J. Withers. 2007. "Welding Residual Stresses in Ferritic Power Plant Steels." *Materials Science and Technology* 23 (9): 1009–20. doi:10.1179/174328407X213116.

G. B. Marquis, and H. C. Yıldırım. 2015. "Fatigue Improvement of Welded Steel Joints by High Frequency Mechanical Impact Treatment." *WILEY-VCH Verlag GmbH & Co.*

Goldak, J. A, and M. Akhlaghi. 2005. *Computational Welding Mechanics*. Springer Verlag.

Goldak, J., A. Chakravarti, and M. Bibby. 1984. “A New Finite Element Model for Welding Heat Sources.” *Metallurgical Transactions B* 15 (2): 299–305.
Goldak, John A. 2005. *Computational Welding Mechanics*. New York: Springer.
“Goldak.pdf.” n.d.
Grong, O. 1997. *Metallurgical Modelling of Welding*. Materials Modelling Series.
Grong, Øystein. 1997. *Metallurgical Modelling of Welding (2nd Edition)*. Materials Modelling Series. Maney Publishing. http://www.knovel.com/web/portal/browse/display?_EXT_KNOVEL_DISPLAY_bookid=1281.
Günther, Hans-Peter. 2005. *Use and Application of High-Performance Steels for Steel Structures*. IABSE.
Heinze, C., A. Pittner, M. Rethmeier, and S. S. Babu. 2013. “Dependency of Martensite Start Temperature on Prior Austenite Grain Size and Its Influence on Welding-Induced Residual Stresses.” *Computational Materials Science* 69 (March): 251–60. doi:10.1016/j.commatsci.2012.11.058.
Houlsby, G. T., and A. M. Puzrin. 2006. *Principles of Hyperplasticity: An Approach to Plasticity Theory Based on Thermodynamic Principles*. London: Springer.
Kirk, D. 1971. “Experimental Features of Residual Stress Measurement by X-Ray Diffractometry.” *Strain* 7 (1): 7–14.
Koistinen, D.P., and R.E. Marburger. 1959. “A General Equation Prescribing the Extent of the Austenite-Martensite Transformation in Pure Iron-Carbon Alloys and Plain Carbon Steels.” *Acta Metallurgica* 7 (1): 59–60. doi:10.1016/0001-6160(59)90170-1.
Krummenacker, Janna. 2011. “Simulation of the Welding Process of Steel Tube Joints Made of S355 and S690.” Karlsruher Institut für Technologie/École Polytechnique Fédérale de Lausanne. http://infoscience.epfl.ch/record/188683.
Leblond, J.-B., G. Mottet, J. Devaux, and J.-C. Devaux. 1985. “Mathematical Models of Anisothermal Phase Transformations in Steels, and Predicted Plastic Behaviour.” *Materials Science and Technology* 1 (10): 815–22. doi:10.1179/026708385790124017.
Lindgren, L.-E. 2001. “Finite Element Modeling and Simulation of Welding Part 1: Increased Complexity.” *Journal of Thermal Stresses* 24 (2): 141–92.
Lindgren, L. E. 2007. *Computational Welding Mechanics: Thermomechanical and Microstructural Simulations*. CRC Press.
Macherauch, E. 1984. “Residual Stresses.” In *Application of Fracture Mechanics to Materials and Structures*, 157–92. Springer. http://link.springer.com/chapter/10.1007/978-94-009-6146-3_7.
Macherauch, Eckard. 2014. “Introduction to Residual Stress.” *Advances in Surface Treatments*, 1.
M. Hashemzadeh. 2014. *Comparison between Different Heat Sources Types in Thin-Plate Welding Simulation*. International Maritime Association of the Mediterranean. http://dx.doi.org/10.1201/b15813.
Ohta, A., K. Matsuoka, N. T. Nguyen, Y. Maeda, and N. Suzuki. 2003. “Fatigue Strength Improvement of Lap Joints of Thin Steel Plate Using Low-Transformation-Temperature Welding Wire.” *AWS Welding Journal* 82 (4): 78 – S.
Özdemir, Okan, Gürel Çam, Hüseyin Çimenoğlu, and Mustafa Koçak. 2010. “Characterization of Microstructure and Mechanical Properties of Low Temperature Transformation Welds (ltt).” In , 299–304. Turkey.
Prevéy, Paul S 1986. *X-RAY DIFFRACTION RESIDUAL STRESS TECHNIQUES*. Vol. 10. Metals Handbook.

Pavelic, V., R. Tanbakuchi, O. A. Uyehara, and P. S. Myers. 1969. “Experimental and Computed Temperature Histories in Gas Tungsten-Arc Welding of Thin Plates.” *WELD J* 48 (7): 295–305.

Prevéy, Paul S. 2001. “X-Ray Diffraction Characterization of Residual Stresses Produced by Shot Peening.” *Shot Peener(USA)* 15 (1): 4–8.

Radaj, Dieter. 2003. *Welding Residual Stresses and Distortion: Calculation and Measurement*. DVS-Verlag.

Ramjaun, T. I., H. J. Stone, L. Karlsson, M. A. Gharghouri, K. Dalaei, R. J. Moat, and H. K. D. H. Bhadeshia. 2014. “Surface Residual Stresses in Multipass Welds Produced Using Low Transformation Temperature Filler Alloys.” *Science and Technology of Welding and Joining* 19 (7): 623–30. doi:10.1179/1362171814Y.0000000234.

Ramjaun, T. I., H. J. Stone, L. Karlsson, J. Kelleher, S. W. Ooi, K. Dalaei, J. Rebelo Kornmeier, and H. K. D. H. Bhadeshia. 2014. “Effects of Dilution and Baseplate Strength on Stress Distributions in Multipass Welds Deposited Using Low Transformation Temperature Filler Alloys.” *Science and Technology of Welding and Joining* 19 (6): 461–67. doi:10.1179/1362171814Y.0000000209.

Rosenthal, Daniel. 1946. “The Theory of Moving Sources of Heat and Its Application to Metal Treatments.” In *Transactions of ASME*, 68:849.

Rykalin, N. N. 1974. “Energy Sources Used for Welding.” *Soudage et Techniques Connexes L (12)*, 471–85.

Shiga, Chiaki, Eiichi Murakawa, Yuki Matsuo, Uusuke Ohsuga, Kazuo Hiraoka, Yasushi Morikage, and Koichi Yasuda. 2014. “Fatigue Improvement in High-Strength Steel Welded Joints with Compressive Residual Stress.” *Welding in the World* 58 (1): 55–64. doi:10.1007/s40194-013-0093-8.

Simulia. 2013. *ABAQUS 6.13: User’s Manual*. Providence, RI: Dassault Systems.

Smith, M.C., and A.C. Smith. 2009. “NeT Bead-on-Plate Round Robin: Comparison of Transient Thermal Predictions and Measurements.” *International Journal of Pressure Vessels and Piping* 86 (1): 96–109. doi:10.1016/j.ijpvp.2008.11.016.

Taleb, Lakhdar, Nathalie Cavallo, and François Waeckel. 2001. “Experimental Analysis of Transformation Plasticity.” *International Journal of Plasticity* 17 (1): 1–20. doi:10.1016/S0749-6419(99)00090-X.

Timothy Issak Ramjaun. 2014. “Viable Welding Alloy for Mitigation of Residual Stress and Enhancement of Fatigue Resistance.” Doctor of Philosophy, Cambridge.

Totten, George E., Maurice AH Howes, and Tatsuo Inoue. 2002. *Handbook of Residual Stress and Deformation of Steel*. ASM international. http://books.google.ch/books?hl=en&lr=&id=_a9UEHk4cOwC&oi=fnd&pg=PR6&dq=Handbook+Of+Residual+Stress+and+Steel+Deformation+Totten,Howes,Inoue+2002%5D&ots=mgaflvop2u&sig=ekEg4RhDAEIZLMUzLD4mzbCK9zk.

Truman, C.E., and M.C. Smith. 2009. “The NeT Residual Stress Measurement and Modelling Round Robin on a Single Weld Bead-on-Plate Specimen.” *International Journal of Pressure Vessels and Piping* 86 (1): 1–2. doi:10.1016/j.ijpvp.2008.11.018.

Ulrich Dilthey. 2006. *Schweißtechnische Fertigungsverfahren 2*.

Welding Handbook Committee. n.d. “Welding Handbook.” American Welding Society.

Withers, P. J., and P.J. Bouchard. 2006. “Identification of Residual Stress Length Scales in Welds for Fracture Assessment.” In , edited by A. G Youtsos, 163–76. Greece: Springer.

Wohlfahrt, Helmut, Thomas Nitschkepagel, Klaus Dilger, Dieter Siegele, Mr Marcus Brand, Mr Jens Sakkiettibutra, and Tobias Loose. 2012. “Residual Stress Calculations And Measurements—Review And Assessment Of The Iiw Round Robin Results.” *Welding in the World* 56 (9-10): 120–40.

Yildirim, Halid Can. 2013. *Design Aspects of High Strength Steel Welded Structures Improved by High Frequency Mechanical Impact (HFMI) Treatment*. Doctoral Dissertations / Aalto University, School of Engineering, Department of Applied Mechanics 2013,134. Helsinki: Unigrafia Oy.

Zamiri, Farshid. 2014. "Welding Simulation and Fatigue Assessment of Tubular K-Joints in High Strength Steel." Lausanne, Switzerland: École Polytechnique Fédérale de Lausanne. http://infoscience.epfl.ch/record/198448.

# 11 Appendices

## 11.1 Appendix 1 – Dflux for the first model

```
      REAL Qtot, rcyl, hcyl, tweld, Lweld, Vweld, Vol
      REAL Tstart, Tend, Power
      REAL wx, wy, wz, pointx, pointy, pointz, ztop, zbottom, r, t, pi
      INTEGER n
      DIMENSION Flux(2)
      DIMENSION TIME(2)
      DIMENSION Coords(3)
      DIMENSION wstart(3)
      DIMENSION wend(3)

      pi = 4*atan(1.0)

C     _____________________________________
C     Heat source parameters
C     Total welding heat input [micro joules]
      Qtot = 38e+9*0.75

C     radius of torch:
      rcyl = 2.4

C     torch depth:
      hcyl = 0.7

C     number of weld pass
      n = 1

      tweld = 26.4
      Lweld = 60

C     Mean welding power input (micro watt )
      Power =  Qtot/ tWeld
C     welding speed 60mm/26.4
      Vweld = Lweld/tweld
C     _____________________________________

C     start point
      wstart(1) = 0.0
      wstart(2) = 0.0
      wstart(3) = -30.0

C     end point
      wend(1) = 0.0
      wend(2) = 0.0
      wend(3) = 30.0

C     volume of welding cylinder
      Vol = (pi*rcyl**2)*hcyl

C     current time
      t = TIME(2)

C     weld start and end times
      Tstart = 0
      Tend = Tstart + tweld

C     torch location
      wx = wstart(1)
      wy = wstart(2)
      wz = wstart(3) + Vweld*t

C     Coordinates of the point under consideration
      pointx = COORDS(1)
      pointy = COORDS(2)
      pointz = COORDS(3)

C     try 1
      ytop = wstart(2) + hcyl
      ybottom = wstart(2)
      DO i = 1,n
         IF (t.GE.Tstart.AND.t.LE.Tend) then
            IF(pointy.GE.ybottom.AND.pointy.LE.ytop) then
               r = (((pointx - wx)**2 + (pointz - wz)**2)**0.5)
               IF (r.LE.rcyl) then
                  Flux(1) = Power/Vol
                  WRITE (6,*) t, Flux(1), r, Vol
                  EXIT
               END IF
            END IF
            Flux(1)=0
         ELSE
            Flux(1)=0
         END IF
      END DO
      Flux(2)=0.
```

## 11.2 Appendix 2- Round Robin model's Properties

Table 11-1 thermal properties used in the round robin model

| T | Conductivity | specific heat(parent) | specific heat(weld) |
|---|---|---|---|
| 0 | 14.12E3 | 0.492E9 | 0.488E9 |
| 10 | 15.26E3 | 0.502E9 | 0.502E9 |
| 200 | 16.69E3 | 0.514E9 | 0.520E9 |
| 300 | 18.11E3 | 0.526E9 | 0.537E9 |
| 400 | 19.54E3 | 0.538E9 | 0.555E9 |
| 500 | 20.96E3 | 0.55E9 | 0.572E9 |
| 600 | 22.38E3 | 0.562E9 | 0.589E9 |
| 700 | 23.81E3 | 0.575E9 | 0.589E9 |
| 800 | 25.23E3 | 0.587E9 | 0.589E9 |
| 900 | 26.66E3 | 0.599E9 | 0.589E9 |
| 1000 | 28.08E3 | 0.611E9 | 0.589E9 |
| 1100 | 29.5E3 | 0.623E9 | 0.589E9 |
| 1200 | 30.93E3 | 0.635E9 | 0.589E9 |
| 1300 | 32.35E3 | 0.647E9 | 0.589E9 |
| 1400 | 33.78E3 | 0.659E9 | 0.589E9 |
| 1500 | 135.12E3 | | |

## 11.3 Appendix 3 - ESAB model's geometry

b

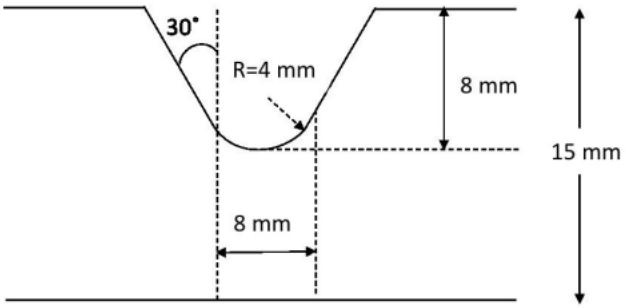


c

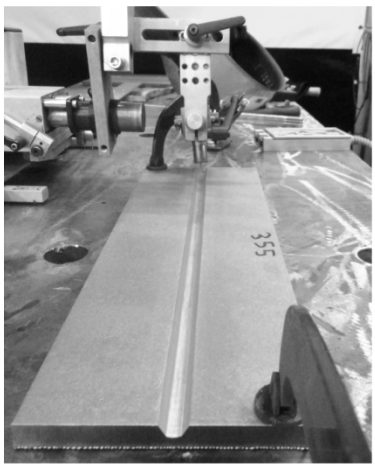

(a, b) cross-section of the machined V-groove ( 500*150*15 mm Plate)

(c) Ready set up for welding

## 11.4 Appendix 4 - Material composition

Weld and base composition

| Alloy | C | Si | Mn | Cr | Ni | Mo |
|---|---|---|---|---|---|---|
| LTT1 | 0.028 | 0.78 | 1.63 | 12.68 | 6.01 | 0.066 |
| BP700 | 0.15 | 0.29 | 0.98 | 0.25 | 0.043 | 0.15 |